



UNIVERSITÀ  
DEGLI STUDI  
DI PADOVA

UNIVERSITÀ DEGLI STUDI DI PADOVA

**Dipartimento di Ingegneria Industriale DII**

Corso di Laurea Magistrale in Energy Engineering

***Influence of the micro and macro structure of stainless-steel  
surfaces on boiling heat transfer***

Relatore: Prof. Ing. Davide Del Col (DII- Università degli Studi di Padova)

Correlatori: Prof. Ing. Luke Andrea (TTK-Universität Kassel)

Ing. Mohammad Deeb (TTK-Universität Kassel)

Studente: Anna Borini (2052443)

Anno Accademico

2022/2023



## ABSTARCT

Over the past 80 years the heat transfer under boiling conditions has been investigated extensively by many scientists worldwide. This interest is justified in part by the heat transfer enhancement that this mechanism promotes on heated surfaces, and consequently by its potential in heat transfer applications. The present investigation is restricted to fully developed nucleate boiling and to small heat fluxes at the beginning of nucleation; high superheats connected with film boiling will be excluded. Therefore, the aim in the design of an evaporator should be to reduce the temperature gradient, to significantly improve the heat transfer and to avoid possible metastable hysteresis effects. New prediction methods for the heat and mass transfer in boiling will be required in future to replace the empirical correlations used until now, since they are inexact for many applications. The motivation of this work lies in the analysis of the influence of heating surface roughness and material on nucleation in saturated liquids (n-pentane, 1-hexanol and 1-pentanol). The experimental data of the pure substances should contribute to an improved and more precise dimensioning of heat exchangers as these are currently often oversized and lead to unnecessarily high material and cost expenditure. All measurements considered in this work are performed in a standard boiling apparatus carried out in the area of convective boiling and nucleated boiling. The heat transfer coefficient is recorded in a range of the heat flux from  $50 \text{ W/m}^2$  to  $100 \text{ kW/m}^2$  for the respective reduced pressures and three different tubes (two plain stainless-steel and copper and one finned stainless steel) are used to perform this analysis. Subsequently, the measured values are compared with correlations according to Gorenflo (VDI-2010) [1] and Slipcevic [2] as well with other measurements from the literature in double logarithmic representations. Parallel to carrying out the heat transfer coefficient measurements, visual recordings are made in the form of high-resolution images of the boiling conditions. At the end of the work, some conclusions are reported with the aim of predicting of how much the choice of a particular material, roughness and substance inside the evaporator can affect it.



## TABLE OF CONTENTS:

NOMENCLATURE.....	7
1. INTRODUCTION.....	11
2. THEORETICAL BASIS.....	13
2.1 Mechanisms of heat transfer during boiling.....	13
2.2 Single phase free convection.....	19
2.3 Basics of vapor bubble formation.....	21
2.4 Calculation methods for nucleate boiling for smooth tubes.....	30
2.4.1 Effect of heat flux and pressure.....	32
2.4.2 Effect of the properties of the fluid.....	34
2.4.3 Effect of the properties of the heater.....	34
2.5 Calculation method for finned tubes.....	37
2.5.1 Calculation according to Gorenflo.....	37
2.5.2 Calculation according to Slipcevic.....	38
3. SURFACE ANALYSIS.....	41
3.1 Surface treatment.....	42
3.1.1 Operating principle of the sandblasting system.....	42
3.2 Surface analysis using optical measurement technology.....	45
3.2.1 Measuring principle of the optical measuring device.....	46
3.4 Results of the roughness analysis of the treated tubes.....	49
3.4.1 Roughness results of the stainless-steel plain tube.....	49
3.4.2 Shape and roughness results of the stainless-steel finned tube.....	53
4. THE EXPERIMENTAL PLANT AND TEST SUBSTANCES.....	61
4.1 Test facilities.....	62
4.1.1 Climate cell.....	62
4.1.2 Evaporator.....	62
4.1.3 Condenser.....	63
4.1.4 Test tubes.....	63
4.1.5 Pipe wall correction.....	67
4.2 Thermostats.....	69
4.3 Measuring device.....	69
4.3.1 Temperature measurement technology.....	69

4.3.2	Resistance thermometer .....	70
4.3.3	Thermocouples .....	70
4.3.4	Pressure measurement technology .....	71
4.3.5	Safety device .....	71
4.3.6	Measuring program .....	72
4.4	Preparation and performance of the measurements.....	72
4.4.1	Starting the measurement .....	72
4.4.2	Recording of the measuring points.....	74
5.	TEST EVALUATION .....	77
5.1	Measurement results on smooth stainless-steel and copper tubes.....	77
5.2	Measurement results for the stainless-steel finned tube .....	90
5.3	Comparison on the tube wall superheating for the different substances .....	99
5.4	Comparison with other correlations .....	107
5.5	Comparison of measurement results for hydrocarbons.....	110
5.6	Effect of the material on the thermal heating wall properties .....	113
6.	SUMMARY AND OUTLOOK .....	117
7.	REFERENCES.....	121
8.	APPENDIX .....	123

## NOMENCLATURE

### Latin letters:

A	Heat transfer area	[m <sup>2</sup> ]
a	Thermal diffusivity	[m <sup>2</sup> /s]
b	Fin width	[m]
b <sub>t</sub>	Fin pitch at the base	[m]
C <sub>p</sub>	Specific heat capacity	[J/kg·K]
d	Pipe diameter	[m]
d <sub>B</sub>	Bladder tear-off diameter	[m]
e	Thermal effusivity	[W·√s/(m <sup>2</sup> ·K)]
F <sub>q</sub>	Influence of the heat flow density	[-]
F <sub>p</sub> *	Influence of the boiling temperature	[-]
F <sub>W</sub>	Influence of the heating wall properties	[-]
F <sub>WR</sub>	Influence of the heating wall roughness	[-]
F <sub>WM</sub>	Influence of the heating wall material	[-]
g	Gravitational constant	[m/s <sup>2</sup> ]
h	Fin height	[m]
h <sub>R</sub>	Reduced height	[m]
K	Pipe factor	[K]
I	Current	[A]
l	Pipe length	[m]
n	Slope	[-]
P	Electrical power	[W]
P <sub>a</sub>	Arithmetic average roughness height	[μm]
P <sub>f</sub>	Fluid parameter	[(μmK) <sup>-1</sup> ]
P <sub>q</sub>	Quadratic average roughness height	[μm]
P <sub>p</sub>	Smoothing depth	[μm]

$P_{pm}$	Average smoothing depth	[ $\mu\text{m}$ ]
$P_v$	Depth of the largest profile valley	[ $\mu\text{m}$ ]
$P_t$	Total roughness height	[ $\mu\text{m}$ ]
$P_z$	Mean peak to valley height	[ $\mu\text{m}$ ]
$p$	Pressure	[bar]
$p_{cr}$	Critical pressure	[bar]
$p_s$	Saturation pressure	[bar]
$p_0$	Vapor pressure at a flat phase interface	[bar]
$\dot{q}$	Heat flux density	[ $\text{W}/\text{m}^2$ ]
$\dot{Q}$	Heat flow	[W]
$R_a$	Arithmetic mean roughness	[ $\Omega$ ]
$R_0$	Cable resistance	[ $\Omega$ ]
$R_{p,old}$	Smoothing depth acc. to DIN 4762 (1960)	[ $\Omega$ ]
$R_l$	Line resistance	[ $\Omega$ ]
$R$	Ohmic resistance	[ $\Omega$ ]
$r$	Radius	[m]
$r_b$	Radius of the base of the finned tube	[m]
$T$	Temperature	[K]
$T_c$	Critical temperature	[K]
$T_F$	Fluid temperature	[K]
$T_G$	Gas temperature	[K]
$T_L$	Liquid temperature	[K]
$T_{sat}$	Saturation temperature	[K]
$T_w$	Wall temperature	[K]
$t$	Fin pitch	[m]
$t_l$	Clear fin spacing	[m]
$U$	Voltage	[V]
$w$	Distance between base and fin tip	[m]
$X$	Temperature change over the fin height	[K]



**Greek letters:**

$\alpha$	Heat transfer coefficient	[W/m <sup>2</sup> ·K]
$\beta$	Isobaric coefficient of thermal expansion	[°C]
$\beta_0$	Contact angle	[°]
$\eta_f$	Fin efficiency	[-]
$\Delta$	Difference	[-]
$\Delta G_{\max}$	Activation energy	[kJ/mol]
$\Delta h_v$	Enthalpy of vaporization	[J/kg]
$\Delta \rho$	Density difference	[kg/m <sup>3</sup> ]
$\Delta p$	Pressure difference	[bar]
$\Delta T$	Wall superheat	[K/°C]
$\Delta T_{\text{corr}}$	Correction factor	[K]
$\lambda$	Thermal conductivity	[W/(m·K)]
$\mu$	Dynamic viscosity	[Pa·s]
$\nu$	Kinematic viscosity	[m <sup>2</sup> /s]
$\pi$	Pygreco	[-]
$\rho_G$	Gas density	[kg/m <sup>3</sup> ]
$\rho_L$	Liquid density	[kg/m <sup>3</sup> ]
$\sigma$	Surface tension	[N/m]
$\varphi$	Area increase	[-]

**Indices:**

0	Related to a normal state
b	Related to the base
c	Core
corr	Correction factor
crit	Related to the critical state
Cu	Copper
f	Finned

G	Related to the vapor or the gaseous phase
i	Inner
L	Referred to the liquid or the liquid phase
lam	Laminar
turb	Turbulent
meas	Measure reading
nb	Nucleate boiling
o	Outer
real	Real (experimental) measured values
ref	Reference
sat	Saturation
p	Calculated values for a smooth pipe surface
w	Wall
T	Total
tube	Related to the pipe

**Dimensionless metrics:**

$A^*$	Borinshanski-Mostinski parameter
$A_3$	Noyes constant
Gr	Grashof number
$K_B$	Slipcevic constant
$K_1$	Kutateladze constant
Nu	Nusselt number
Pr	Prandtl number
$S_B$	Heat loss in the fins

## 1. INTRODUCTION

The combination of a worldwide increasing demand of energy, the progressively scarcer emerging fossil fuels and the need to reduce risks of climate change is reflected in a rethinking of energy production. Renewable energies such as wind and solar energy can make a significant contribution to climate protection, but the main success factor lies in the efficiency of the equipment used. For this reason, the productivity of existing technologies for energy conversion must be improved and replaced by new methods. Nucleate pool boiling is an effective mode of heat transfer since high heat transfer coefficients for small driving temperature differences can be reached, indeed evaporator processes are widely used in the energy and process technology, as in power stations, refrigeration and thermal separation processes. Despite the large number of studies on boiling heat transfer, the prediction of heat transfer coefficients is still based on empirical or semi empirical methods. Therefore, the motivation of this work lies in the improvement of the predictive methods for the calculation of the heat transfer coefficient  $\alpha$  in pool boiling, being an important tool for the optimum design of the evaporators and for the successful operation of refrigeration units. In this investigation, it will be used a finned stainless-steel tube and stainless steel and copper smooth tubes under variation of the main factors influencing nucleate boiling. As test materials the hydrocarbon n-pentane, as well as the alcohols 1-pentanol and 1-hexanol will be analyzed. An optical device is used to measure roughness for smooth tubes and geometry for threaded tubes. The prediction method given in the VDI-Heat-Atlas [1] will be taken as an example for the currently available methods in the literature and to conclude the analysis a comparison between the experimental values and the ones available in the literature is carried out.



## 2. THEORETICAL BASIS

Heat transfer in pool boiling is mainly used in flooded evaporators in refrigeration, air conditioning, heat pumps and petrol industry. The main advantage of the nucleate boiling mechanisms is that large heat transfer rates may be achieved with small temperature gradients. The difficulty of achieving a unified predicted method lies in the large number of parameters that influence this phenomenon and their complexity in interacting with each other. Therefore, empirical correlations based on more or less accurate measurement data are still applied for the design of modern evaporators.

### 2.1 Mechanisms of heat transfer during boiling

By vaporization we mean the process of converting a liquid into vapor because of heat supply. It can take place into two ways:

- Boiling: when bubbles of vapor are formed on a heated surface immersed in the liquid or, more rarely, in the liquid itself; the temperature of the heated surface will be higher than the saturation temperature of the liquid.
- Evaporation: when the liquid vaporized at a liquid-vapor interface, without the formation of bubbles.

Pool boiling refers to boiling processes without an imposed forced flow, where fluid flow is caused by natural convective phenomena only. The supply of heat can be electric, nuclear (increase in the heat flux density) or implemented using a fluid (temperature increase). In the case examined here, the heating element is electrically heated with a defined power and the temperature difference between the surface and the surrounding boiling liquid is measured. There is a defined correlation between the heat flux, given by the ratio between the supplied heat flow  $\dot{Q}$  and the heat transfer surface:

$$\dot{q} = \frac{\dot{Q}}{A} \quad (2.1)$$

and the temperature difference:

$$\Delta T = T_w - T_{sat} \quad (2.2)$$

where  $T_w$  is the wall temperature and  $T_{sat}$  is the saturation temperature of the boiling liquid. This relation is described with the so-called Nukiyama curve in Fig. 2.1, where it is described the stationary boiling curve of a fluid in the saturation state with a fixed heating surface for natural convection. The evolution of this curve depends on a large number of influencing factors [3]:

- Thermophysical properties of the fluid and possible additives in real vaporizers (oils, surfactants and particles).
- Operating parameters such as saturation pressure or saturation temperature and heat flux.
- Heating surface properties: geometry of micro- and macrostructure, material properties, wettability by the respective fluid, surface energy and the associated tendency to fouling.
- Design of the evaporator and orientation of the heating surface to the direction of gravity.
- Additional convection effects.

In 1934 Nukiyama did the following experiment: in a vessel full of water, at atmospheric pressure and in saturation conditions, he immersed a platinum wire that was electrically heated. The thermal flux released by the wire could be calculated if the voltage drop at its ends and the current intensity were known. The wire wall temperature was derived from electrical resistance measurements. Nukiyama varied the specific heat flow given by the Joule effect and he measured the resulting wall temperature  $T_w$  of the heating body, plotting the trend as reported in the figure below. Four different boiling regimes or mechanisms are distinguished regarding the heat transfer mechanisms, as shown in Fig. 2.1: convective boiling (until “A”), nucleate boiling (“A” to “B”), transition boiling (“B” to “C”) and film boiling (“C” to “D”).

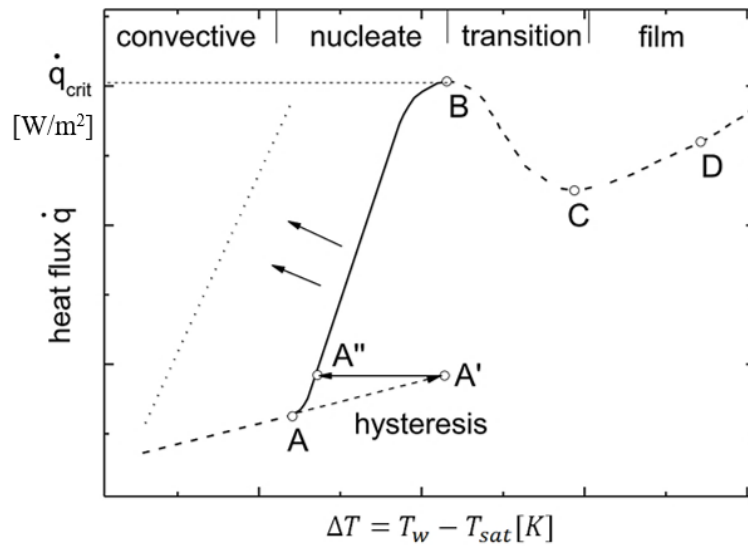


Figure 2.1: Schematic representation of the boiling curve with the four different boiling mechanisms indicated [3].

As soon as the first bubble appears, the wall superheat decreases, due to the improved heat transfer. The range of nucleate boiling from point A to the critical heat flux (point B) is used in many engineering applications because at low wall overheating high heat flows can be transferred. The beginning of nucleate boiling, see point “A” in Fig. 2.1, is characterized by the formation of the “first” bubble on the heating surface. The initial of nucleate boiling is featured by a large range of hysteresis which may lead to permanent damage to the heating surface, if the superheat becomes too high. The phenomenon called hysteresis can be divided into several subsets: TOS (hysteresis of temperature overshoot) is a hysteresis phenomenon involving the delayed of the onset of nucleate boiling, while TD (temperature deviation) is defined as the hysteresis that occurs in the transition region between partial and fully developed nucleate boiling as shown in Fig. 2.2.

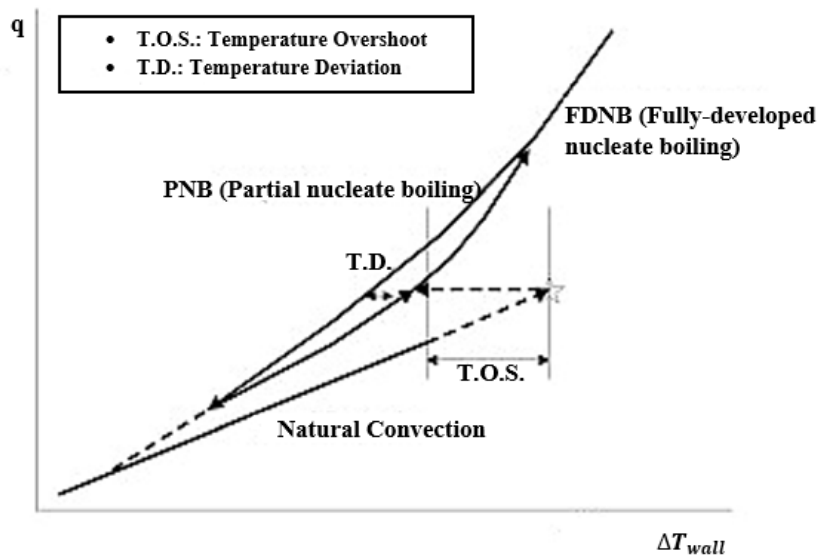


Figure 2.2: Characteristic curves of nucleate pool boiling hysteresis [4].

As it is possible to note from the Fig. 2.3 (on left side) by increasing the heat flux gradually, the boiling region spreads downstream.

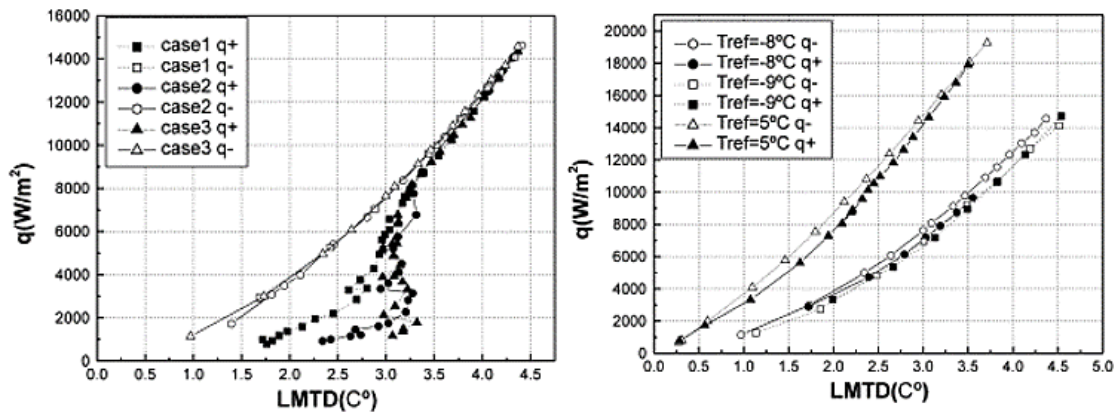


Figure 2.3: Boiling curves for various conditions of incipience (left side) and TD hysteresis for each refrigerant temperature (right side) [4].

As a result, the LMTD (Log Mean Temperature Difference) changes little, although high heat flux is applied. If the heat flux decreases after reaching a high heat flux, no significant change of heat flux is found until the complete spreading of nucleate boiling (CSNB) is reached. However, the decreasing path does not follow the  $q^+$  curve anymore and the heat flux gradually decreases. The incipience of boiling ( $q^+$ ) is delayed due to



the combined TOS, and the boiling area spreads until the boiling occurs all over the area. Only the density of boiling spots decreases in the whole area. In other words, the refrigerant boils but sometimes it doesn't boil in spite of the similar conditions. This can be a fatal problem for normal operation because no boiling means that the performance of a refrigeration system falls abruptly. Fig. 2.3 (on the right side) shows the hysteresis named temperature deviation (TD). The performance of heat transfer is influenced by the history of heat flux. The heat flux for  $q^-$  is always higher than that for  $q^+$ . The difference between the increasing and the decreasing heat flux causes a different heat transfer coefficient. The onset of nucleate boiling (ONB) is defined as the condition when the nucleate boiling is first initiated, and the range of hysteresis has always to be passed through. The range of hysteresis may be reduced or even avoided by shifting the onset of nucleate boiling towards smaller superheats  $\Delta T$  by “early” activation, see the dotted straight line in Fig. 2.1. The superheat required by the liquid can be estimated from the slope of the equilibrium vapor pressure curve  $\left(\frac{dp}{dT}\right)_{sat}$ . An increase in wall superheat activates an increasing number of smaller nucleation sites, leading to the nonlinear increase in  $\dot{q}$ . Nucleate boiling allows heat to be transferred at comparatively high rates by applying small temperature differences. However, there is a limit to the extent that the heat flux can thus be increased. The temperature difference  $\Delta T$  at which this maximum (or critical) heat flux  $\dot{q}_{crit}$  occurs depends on the saturation pressure. In this regime of very intense nucleate boiling, a coherent film of vapor starts to form on parts of the heated surface, leading to a new regime of total film boiling when the surface is completely covered by vapor. There, the heat flux increases again with  $\Delta T$ , at first with slightly decreasing of the heat transfer coefficient and then at a rate corresponding to a gradual increase at very high superheats, mainly because of growing turbulence in the film of vapor and the gradual increase in heat transfer by radiation. The absence of contact between the liquid and the heating surface reduces the influence of the surface properties, compared to nucleate boiling. It is worth noting that the heat transfer coefficient, the maximum heat flux in nucleate boiling and the minimum heat flux in film boiling depend considerably on pressure, whereas the heat transfer in total film boiling and in single-phase free convection is only slightly influenced by the

pressure (and thus by the temperature) in the saturated state. The point “C” of minimum heat flux and minimum wall temperature in total film boiling is called the Leidenfrost point. At this one the balance arises, and the temperature of the heating surface is so high that the addition heat is given off by radiation from the heating surface. This area is called transitional boiling and should be avoided at all costs, since the heating surface temperatures are above the melting temperature of the used material. At least in this area the damage to the heating surface used is to be expected. This transition is important during the cooldown of cryogenic systems, and during the metallurgical quenching of components with a large thermal capacity. For the transfer of a quantity of heat, calculated from the difference between the wall temperature  $T_w$  and saturation temperature of the fluid  $T_{sat}$  we can define the heat transfer coefficient:

$$\alpha = \frac{\dot{q}}{\Delta T} \quad (2.3)$$

The heat transfer in free convection describes the process until reaching the heat saturation temperature  $T_{sat}$ . When exceeding the saturation temperature, there is the formation of vapor bubbles.

## 2.2 Single phase free convection

Single-phase free convection without bubble formation may occur in regions of evaporators where the heating surface operates at small wall superheats or low heat fluxes below the onset of nucleate boiling. There are two predictive equations used generally for free convection, one for laminar flow and the other for turbulent flow in the boundary [1]:

$$Nu_{lam} = 0.60(GrPr)^{\frac{1}{4}} \quad (2.4)$$

$$Nu_{turb} = 0.15(GrPr)^{\frac{1}{3}} \quad (2.5)$$

Valid in both cases for Prandtl numbers lying in the range 2 - 100. The two equations predict the same Nusselt number  $Nu$  when the Rayleigh number ( $Ra$ ), equal to the product of Grashof number  $Gr$  and Prandtl number  $Pr$ , is slightly less than  $2 \times 10^7$ , so the transition from turbulent to laminar flow probably occur in the range  $10^7 < GrPr < 10^8$ . The transition from laminar to turbulent flow may be shifted toward much higher values of  $GrPr$  in special cases in which laminar flow is favored by the geometry and finish of the heating surface. They are only weakly dependent on the heat flow density, and they are mainly influenced by the substance data being proportional to the Grashof and Prandtl numbers. The Grashof number is a dimensionless number which approximates the ratio of the buoyancy to viscous forces acting on a fluid and it is used for describing the heat transfer in natural convection and it is defined as:

$$Gr = \frac{g\beta(T_w - T_F)d^3}{\nu^2} \quad (2.6)$$

where  $g$  is gravitational acceleration due to earth,  $\beta$  represents the isobaric coefficient of thermal expansion, equal to approximately  $1/T$  for ideal gases,  $d$  is the diameter of the tube, which reflects the characteristic length,  $(T_w - T_F)$  is the subtraction between the wall temperature and the fluid temperature and the kinematic viscosity of the fluid is expressed by  $\nu$ .

Whereas the Prandtl number is defined as:

$$\text{Pr} = \frac{\nu}{a} = \frac{\mu/\rho_L}{\frac{\lambda_L}{Cp \cdot \rho_L}} = \frac{\mu \cdot Cp}{\lambda_L} \quad (2.7)$$

This is a physical property ratio between the kinematic viscosity  $\nu$  (that is the ratio between the dynamic viscosity and the density of the fluid) and the thermal diffusivity  $a$  that is the ratio between the thermal conductivity of the fluid and the product between the specific heat capacity and the density of the fluid. The Nusselt number is defined as the ratio between the convective heat and the conductive heat transfer at a boundary in a fluid. So, it is equal to the ratio between the product of the convective heat transfer coefficient  $\alpha$  and the characteristic length that in this case is the pipe diameter  $d$  and the thermal conductivity of the liquid  $\lambda_L$ .

$$\text{Nu} = \frac{\alpha \cdot d}{\lambda_L} \quad (2.8)$$

### 2.3 Basics of vapor bubble formation

Vapor bubbles grow from active nucleation sites once the surface attains the wall superheat required for nucleation. Fig. 2.4 (reported below) shows diagrammatically the pressure-volume isotherms for a pure single-component substance. For a constant temperature  $T$ , the pressure and volume vary along a line such as ABFG. Liquid only exists along the line AB; vapor only exists along the line FG and liquid and vapor coexist along the line BDF. Points in the metastable region may be reached by carefully increasing the liquid temperature above the saturation temperature corresponding to the imposed static pressure; this process is referred to as superheating and the metastable liquid state is referred to as superheated liquid. Vapor and liquid phases can coexist in unstable equilibrium states along lines such as BC or FE.

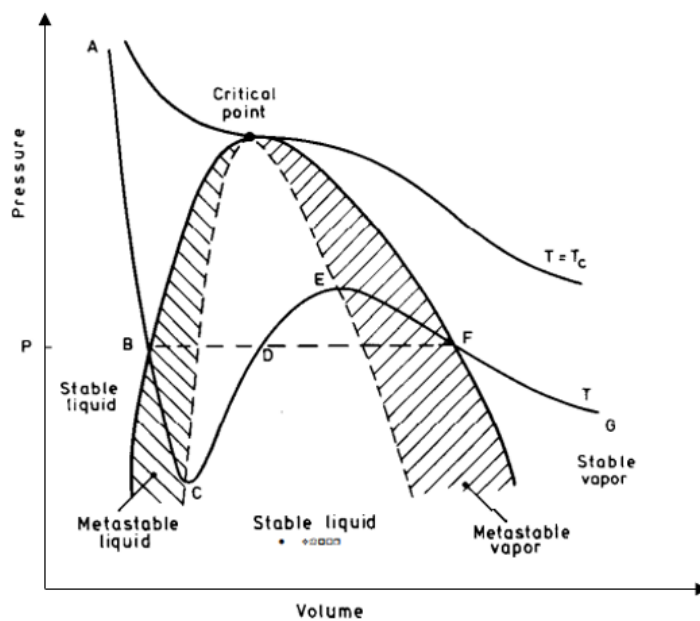


Figure 2.4: Pressure-volume surface for a pure substance [5].

Initially the bubble growth is driven by the excess vapor pressure not balanced by the surface tension forces and the inertia of the surrounding liquid control the process. This stage is very short (a few ms after the inception). In the later stage the bubble growth is governed by the rate of conduction from the superheated liquid to liquid-vapor interface. So, before the formation of the first bubble, it is not present in the liquid a

stable thermodynamic equilibrium but it's a metastable state. Before going to analyze the process in detail, it is necessary to discern the nucleation into homogeneous and heterogeneous nucleation. In the case of homogeneous nucleation there is no contact between the vapor bubbles (within a liquid) and the heating surface, while heterogeneous nucleation, that is considered in this analysis, takes place on solid surfaces. The nucleation sites are characterized by microscopic cavities or indentations and the shape and the size of them depends on the manufacturing process of the heating surface. It is important to distinguish between active and potential nucleation sites. Active nucleation sites show a time-varying frequency of growth and tearing off of the vapor bubbles, while in potential nucleation sites, the bubble rupture is observed only sporadically. With an accurate analysis, it is possible to notice the presence of microscopic cavities where there is the formation of a certain quantity of vapor ("meniscus") inside the cavity with a heating surface. At the surface of the bubbles, a phase interface forms between the liquid, gaseous and the solid phase. The vapor that is formed in the cavity with the superheating is going to increase because, with the increasing in temperature, there is the expansion of the gas. For the complete growth of a vapor bubble there must be an equilibrium between the gaseous bubble and the surrounding liquid.

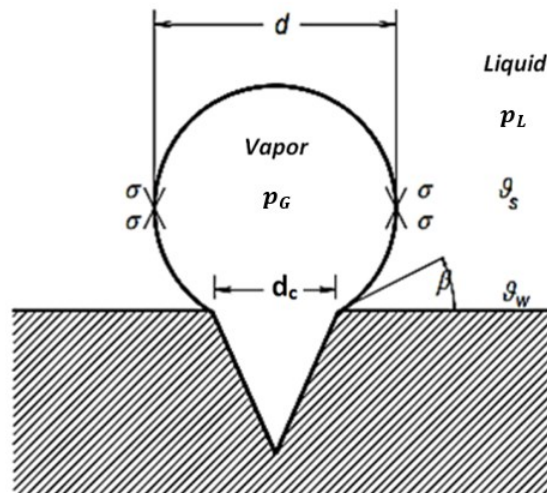


Figure 2.5: Qualitative representation of an incipient bubble in a nucleation site taken from [6].

When buoyancy of the vapor bubble is higher than the dynamic force that depends on the inertial force or surface tension, the bubble tears off from the heating surface. So, when the critical size of a viable bubble is reached, the bubble constricts and tears off, Fig. 2.6 (a-b). This creates two subsets and by the rise of the vapor bubble the liquid is mixed and supercooled liquid flows to the heating surface. This process has a positive effect on the heat transfer. In this way, after a bubble breaks away from the surface, a smaller one remains in the recess, while the larger amount of steam is in the rising bubble, Fig. 2.6 (c). The bigger one tries to go up for the difference of density with the bottom part that has a higher density compared to the bigger part. At the bottom point of the bubble, a pressure drop (metastable state) is induced and so there is a capillary pressure (depression). In this condition, the system tries to find the equilibrium, so for that reason there are vibrations and points in the liquid where we have slightly higher pressure that tends to go in the zone in which we have lower pressure. In this way the heat transfer due to convection is enhanced. Having a continuous heating of the surface, the part of the droplet that remains near the surface, is heated and then the same happens to the liquid, so there is a better transport of heat surface-bubble-liquid. If there is an increase of the  $\Delta T$ , the part of vapor that is remained adhered to the surface, increases its volume and so we have the formation of another bubble. After the formation of the new bubble, the last droplet lifts up and we have an improvement of the heat transfer

due to conduction. In the case in which we have a decrease the  $\Delta T$ , there is in any case the formation of bubble, but it has not the possibility to grow, so immediately after the formation it breaks and then it condenses again.

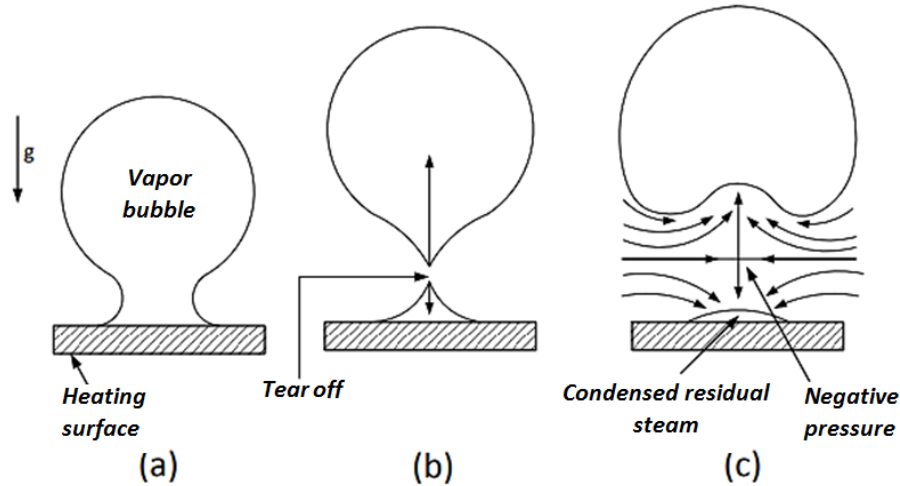


Figure 2.6: Schematic representation of the formation and demolition of a vapor bubble from the heating surface [7].

In fact, because of surface tension  $\sigma$ , the pressure inside a vapor nucleus of radius  $r$  must be higher than the pressure in the adjacent liquid. This phenomenon can be described physically by what is called the Young-Laplace equation that is an algebraic equation that describes the capillary pressure difference sustained across the interface between two static fluids due the phenomenon of surface tension or wall tension. The following considerations are applied to the equilibrium of a bubble assumed to be spherical, with the liquid surrounding it. Between the gaseous bubble (gas=index G) and the surrounding liquid (liquid = index L) thermal equilibrium exists [8]:

$$T_G = T_L = T \quad (2.9)$$

If a surface element of a spherical shell is cut out of a vapor bubble, as depicted in the right side of Fig. 2.7, with side lengths  $rd\varphi$ , the forces  $\sigma rd\varphi$  exerted by the surface tension  $\sigma$ , that is a force per unit of length, act upon the edges.



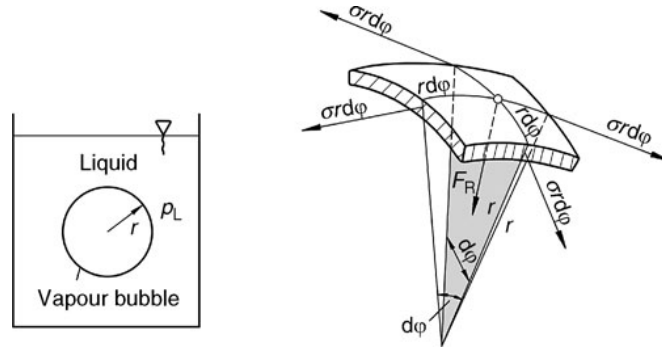


Figure 2.7: Mechanical equilibrium between a spherical vapor bubble and the liquid surrounding it [8].

The resultant  $F_R$  of these forces is given by:

$$d^2 F_R = 2\sigma r d\varphi^2 \quad (2.10)$$

These forces resulting from the gas and liquid pressure are also of influence:

$$p_L (rd\varphi)^2 + d^2 F_R = p_G (rd\varphi)^2 \quad (2.11)$$

From this, the condition of mechanical equilibrium is obtained:

$$p_G = p_L + \frac{2\sigma}{r} \quad (2.12)$$

From the equation above it is possible to observed that the vapor in the bubble must be at higher pressure compared to that of the surrounding liquid because in addition to the liquid pressure the surface tension acts on the phase interface between bubble and liquid as can be shown with a simple force balance. Finally, the condition of equilibrium with respect to the mass exchange between the gaseous and liquid phase also holds. In 1871, William Thomson published an equation describing capillary action, relating to the curvature of a liquid-vapor interface to the vapor:

$$p_L = p_0 - \frac{\rho_L}{\rho_L - \rho_G} \frac{2\sigma}{r} \quad (2.13)$$

$$p_G = p_0 - \frac{\rho_G}{\rho_L - \rho_G} \frac{2\sigma}{r} \quad (2.14)$$

It produces a relationship between the vapor pressure  $p_0(T)$  at a flat phase interface, the liquid pressure  $p_L(T, r)$  and the vapor pressure  $p_G(T, r)$  at the surface of a bubble of radius  $r$ . These relationships are illustrated in Fig. 2.8. At a given temperature  $T$ , the vapor pressure  $p_G$  is smaller by:

$$p_0 - p_G = \Delta p_G = \frac{\rho_G 2\sigma}{\Delta\rho \cdot r} = \frac{\rho_G}{\rho_L - \rho_G} \frac{2\sigma}{r} \quad (2.15)$$

than the vapor pressure  $p_0$  at the flat phase boundary. As the surface tension  $\sigma$  is temperature dependent the curves for the vapor pressure  $p_G$  and the liquid pressure  $p_L$  do not run exactly but only approximately parallel to the vapor pressure curve  $p_0$  at the phase interface. If instead of stipulating the temperature  $T$ , the pressure  $p_0$  of a liquid-vapor bubble system is given, then the liquid has to be superheated by  $\Delta T = T - T_{sat}$  in comparison to the system with flat phase boundary, so that a vapor bubble of radius  $r$  is in equilibrium with liquid as shown in Fig. 2.8.

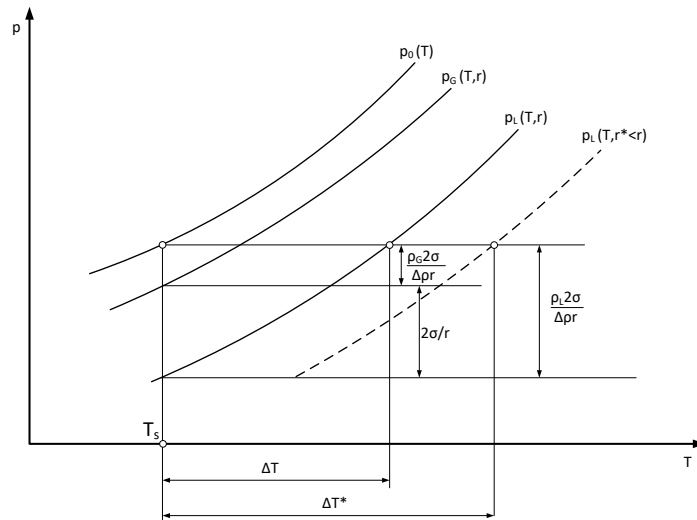


Figure 2.8: Steam and fluid pressure between liquid and one spherical vapor bubble [8].

In addition, it is clear that when the required degree of superheating  $\Delta T$  is larger; the radius  $r$  of the vapor bubble is the smaller, therefore, for small radii  $r^* < r$  the curves for the vapor pressure  $p_G(T, r^*)$  and the liquid pressure  $p_L(T, r^*)$  are shifted further to the right. Conversely for a given degree of superheating  $\Delta T$ , a vapor bubble of definite radius  $r$  is in equilibrium with the superheated liquid. For the approximate calculation

of the required superheating, we assume that the curves  $p_0(T)$  and  $p_L(T, r)$  in Fig 2.8 run parallel. This gives:

$$\frac{dp_L}{dT} = \frac{dp_0}{dT} \quad (2.16)$$

The differential  $dp_0/dT$  is the slope of the vapor pressure curve  $p_0(T)$ . It can be calculated from inverse formula of the Clausius-Clapeyron equation:

$$\frac{dp_0}{dT} = \frac{\Delta h_v}{T_{sat}(v_G - v_L)} = \frac{\Delta h_v \rho_G \rho_L}{T_{sat}(\rho_L - \rho_G)} \quad (2.17)$$

On the other hand, with (2.13):

$$\frac{dp_L}{dT} \cong \frac{p_0 - p_L}{\Delta T} = \frac{1}{\Delta T} \frac{\rho_L}{\rho_L - \rho_G} \frac{2\sigma}{r} \quad (2.18)$$

From these equations, the bubble radius  $r$  is calculated as a function of the superheating  $\Delta T = T - T_{sat}$ , with the simple assumption that the vapor can be treated as an ideal gas and that the specific volume of the liquid is negligible being really smaller compared to that of the vapor [9]:

$$r_{crit} \cong \frac{2\sigma T_{sat}}{\rho_G \Delta h_v \Delta T} \quad (2.19)$$

So, as it is possible to notice, under steady state conditions, the pressure in the bubble and hence the superheating temperature can be expected to vary directly with the inverse of the bubble radius. Supposing that the value of the radius is minimum, the superheat of the vapor nucleus will be maximal. According to this, for a particular degree of liquid superheating  $\Delta T$  a definite bubble radius exists, at which the bubble is in equilibrium with the liquid. Bubbles, whose radii are  $r^* < r_{crit}$ , are in equilibrium with the liquid only if the superheating  $\Delta T^* > \Delta T$ . A liquid superheated by  $\Delta T$  is too cold. Therefore, bubbles that are too small will condense again. Bubbles of radius  $r^* > r_{crit}$  are in liquid that is superheated, and they can continue to grow. However, in reality the residence time of bubbles, in particular those close to the wall, is so small that equilibrium is never reached, and the actual superheating of the fluid is many times

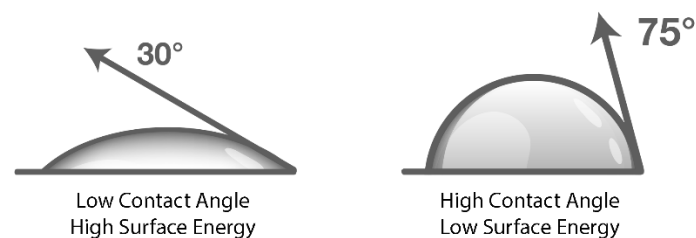
greater than  $\Delta T$ . Starting from the critical radius, derived from the equation subsequently described, it is possible to evaluate the necessary activation energy  $\Delta G_{max}$ , based on the change in Gibb's energy [6]:

$$\Delta G_{max} = \frac{4}{3} \pi \sigma r_{crit}^2 = \frac{16}{3} \pi \frac{\sigma^2}{(\rho_G - \rho_L)^2} \quad (2.20)$$

On the other side, the superheating of the surface is a function of the heat flux being transferred through the solid material to it. Usually, the surface of the solid material contains different nucleation sites and therefore, the number of activated nuclei, where bubbles are formed at the surface, is increasing with the higher heat flux. The increasing of the number of activated nuclei results in a more intensive fluid dynamic mixing of the liquid at the heated surface. Both together, namely the mass transport in the bubble in form of vapor and the microscopic turbulence with its drift flux behind the bubble improves the heat transfer conditions. After the bubble breaks off, further gas or vapor remains enclosed in the depression. This will be cooled by cold liquid flowing from the center of the fluid to the wall, and then subsequently, by additionally heating from the wall. A new nucleus for the growth of a vapor bubble forms. Bubble radius decreases with increasing superheat because the surface tension decreases with increasing temperature. It follows that for larger superheats more nucleation sites are involved in the formation of bubbles, at which small bubbles arise. These considerations explain why the surface structure is an influential quantity of heat transfer. Vapor bubbles always develop at favorable positions on solid surfaces or on suspended particles. Therefore, it is generally heterogeneous nuclei formation that prevails, as will be explained in chapter 3. In the literature, the bubble break-diameter is determined by a wide variety of equations. In this work the bubble break-off diameter is given, according to Fritz, by [10]:

$$d_B = 0.0149 \beta_0 \sqrt{\frac{2\sigma}{g(\rho_L - \rho_G)}} \quad (2.21)$$

In which the contact angle between the bladder and the heating wall is expressed with  $\beta_0$  and according to various experiments this is equal to  $45^\circ$  for water,  $1^\circ$  for low-boiling fluids and  $35^\circ$  for all other fluids. Equation 2.21 is applied for spherical bubbles. An increase in the tear-off diameter results from a reduction in pressure (see paragraph 5.1). With higher pressures for the same cavity considered, the meniscus will be in a lower position as in this case the surface tension will be smaller and therefore it is easier for the liquid to go downwards, in this way there is a greater surface in contact between liquid and vapor. Thus, the onset of nucleate boiling for highly wetting fluids is different from that of poor-wetting fluids. Wettability refers to the tendency of liquids to spread across a surface of interest. In general, surfaces on which the liquid tends to spread out, forming a flatter droplet, are described as having good wetting or high wettability. Surfaces on which liquid tends to “ball up” are described as having poor wetting or low wettability. In practice, these wettability categories are related to specific ranges of contact angle measurements, as defined in the diagram in Fig. 2.9.



*Figure 2.9: Illustrations of contact angle measurements on surfaces with high wettability and low wettability, respectively (<https://www.brighton-science.com/>).*

With highly wetting liquids there will be only a small number of active nuclei on a given surface then with poorly wetting liquids. This is due to the enhanced ability of fluids of small wetting angle to effectively flood the cavities. In highly wetting liquids the residual bubble will be small and therefore requires for its initial growth a maximum of superheats.

## 2.4 Calculation methods for nucleate boiling for smooth tubes

The nucleate boiling phenomenon has been studied extensively in the past. As a result, it is possible to find a great number of correlations in the literature involving several empirical constants and adjustable parameters with their interactions. Often these correlations have been useful with respect to their application and can give a first estimation for design or for safety issues, but the applicability diminishes as parameters of interest start to fall outside the range of physical parameters for which the correlations are developed. Theoretically a consistent calculation method for the heat transfer coefficient  $\alpha$  in nucleate boiling, which should be based on the physical phenomena connected with vapour bubbles growing, departing and slideing on the wall and with interactions of bubbles and of neighboring nucleation sites within the microstructure of the heating surface does not yet exist. Instead, the predictive methods for  $\alpha$  available in the literature at present are empirical or semiempirical, especially for heat transfer conditions relevant in practice. In the VDI-Heat-Atlas method, a relationship for a reduced heat transfer coefficient  $\frac{\alpha}{\alpha_0}$  on a single plain tube is established. With this method the relative influences on  $\alpha$  of the main groups of variables are treated separately considering: the operating parameters (namely the heat flux  $q$  and the pressure  $p$ ), the properties of the liquids and the nature of the heated surfaces as it is possible to notice from the equation 2.22 below:

$$\frac{\alpha}{\alpha_0} = F(p^*) \cdot F\left(\frac{q}{q_0}\right) \cdot F_{WR} \cdot F_{WM} \quad (2.22)$$

In which  $p^*$  is calculated from the ratio between the saturation pressure  $p_{sat}$  and the critical pressure  $p_{crit}$ . So, the function  $F(p^*)$  describes the influence of the saturation pressure,  $F\left(\frac{q}{q_0}\right)$  the influence of the heat flux,  $F_{WR}$  the influence of the roughness of the heating surface or the microstructure and  $F_{WM}$  the influence of the heating wall material. In this equation  $\alpha_0$  is the heat transfer coefficient for a specific fluid at a reference state that is the same for all fluids and  $F$  are independent non dimensional functions applicable to all fluids (with a very small number of exceptions). The

influence of the thermophysical properties of the boiling liquid is summarize in  $\alpha_0$ , which is related to the conditions  $q_0 = 20 \text{ kW}/\text{m}^2$ , for a reduced pressure  $p_0^* = p_{sat}/p_{crit} = 0.1$ . The reference state for the heater is defined as a copper cylinder with an intermediate value  $R_{\alpha_0} = 0.4 \text{ }\mu\text{m}$  of the arithmetic mean roughness height of the surface (as defined in ISO 4287 [11]), which lies within the common range for heater surfaces manufactured in practice with thermal conductivity  $\lambda_0$ , density  $\rho_0$  and the specific heat capacity  $c_0$ . This implies that  $\alpha_0$  have to be determined by experiments (e.g. Gorenflo et al, 2004) [12] or by the correlation by Stephan & Preusser (1978) [13] for pure liquids. For water, a reference value of  $\alpha_0 = 5600 \text{ W}/\text{m}^2\text{K}$  at  $\dot{q}_0 = 20 \text{ kW}/\text{m}^2$  was obtained from the VDI-Heat-Atlas. For fluids for which no suitable experimental data are available, Gorenflo recommended using Stephan and Preuss correlations, although greater uncertainties can be expected in the following prediction:

$$Nu = 0.1 \left[ \frac{\dot{q}_0 d_B}{T_S \lambda_L} \right]^{0.674} \left[ \frac{\rho_G}{\rho_L} \right]^{0.156} \left[ \frac{\Delta h_v d_B}{\alpha_L^2} \right]^{0.371} \left[ \frac{\rho_L \alpha_L^2}{d_B \sigma} \right]^{0.350} \left[ \frac{\mu_L C_{p,L}}{\lambda_L} \right]^{0.16} \quad (2.23)$$

The Nusselt number used for this equation is equal to:

$$Nu = \frac{\alpha_{0,calc} d_B}{\lambda_L} \quad (2.24)$$

Where the thermal conductivity of the liquid is indicated by  $\lambda_L$  and the characteristic length is evaluated through the bubble tear-off diameter  $d_B$  according to Fritz [10], as we can see from the equation (2.21). From the inversed formula of the equation 2.41 it is possible to evaluate  $\alpha_{0,calc}$ .

### 2.4.1 Effect of heat flux and pressure

The influence of the heat flux is determined by:

$$F\left(\frac{\dot{q}}{\dot{q}_0}\right) = \left(\frac{\dot{q}}{\dot{q}_0}\right)^{n(p^*)} \quad (2.25)$$

where  $n(p^*)$  is the slope of the straight line in the double-logarithmic diagram with  $\alpha$  as a function of the heat flux. The slope of the straight lines  $n$  decreases with the increasing of the pressure, because more and smaller nucleation sites in the surface are already activated with increasing superheat. The relative increase in the heat transfer coefficient  $\alpha$  with the heat flux becomes smaller with increasing saturation pressure. The pressure-dependent exponent  $n(p^*)$  is defined according to the VDI-Heat-Atlas by:

$$n(p^*) = a - bp^{*c} \quad (2.26)$$

The parameters  $a$ ,  $b$ ,  $c$  are adapted to a variety of measurements for organic liquids, water and helium. The inclination of the slopes for water is always lower than the inclination for the organic fluids. According to the second version of the VDI-Heat-Atlas, the regression lines are therefore steeper. The fitting parameters are listed in Table 2.1, as they vary depending on the references.

*Table 2.1: List of fitting parameters in Eq. (2.24) for the slope of the interpolation line of the  $\alpha$ - $q$  relationship.*

Boiling liquid	$a$	$b$	$c$	References
Organic fluid	0.9	0.3	0.3	<i>Gorenflo (2006)</i>
Organic fluid	0.95	0.3	0.3	<i>Gorenflo (2010)</i>
Organic fluid	0.93	0.26	0.37	<i>Luke (1996)</i>
Water, Helium	0.9	0.3	0.15	<i>(Gorenflo 2010)</i>



The influence of the saturation pressure along the vapor pressure curve is expressed by the function  $F(p^*)$  and is calculated from the reference value  $\alpha_0(p^*)$ , for organic liquids (Gorenflo 2006 [14]) with:

$$F(p^*) = 1.2p^{*0.27} + 2.5p^* + \frac{p^*}{1 - p^*} \quad (2.27)$$

and for water and helium with a slightly lower pressure dependence:

$$F(p^*) = 1.73p^{*0.27} + \left(6.1 + \frac{0.68}{1 - p^{*2}}\right)p^{*2} \quad (2.28)$$

A pressure dependence even more pronounced is observed in recent works on very uniformly structured copper tubes for organic liquids and now also considered in Gorenflo (2010 [1]):

$$F(p^*) = 0.7p^{*0.2} + 4p^* + \frac{1.4p^*}{1 - p^*} \quad (2.29)$$

In the first version the underlying investigations were primarily measurements with organic fluids and halogen refrigerants such as R12, R113 and R502. In the second version of VDI-Heat-Atlas [1], adjusting the correlation, it is possible to find investigations with further developed refrigerants, such as R134a R507. For low pressure ( $p^* < 0.05$ ), the pressure dependency of the heat transfer coefficient is less, while for high pressures ( $p^* > 0.5$ ) much more pronounced [3]. The empirical equation for the slope in the second version of the VDI-Heat-Atlas is based on the investigations by Siebert [15]. The upper limit for the validity of the equations shown in this paragraph is given by the value  $p^* = 0.9$ , because at this reduced pressure the measured values are scanty and are also unreliable owing to the very small superheat of the wall surfaces at these pressures. While, since in most of the papers water was used as the working fluid, the lowest pressure value considered was 0.03, since having the water a critical pressure of 221 bar results in a saturation pressure of 6 bar. Also, Stephan and Preusser built their theory considering a pressure value of 0.03 because using for example the refrigerant R134a, which has a critical pressure 40.6 bar, a value of 1.2 bar is obtained which is always higher or similar to the value of atmospheric pressure.

Table 2.2: Summary of the formulas for the calculation of the factors related to the dependance with pressure and heat flux, considering Gorenflo 2006 [14] and Gorenflo 2010 [1].

<b>COEFFICIENT</b>	<b>CALCULATION (GORENFLO 2006)</b>	<b>CALCULATION (GORENFLO 2010)</b>
$F(p^*)$	$F(p^*) = 1.2p^{*0.27} + 2.5p^* + \frac{p^*}{1-p^*}$	$F(p^*) = 0.7p^{*0.2} + 4p^* + \frac{1.4p^*}{1-p^*}$
$F_{\dot{q}} = \left(\frac{\dot{q}}{\dot{q}_0}\right)^{n(p^*)}$	$n(p^*) = 0.9 - 0.3p^{*0.3}$	$n(p^*) = 0.95 - 0.3p^{*0.3}$

#### 2.4.2 Effect of the properties of the fluid

From VDI-Heat-Atlas (Gorenflo 2010) it is possible to evaluate the heat transfer coefficient calculated at the reference condition:

$$\alpha_{0,calc} = 3.58P_f^{0.6}, \text{ with } P_f = (dp/dT)_{sat}/\sigma \quad (2.30)$$

where  $(dp/dT)_{sat}$  is the slope of the vapor pressure curve and  $\sigma$  is the surface tension, both at the reference pressure  $p_0^* = 0.1$ .

#### 2.4.3 Effect of the properties of the heater

In the following, the limited experimental evidence available at present is used to develop a preliminary method of representing separately the influences of the material of the heated wall and the roughness texture of its surface. The influence of the heating wall properties is given by the equation:

$$F_W = F_{WR} * F_{WM} \quad (2.31)$$

For this separation, it is essential to have an appropriate quantitative specification of the surface texture. Stephan (1963) [16] studied both horizontal cylinders and flat surfaces and found that a roughness exponent of  $m = 0.133$  was representative of both heater types:

$$F_{WR} = \left(\frac{P_a}{P_{a0}}\right)^{2/15} \quad (2.32)$$

where the reference value  $P_{a0} = 0.4 \mu\text{m}$  is the arithmetic mean roughness according to DIN EN ISO 4287 [11], of a sanded copper heating surface across the scores (i.e., in the direction of greatest roughness). Stephan based his correlation on experiments at high heat fluxes and near atmospheric pressure for different rough surfaces. Among the properties of the wall material, the thermal effusivity  $e = (\lambda \rho C_p)_w^{0.5}$  (the square root of the product of the material's thermal conductivity  $\lambda$ , the density  $\rho$  and the specific heat capacity  $C_p$ ) is particularly important for the transient conduction of heat in the wall to the active nucleation sites on its surface. From the data it can be concluded that the influence of the wall material may be represented very approximately by:

$$\alpha \propto (\lambda_w \rho_w C_{p,w})^{0.25} = e^{0.5} \text{ or } F_{WM} = \left(\frac{e}{e_{Cu}}\right)^{0.5} \quad (2.33)$$

$$F_{WM} = [(\lambda_w \rho_w C_{p,w} / (\lambda_0 \rho_0 C_{p_0}))^{0.25} \quad (2.34)$$

From the above, the function  $F_W$  can be written as:

$$F_W = \left(\frac{P_a}{P_{a0}}\right)^{2/15} \left[ \frac{\lambda_w \rho_w C_{p,w}}{(\lambda_0 \rho_0 C_{p_0})_{Cu}} \right]^{0.25} \quad (2.35)$$

It is convenient to use copper as a reference wall material because most of the data in literature were measured with copper heaters. The geometrical characteristics of the wall, such as the diameter of horizontal tubes, do not appear in  $F_W$ . There are other equations for the calculation of the heat transfer coefficient, like the Borinshanski-Mostinski equation in which  $\alpha$  is a function of  $\dot{q}/A$ , of the reduced pressure  $p^*$  and of the critical pressure  $p_{cr}$ :

$$\alpha = A^* \cdot F(p^*) \cdot (\dot{q}/A)^{0.7} \quad (2.36)$$

$$A^* = 0.1011 \cdot p_{cr}^{0.69} \quad (2.37)$$

$$F(p^*) = 1.8p^{*0.17} + 4p^{*1.2}10p^{*10} \quad (2.38)$$

When designing boilers in pool boiling, it is suggested to use only the first term on the right side of the above equation:

$$F(p^*) = 1.8p^{*0.17} \quad (2.39)$$

Another widely used equation is that by Cooper based on extensive data that expresses the heat transfer coefficient during nucleate boiling (pool boiling) as a function of the roughness term, the heat flux, the reduced pressure and the molecular weight [17]:

$$\alpha = C \cdot 55 \cdot p^{*(0.12-0.2 \cdot \log Rp)} \cdot (-\log p^*)^{-0.55} \cdot M^{-0.5} \cdot \dot{q}^{0.67} \quad (2.40)$$

where  $R_p$  is the surface roughness [ $\mu\text{m}$ ],  $M$  is the molecular weight [g/mol] and  $C$  is the material constant equal to 1.7 for copper and 1 for stainless steel. In this equation the roughness influence is not really considered separately from the other influence parameter. So, in this equation the heat transfer coefficient  $\alpha \propto \dot{q}^{0.67}$  is multiplied by a constant  $K_{nb}$  that depends on the reduced pressure, the molecular weight and on the reduced pressure. Changing the evaporation temperature, also the reduced pressure is going to be modified, so I will have different value of this constant. The effect of the saturation temperature and so the reduced pressure is more visible at low vapor quality, where the nucleate boiling is more important. When the reduced pressure increases also the heat transfer coefficient increases. This equation can be used for a range of the reduced pressure between 0.08 and 0.9 and a surface roughness  $0.22 \mu\text{m} < R_{p,old} < 4.31 \mu\text{m}$ . It should also be noted that  $R_{p,old}$  (old reference value for the emery ground copper surface) used in the Cooper correlation is defined by DIN 4762/1960, while Gorenflo suggested the conversion  $R_a \approx 0.4 R_{p,old}$  which is adopted in this work.

## 2.5 Calculation method for finned tubes

The macroscopic shape of the heating surface enhances or hinders the movement of the liquid and the upstreaming bubbles by its shape and arrangement in the evaporator. This results in additional convection effects which influences the bubble formation and the heat transfer locally differently. The evaporation process can be improved using finned surface as known for long time ([19] [20]). To consider the influence of the fins structure are available numerous research work, which relates to different geometries:

- Conventional finned tubes with rectangular or trapezoidal shape fins geometry.
- Heavy duty tubes (Y or T shaped fins with different coatings).

The following equations are alternative calculation approaches for conventional rib structures since the measurements in this work will be processed with them.

### 2.5.1 Calculation according to Gorenflo

In this analysis a low finned tube GEWA-K30 in stainless steel is used. The number after the letter K is the equal to the number of fins per inch, so in this case in 1 inch (equal to 25.4 mm) there are 30 fins. Within the range of initial nucleate boiling where the heat flux is low, horizontal evaporator tubes with the external fins transfer heat more efficiently than smooth tubes (as will be confirmed by the experimental data in paragraph 5.2). As a consequence, the exponent  $n$  should be less than that for a plain tube, and the pressure dependence of  $F(p^*)$  will be weaker. To account for the influence of the fins there is a modified version of the equation used for the effect of heat flux. The new relationship, according to [1], is equal to:

$$n_f(p^*) = n_p(p^*) - 0.1 \frac{h}{t_l} \quad (2.41)$$

where  $n_f(p^*)$  and  $n(p^*)$  are the indices in the terms for the finned and plain tubes respectively. In this equation there is an additional term consisting of the ratio between the height of the fins  $h$  and the free space between the fins  $t_l$ . Further measurements show that the pressure influence is reduced due to the fins, and it can be expressed with

the help of the ratio between the reduced pressure and the square root of the increase in area  $\varphi$ , using the following equation:

$$F_{f,p^*} = F(p^*/\sqrt{\varphi}) \quad (2.42)$$

where  $\varphi$  is the ratio of the surface area of the finned tube to that of a plain tube of the same core diameter. The VDI-Heat-Atlas [1] can only be used for copper pipes with free fin spacing of  $t_l \geq 1 \text{ mm}$  and in a pressure range of  $0.02 \leq p^* \leq 0.3$  (or from somewhat below 1 bar to not much above 10 bar). The calculation of the normalized heat transfer coefficient  $\alpha_0$  is the same as for smooth tube, according to Stephan Preusser [13]. A fact that can be exploited in estimating the reference value  $\alpha_{0,f}$  for finned tubes is that the heat transfer coefficients for both finned and plain copper tubes are approximately the same at a heat flux of about  $100 \text{ kW/m}^2$  and a reduced pressure equal to 0.1:

$$\alpha_{100,f} = \alpha_{100,p} \text{ at } q = 100 \frac{\text{kW}}{\text{m}^2} \text{ and } p_0^* = 0.1 \quad (2.43)$$

### 2.5.2 Calculation according to Slipcevic

A correlation created using dimensional analysis to calculate the heat transfer in nucleate boiling on single finned tubes was studied by Slipcevic and Zimmermann [2]. After further experimental investigations on various halogen refrigerants, Slipcevic published an empirical dimensionless equation for the calculation of the heat transfer in which the heat transfer coefficient used is equal to:

$$\alpha = \alpha_{real} \left[ 1 - (1 - \eta_f) \frac{A_f}{A_T} \right] \quad (2.44)$$

The calculation of the heat transfer coefficient requires the real heat transfer coefficient, which takes into account also the heat conduction in the fins, the  $\eta_f$  efficiency and the ratio between the finned area  $A_f$  to the total area  $A_T$ .

To determine the real heat transfer coefficient, it is necessary to start from the definition of Nusselt number:

$$Nu = \frac{\alpha_{real} \cdot d_B}{\lambda_L} \quad (2.45)$$

and a constant:

$$K_B = \frac{Cp_{,L} \cdot \rho_G \cdot \Delta h_v \cdot \dot{q}^2}{g^2 \cdot T_{sat} \cdot \lambda_L^2 \cdot \rho_L} \quad (2.46)$$

When boiling on single finned tubes, the following new equation is proposed:

$$Nu = 6.3 \cdot 10^{-4} \cdot \varphi \cdot K_B^{1/3} \quad (2.47)$$

Where the area increase is represented by the parameter  $\varphi$ . This equation can only be used in the interval  $2.5 \leq \varphi \leq 4$  and cannot be used for tubes with  $\varphi$  tending to 1. For practical calculations the equation [2.48] can be written in the simple form:

$$\alpha_{real} = S_B \cdot \varphi \cdot \dot{q}^{2/3} \quad (2.48)$$

The temperature drop required by the heat conduction in the fins is due to the dimensionless correction factor relationship:

$$S_B = \frac{6.3 \cdot 10^{-4} \cdot \lambda_L}{d_B} \cdot \left[ \frac{Cp_{,L} \cdot \rho_G \cdot \Delta h_v}{g^2 \cdot T_{sat} \cdot \lambda_L^2 \cdot \rho_L} \right]^{1/3} \quad (2.49)$$

This depends on the material properties, the boiling temperature  $T_{sat}$  of the refrigerant and it is dependent on the bubble break-off diameter. Furthermore, to calculate the heat transfer coefficient  $\alpha$  the fin efficiency is defined as:

$$\eta_f = \frac{\tanh X}{X} \quad (2.50)$$

The change is due to the finned surface, or the fin height of temperature defined by the variable:

$$X = h_R \sqrt{\frac{2\alpha_{real}}{b \cdot \lambda_f}} \quad (2.51)$$

where the reduced height is defined as:

$$h_R = h \cdot \left(1 + 0.35 \cdot \ln \frac{d_o}{d_c}\right) \quad (2.52)$$

that it is calculated taking into account the quotient of the outer diameter  $d_o$  to the core diameter  $d_c$ . For the finned area  $A_f$  required in equation  $F_R$ , the equation applies:

$$A_f = \frac{1}{2t_l} \pi (d_o^2 - d_c^2) \quad (2.53)$$

Along with the base area:

$$A_b = \frac{t_l - b}{t_l} \cdot d_c \cdot \pi \quad (2.54)$$

In this way they form the total exchange area of the finned tube equal to:

$$A_T = A_b + A_f \quad (2.55)$$



### 3. SURFACE ANALYSIS

The bubble formation within favored cavities of the surface is one of the main mechanisms of the nucleate boiling heat transfer. The microscopic (roughness) and macroscopic structure (geometry) with its elevations and cavities directly influences the wetting of the heating surface by the fluid and thus the formation of bubbles and consequently the heat transfer. The cavities for the activation of the bubble nucleation sites depend on the operating parameters as superheat and saturation pressure. Some large cavities are only activated for low superheat and low pressures; the small cavities become of interest for high superheat and higher pressures, as will be shown with the use of high-speed recordings. Heating elements like tubes, plates and sheets show a technical rough structure due to manufacturing process. The structures mainly fall into two groups: deterministic with orderly separated grooves such as those with turned or emery grinded surfaces with regularly oriented grooves and stochastic such as sandblasted surfaces with statistically distributed peaks and cavities. In the case that is going to be considered, there are different tubes with the same dimensions but with different materials (copper and stainless-steel). Observing the two tubes, they appear homogeneous, but with a specific analysis, from the microscopic point of view, it is possible to understand that the two smooth tubes present stochastic behavior, because they are characterized by the presence of numerous cavities with different dimensions that occupied completely casual positions inside the material. In addition, it is possible to classify three ranges that characterized the roughness of a surface:

- $P_a^1 = 0.1 \div 1 \mu\text{m}$  smooth/polished surfaces
- $P_a = 1 \div 2 \mu\text{m}$  rougher than smooth surfaces
- $P_a = > 8 \mu\text{m}$  rough surfaces

---

<sup>1</sup> In scientific representation and literature  $P_a$  is chosen, for practical belongs it is usual to take  $R_a$ , because simple roughness measurement instruments used in general in manufacturing process do not offer the possibility to have values with the cut-off.

### **3.1 Surface treatment**

This chapter first addresses the sandblasting process, to achieve the desired roughness of the examined pipe sample. This is followed by a description of the optical measurement device with the corresponding measurement results of the surface for the copper and stainless-steel smooth tubes and finned stainless-steel tube considered and analyzed in the paragraphs below.

#### **3.1.1 Operating principle of the sandblasting system**

For the experimental investigation of the roughness influence on heat transfer in nucleate boiling, sandblasting is one of the mechanical surface treatment methods more used for achieving the desired roughness of the pipe. The structure and in particular the roughness can be varied by changing the sandblasting parameters, such as the blasting pressure or the blasting medium. From the literature is known that an increase in the roughness leads to an improvement in the heat transfer coefficient. So, for this reason, it is possible to increase the surface roughness and thus the number of indentations through sandblasting. The surface treatment of the materials (copper and stainless steel) is made using the sandblasting system from the company “Auer Technology for Surface Treatment” type ST 1200 J. The sandblasting plant essentially consists of four main components, as it is possible to see from Fig. 3.1: jet nozzle, funnel with suction pipe, rotatable clamping device and linear feed device. The jet unit consists of a mixing chamber and the injector jet nozzle with a diameter equal to 8 mm, which is placed vertically above the pipe. The injector jet nozzle has a downward opening for accelerating the blasting material out of the nozzle using compressed air. The size of the nozzle will vary depending on the grit of the used blasting agent selected. With the help of the electrically operated displacement device move the nozzle in a horizontal direction over the workpiece, with a velocity constant equal to  $v_D = 4.6$  mm/s. To start up the system it is necessary to use compressed air which allows the sand to go out from the injector. For this reason, according to the literature, it is necessary to set an air pressure value of 1.4 bar. After having switched on the device, it is possible, by keeping

the pedal pressed, to move the nozzle forward and backward. The funnel located at the bottom of the plant is used for collecting the blasting material and then through a supply line with a filter it is possible to feed again the mixing chamber with the cleaned sand.

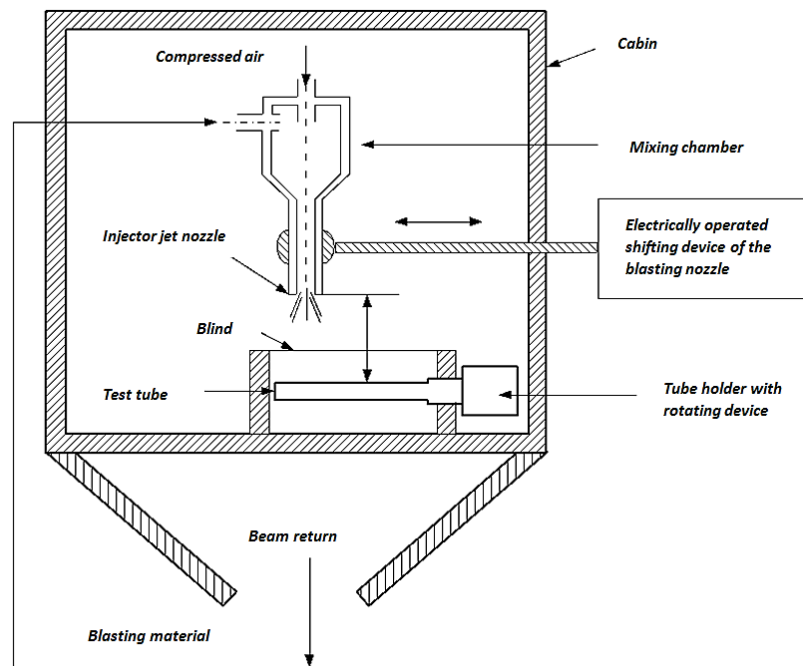
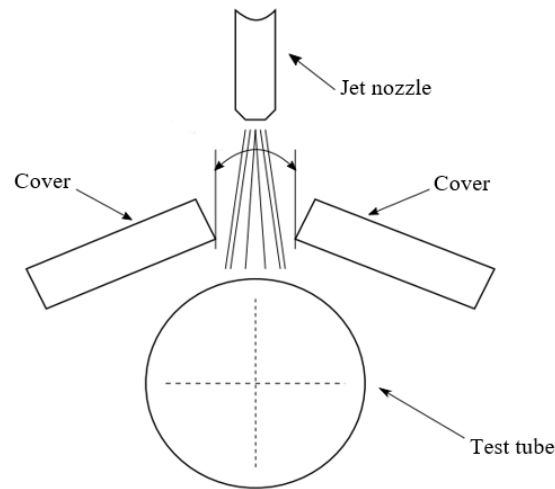


Figure 3.1: Schematic representation of the sandblasting system [21].

An additionally installed tube holder allows the tube to be positioned perpendicularly to the blasting nozzle during the sandblasting process. Furthermore, the pipe holder has a rotating device that is used for turning the tube to ensure that the process takes place equally around the entire tube. The total number of steps is 20, so it is possible to divide  $360^\circ$  in 20 steps, obtaining  $18^\circ$  for each step. In the case considered it will be performed the rotations corresponding to the angles:  $0^\circ$ ,  $5^\circ$  ( $5^\circ \times 18^\circ = 90^\circ$ ),  $10^\circ$  ( $10^\circ \times 18^\circ = 180^\circ$ ),  $15^\circ$  ( $15^\circ \times 18^\circ = 270^\circ$ ),  $19^\circ$  ( $19^\circ \times 18^\circ = 342^\circ$ ). For preparing the tube, the sample is placed in the tube holder and with a plumb it is aligned vertically respect to the jet nozzle above the pipe. The blasting material thus hits the set azimuthal position of the tube and is evenly distributed over the area. The distance between the test tube and the nozzle is 180 mm.



*Figure 3.2: Schematic representation of the aperture [21].*

The sandblasting agent used is corundum (EKF), a crystalline form of aluminum oxide ( $\text{Al}_2\text{O}_3$ ) with angular grain. It will be in the grain sizes EKF 400 with a grain diameter between  $d_p = 8\text{-}32 \mu\text{m}$  and EKF 120 with  $d_p = 90\text{-}125 \mu\text{m}$  used. Chemically it is composed of 97.7 % white nonferrous aluminum oxide ( $\text{Al}_2\text{O}_3$ ), 0.02% sodium oxide ( $\text{Na}_2\text{O}$ ), 0.04% iron oxide ( $\text{FeO}_3$ ) and 0.01 % calcium oxide ( $\text{CaO}$ ) together. Some characteristics of this blasting media is the high hardness and the brightness. To obtain as desired a “fine” roughness (around  $0.4 \mu\text{m}$ ) we have to consider the influence of different parameters:

- jet pressure,
- distance pipe to nozzle,
- opening diameter of the jet nozzle,
- material of the surface to be processed,
- grain size and shape of the blasting agent used,
- travel speed of the jet nozzle,
- angle of the jet nozzle.

### 3.2 Surface analysis using optical measurement technology

The surface topographies to be examined in this work are determined using the optical measuring device "Alicona InfiniteFocus", see Fig. 3.3, which is based on the principle of the focus variation and so the conversion of optical signal to electrical one.



*Figure 3.3: Graphic representation of the Alicona InfiniteFocus measuring device [6].*

The InfiniteFocus from Alicona is one of the high-resolution universal 3D surface measuring devices, which uses the focus variation method (ISO norm 21278). The measuring device combines the function of a regular surface measuring system with those of a micro coordinate measuring machine. Through this can measure shapes and roughness with a vertical resolution (z-axis) down to 10 nm, which corresponds to the requirements of the standard DIN EN ISO 4287 [11]. A white light source emits a ray of light that hits a semi-transparent mirror and turns 90° deflected so that the light hits the sample surface perpendicularly and it is reflected. Depending on the surface finish, the light rays are steered in different directions and recorded by the CCD sensor of the measuring device. To create a three-dimensional measurement with an associated color image, it is used along the optical axis a calculation algorithm, from the sensor data.

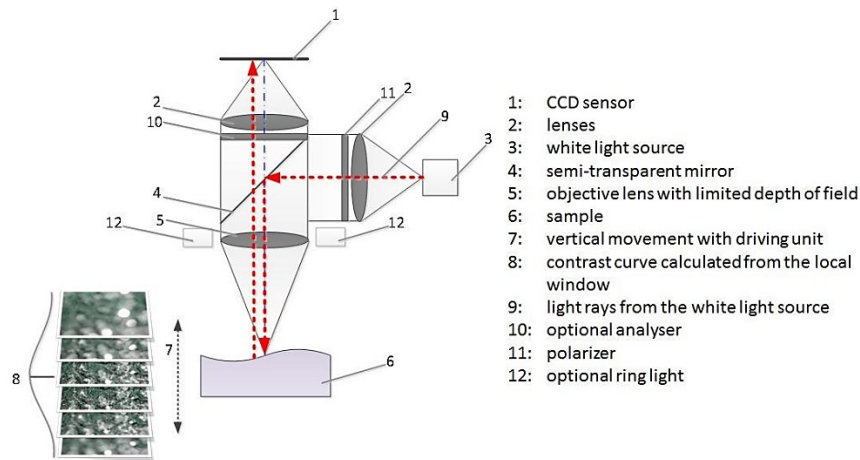


Figure 3.4: Schematic representation of the function of the measuring device [6].

### 3.2.1 Measuring principle of the optical measuring device

In the first step, the surface of the test tube is cleaned with isopropanol and then dried with a heat gun to dry the pipe and remove impurities on the surface. The tube is then clamped in a holder and aligned under the lens. The operating principle of the optical measuring device is based on the evaluating method of focus variation and the associated scanning system. The optical component has special lens with a total of five lenses, from 5x to 100x magnifications. A lens with a 50x magnification is used for the smooth tubes, even if in this case the area that is going to be considered it will be smaller. This is done because, in this case, if it is used 20x the resolution of the roughness on the vertical axis is not enough. Regarding the finned tube, a magnification of 20x is used to measure roughness, while for the geometry, a magnification of 5x is applied. For the smooth tube, 10 roughness measurements are taken in the axial direction and 12 measurements were taken around the circumference, whereas for the finned tube 4 measurements are taken for the geometry and 10 measurements are taken for measuring the roughness. The first topography recording is taken over the first thermocouple and to accommodate the remaining thermocouples, which are spaced 30° apart, the pipe is readjusted for each measuring point under the lens. The device is going to work between two limits (upper and lower limit), in which starting the recording from the lower one, it captures a large number of pictures, until it will reach the upper limit where it is able to obtain one single sharp photo, given by the union of all the

previous ones. This is a very accurate tool because it gives a 3D picture developed in the three coordinates x, y and z. The sensor settings, such as contrast and exposure time, are redefined for each measurement. In the next step, the raw data can be processed and evaluated using the “MoutainsMap” program.

### **3.3 Parameters of surface analysis according to standard**

The roughness influence on the heat transfer in nucleate boiling has hitherto been described in various empirical calculations by two types of parameters: "two-dimensional" and "three dimensional" methods. In this analysis it will be considered only the two-dimensional parameters. As can be seen from table 3.1, several parameters can be defined: the arithmetic average roughness  $P_a$  that gives the average of all ordinate values  $Z(x)$  along a single measurement section, the root mean square  $P_q$  that is the square mean roughness of the ordinate values along a single measurement section, the smoothing depth  $P_p$  that describes the height of the largest profile peak in relation to the center line of a single measuring section, the mean smoothing depth  $P_{pm}$  that represents the smoothing depths of five equal areas within the individual measurement sections formed. In addition, the parameter  $P_t$  describes the overall height of the profile and corresponds to the vertical distance between the highest and the lowest point of the profile within a single measurement section, while the parameter  $P_z$  is calculated as the mean of the five highest profile peaks and five deepest profile valleys. This results in the greatest height of the profile  $P_z$  as the mean value five sections. The roughness parameters are standardized according to DIN EN ISO 4287. The indicated arithmetic mean roughness value  $P_a$  is one of the most important parameters and it is often used in the literature to calculate the heat transfer in nucleate boiling.

Table 3.1: Overview of the two-dimensional roughness parameters according to the standard [3].

<b>Two-dimensional Parameters according to DIN EN ISO 4287</b>	<b>Description</b>
$P_a = \frac{1}{x} \int_0^l  Z(x)  dx$	Arithmetic average roughness: absolute values of the ordinate values $Z(x)$ at any position $x$ within a reference distance $l$ .
$P_q = \sqrt{\frac{1}{x} \int_0^l  Z(x) ^2 dx}$	Square mean roughness: it is similar to $P_a$ , higher sensitivity for peaks and scratches.
$P_p = \max(Z_i)$	Smoothing depth: Distance between the largest profile peak and the centerline.
$P_{pm} = \frac{1}{5} \cdot \sum_{i=1}^5 P_{pi}$	Average smoothing depth: distance from the highest peak to the center line in one in reference route divided into five sections.
$P_v = \min(Z_i)$	Depth of the largest profile valley: it shows the largest profile valley in relation to the center line.
$P_t = \max(Z_i) + \min(Z_i)$	Total height of the profile: sum of the highest profile peak and the lowest profile valley.
$P_z = \frac{1}{5} \cdot \sum_{i=1}^5 Z_i$	Average roughness: calculated mean of the five highest profile peaks and five deepest profile valleys.



### 3.4 Results of the roughness analysis of the treated tubes

In this chapter, the values obtained from the roughness measurements for the two fine sandblasted smooth tubes and the geometry and roughness measurements for the finned tube are shown in tables and graphs.

#### 3.4.1 Roughness results of the stainless-steel plain tube

In particular, this paragraph first refers to the roughness measurements of the smooth tubes, where a distinction is made between measurements in the axial direction and in the radial one. While in chapter 3.4.2 it will be analyzed the form and the roughness measurements of the finned tube. For a better overview, the surface measurements carried out with the respective placements and the number of measuring points are listed in Table 3.2.

*Table 3.2: Placement of the measurement's objects and number of measurement points.*

<i>Measurement object</i>	<i>Type of measurement</i>	<i>Alignment of measurement object</i>	<i>Number of measuring points</i>
smooth tube	roughness	axial	10
smooth tube	roughness	radial	12
finned tube	form	axial	4
finned tube	roughness (rib)	axial	3
finned tube	roughness (flank)	axial	4
finned tube	roughness (volley)	axial	3

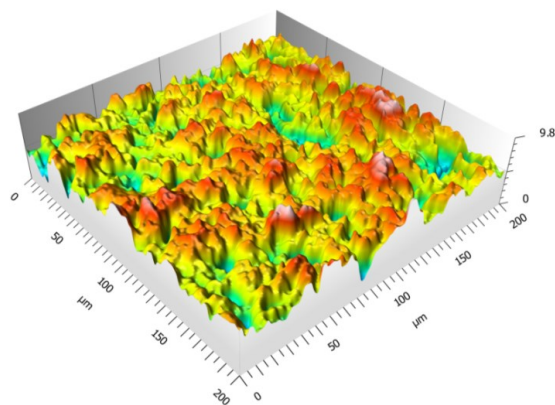
Table 3.3 contains the roughness parameters of the two fine sandblasted copper and stainless-steel tubes.

*Table 3.3: 2D roughness parameters of the fine sandblasted pipes according to the standard DIN EN ISO 4287 [11] for an area of 500  $\mu\text{m}$  x 500  $\mu\text{m}$ .*

<b>Test tube</b> <b><math>\varnothing</math></b> <b>[mm]</b>	<b>Material</b> <b>[–]</b>		<b><math>P_a</math></b> <b>[<math>\mu\text{m}</math>]</b>	<b><math>P_q</math></b> <b>[<math>\mu\text{m}</math>]</b>	<b><math>P_p</math></b> <b>[<math>\mu\text{m}</math>]</b>	<b><math>P_t</math></b> <b>[<math>\mu\text{m}</math>]</b>	<b><math>P_{pm}</math></b> <b>[<math>\mu\text{m}</math>]</b>	<b>Number of measurements</b>
<b>19.05</b>	<b>copper</b>	Mean	1.06	1.33	2.78	6.34	2.78	25168 measurements from 22 points
		Max	1.97	2.50	6.79	14.33	6.79	
		Min	0.55	0.68	1.23	3.18	1.23	
		$\sigma$	0.23	0.29	0.77	1.46	0.77	
<b>19.05</b>	<b>Stainless-steel</b>	Mean	0.70	0.89	2.14	4.48	2.14	25168 measurements from 22 points
		Max	1.31	1.67	5.99	10.12	5.99	
		Min	0.30	0.37	0.79	1.88	0.79	
		$\sigma$	0.15	0.19	0.62	1.08	0.62	

Table 3.3 shows that the copper smooth tube has an average arithmetic mean roughness value  $P_a$  of 1.06  $\mu\text{m}$  and the stainless-steel smooth tube has a value of  $P_a$  equal to 0.70. It is thus possible to see, given the range shown above, that the values obtained are good because these two values are more or less in the range between 0.4 and 1  $\mu\text{m}$ . The value in which we are more interested in is the standard deviation, because using the standard deviation  $\sigma$  it is possible to evaluate a statement about the homogeneity of the surface. To correctly describe a variable, it is not sufficient to use a statistical average such as the arithmetic mean or median because these indices provide only a partial view of the variable. You also need to use an index of variability, such as the standard deviation because the position index allows to get an idea of what is happening in the central part of the distribution, not in the other parts of the distribution. The more variability there is among the measurements, the greater the deviations from the mean, the greater the sum

of the squares and, therefore, the higher the value of the standard deviation. For this reason, for very small standard deviations we have for example a very homogeneous surface, while at higher standard deviations the surface is more inhomogeneous. As it is possible to see from the table above, the standard deviation has a value equal to 0.23 for the copper tube and a value equal to 0.15 for the stainless steel, so the second one has a more homogeneous surface. It can be notice that the stainless-steel pipe has a lower roughness values compared to copper. This is because the stainless-steel tube has higher strength and thus the same sandblasting conditions as for copper lead to a lower roughness, even if they are both small values. From the row data obtained from the optical device, considering only one measurement as an example, it is possible to obtain a 2D diagram of the measured section. After converting it into a 3D representation using the MountainMap software, it can be seen that there is an inclination of the plane, so it is necessary to use a command to remove the shape and thus obtain a profile in the same plane. It is now possible to extract a profile of the series that contains all the measurements taken and from which it is possible to see if there are any peaks or holes within the area in question that are too pronounced and would distract from the result obtained. To conclude the analysis in this way, it is possible to extract an individual profile of the area under consideration. For greater clarity of the above explanation, two examples for the third axial measurement for the roughness of the smooth copper pipe and the fifth axial measurement for the roughness of the smooth stainless-steel pipe are shown in the figures below (Fig. 3.5 - 3.8).



*Figure 3.5: Surface topography of the third measurement in the axial direction of the smooth copper tube (image captured via MountainsMap Universal).*

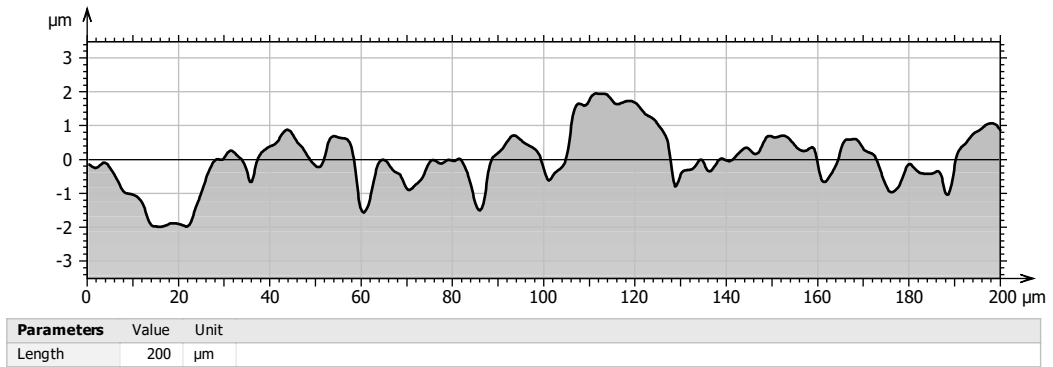


Figure 3.6: Two-dimensional profile cross section of the third measurement in the axial direction of the smooth copper tube (diagram captured via MountainsMap Universal).

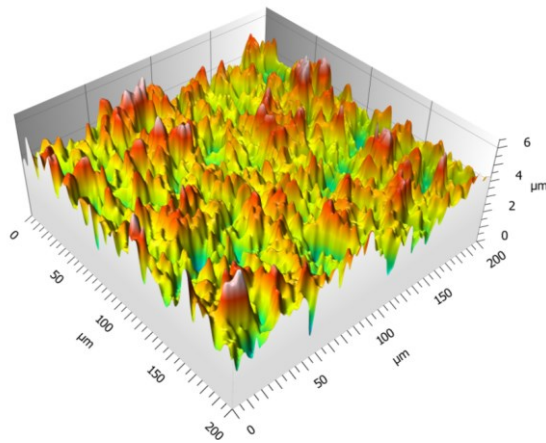


Figure 3.7: Surface topography of the fifth measurement in the axial direction of the smooth stainless-steel tube (image captured via MountainsMap Universal).

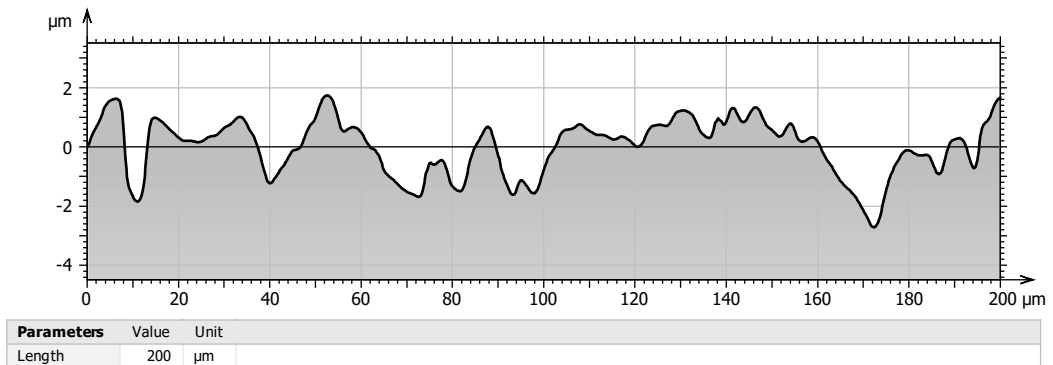


Figure 3.8: Two-dimensional profile cross section of the fifth measurement in the axial direction of the smooth stainless-steel tube (diagram captured via MountainsMap Universal).

### 3.4.2 Shape and roughness results of the stainless-steel finned tube

The following values of the form and roughness measurements refer to the tube with embossed rib geometry. Table 3.4 gives the average values of the four shape measurements. Fig. 3.9 is shown in order to have more clarity of the variables considered in table 3.4.

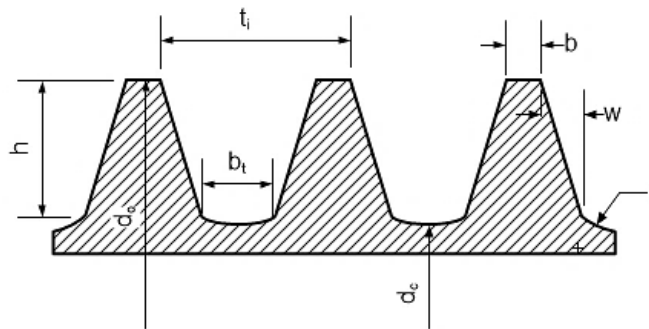


Figure 3.9: Representation of an exemplary rib geometry [7].

Table 3.4: Results of the form measurements of the finned tube.

	<b>h</b> [mm]	<b>t</b> [mm]	<b>b<sub>t</sub></b> [mm]	<b>b</b> [mm]	<b>w</b> [mm]	<b>r<sub>b</sub></b> [mm]
<b>Beginning</b>	0.53	0.79	0.38	0.35	0.04	0.25
<b>Center</b>	0.52	0.86	0.41	0.35	0.04	0.26
<b>End</b>	0.49	0.87	0.41	0.34	0.04	0.24
<b>In total</b>	0.51	0.84	0.40	0.35	0.04	0.25

The geometry data of the rib structure are determined by collecting data at different sections of a measurement area, inclining the tube during measurement to get a better view of the fins. As can be seen in Table 3.4, four values were taken in three different positions of the pipe at the beginning at the center and at the end each one for each three steps as we can see from Fig. 3.10.

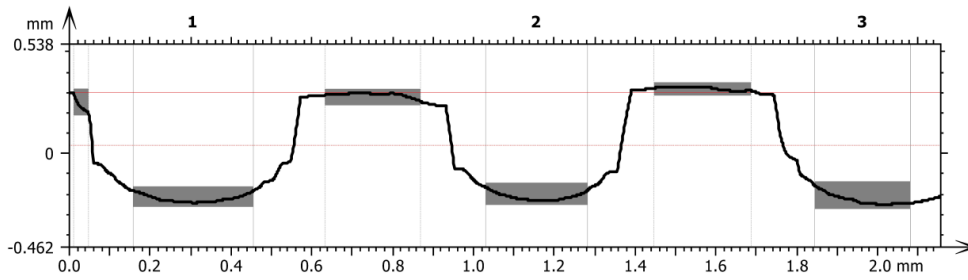


Figure 3.10: Representation of the steps for the measurement of the geometry of the rib geometry (image captured via MountainsMap Universal).

The rib height  $h$  is equal to 0.51 mm, the rib pitch  $t$  is 0.84 mm and the clear rib spacing is  $b_t = 0.4$  mm. Furthermore, the rib width is given as  $b = 0.35$  mm, the distance between the base and rib tip  $w$  as 0.04 mm and the radius  $r_b$  as 0.25 mm.

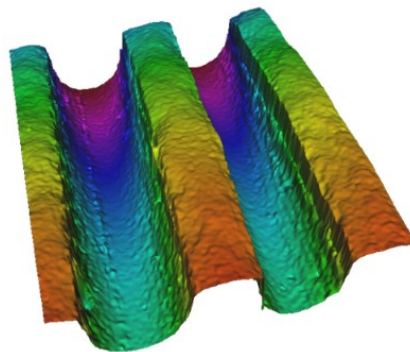


Figure 3.11: Three-dimensional surface topography of the fourth form measurement (image captured via MountainsMap Universal).

In the three-dimensional topography, shown in Fig. 3.11, different colors can be seen depending on the area. At the beginning, the area in the valley is yellowish, greenish in the middle and deep blue at the end due to different altitude values. After having analyzed the values referring to the geometry, the roughness of the pipe is analyzed as previously done with the smooth pipe. The roughness results are shown in Table 3.5.

Table 3.5: Roughness data evaluated according to DIN EN ISO 4287 [10] for the finned tube, measuring point positioned on the fin tip.

	<b>P<sub>a</sub></b> [μm]	<b>P<sub>q</sub></b> [μm]	<b>P<sub>p</sub></b> [μm]	<b>P<sub>t</sub></b> [μm]	<b>P<sub>pm</sub></b> [μm]	<b>Number of measurements</b>
<b>Mean</b>	1.00	1.25	2.27	5.28	2.27	1371 measurement runs measured at 3 positions
<b>Max</b>	2.00	2.61	4.81	10.94	4.81	
<b>Min</b>	0.27	0.35	0.49	1.42	0.49	
<b>Standard deviation</b>	0.32	0.39	0.82	1.76	0.82	

A total of 1371 measurement runs are recorded to determine the roughness parameters. From these, the mean, max and min values, and the standard deviation are calculated for each two-dimensional roughness parameter. According to Table 3.5, the arithmetic mean roughness value  $P_a$  is equal to 1.00 μm, the square mean roughness value  $P_q = 1.25$  μm and is therefore increased by 25%. The following figures in Fig. 3.12 and Fig. 3.13 illustrate the surface topography and a two-dimensional profile cross section of the first measurement on the rib tip.

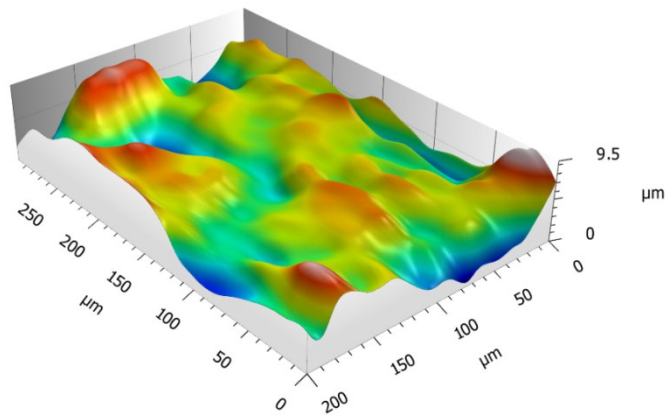


Figure 3.12: Surface topography of the first measurement on the rib tip (image captured via MountainsMap Universal).

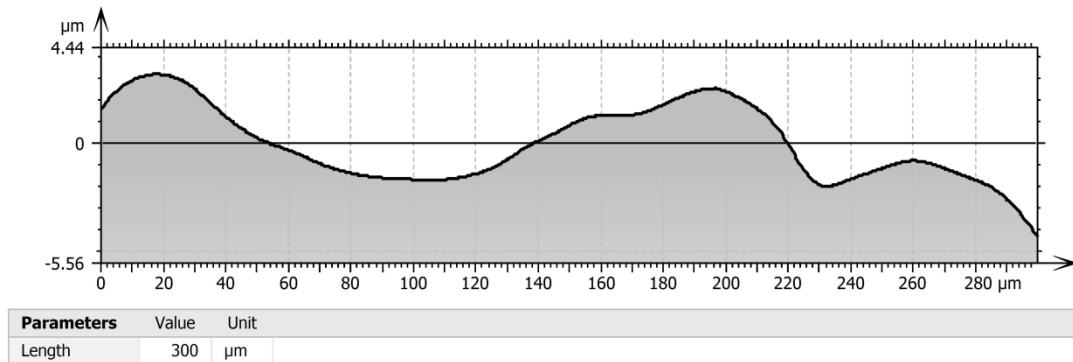


Figure 3.13: Two-dimensional profile cross-section of the first measurement on the rib tip (diagram captured via MountainsMap Universal).

The roughness structure of the first measuring point shows that peaks and grooves are distributed stochastically. In the profile cross-section extracted from the topography, extremes and low points, in which gas and vapor residues, can be deposited can be seen. Table 3.6 shows the parameters of the roughness measurements on the rib flank. For this purpose, four measurements are carried out with the optical measuring device Alicona Infinite Focus.

Table 3.6: Roughness data evaluated according to DIN EN ISO 4287 [11] for the finned tube, measuring point positioned on the fin flank.

	$P_a$ [µm]	$P_q$ [µm]	$P_p$ [µm]	$P_t$ [µm]	$P_{pm}$ [µm]	Number of measurements
<b>Mean</b>	0.98	1.23	2.86	5.73	2.86	574 measurement runs measured at 4 positions
<b>Max</b>	2.39	2.92	7.29	12.76	7.29	
<b>Min</b>	0.38	0.47	0.99	2.11	0.99	
<b>Standard deviation</b>	0.46	0.56	1.26	2.21	1.26	

Using 574 measurement runs, the values of the individual measurements are combined. From these, the mean value, maximum and minimum value, as well as the standard deviation sigma for the various roughness parameters are then determined. The arithmetic mean roughness value  $P_a$  is 0.98 µm; the square mean roughness value  $P_q$  has a value equal to 1.23 µm, so it is increased by approx. 25%. Fig. 3.14 and 3.15 are



shown below to illustrate the surface structure two-dimensional profile cross section of the first measurement on the flank.

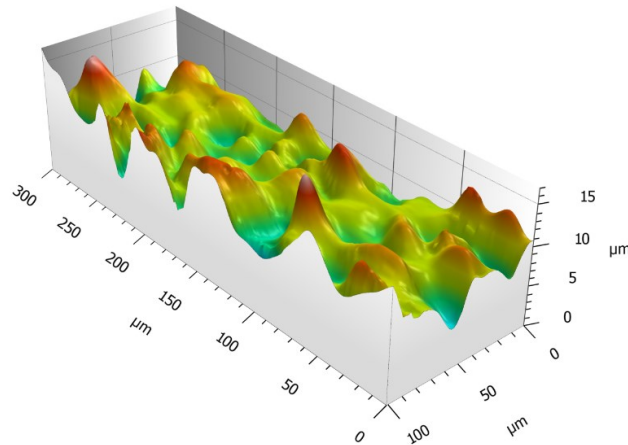


Figure 3.14: Surface topography of the first measurement on the flank (image captured via MountainsMap Universal).

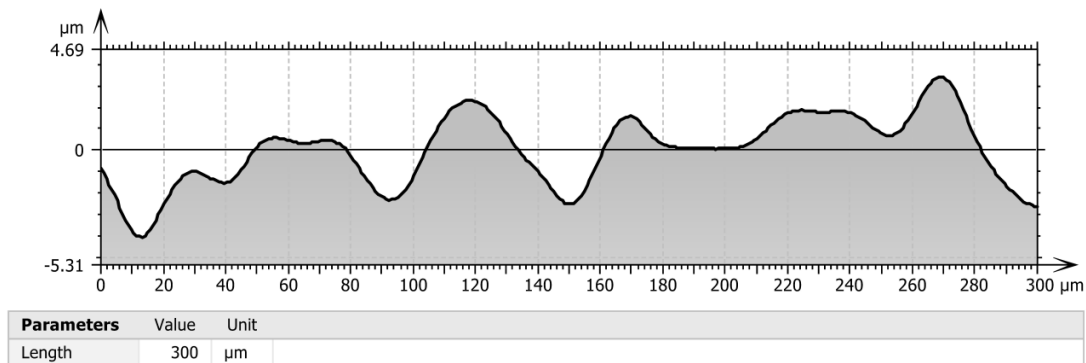


Figure 3.15: Two-dimensional profile cross-section of the first measurement on the flank (diagram captured via MountainsMap Universal).

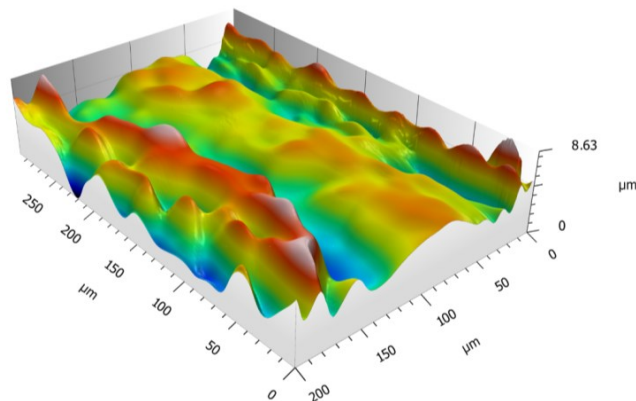
The surface structure in Fig. 3.14 is homogeneous, with peaks and grooves distributed stochastically. Isolated peaks with a significant increase can be identified on the z-axis. The extracted area in Fig. 3.15 shows almost evenly distributed indentations. Deposition of vapor and gaseous fluids in these is possible to form potential nucleation sites. The measured values of the roughness measurements carried out in the valley are documented in Table 3.7.

For this purpose, three measurements are carried out and from these the corresponding roughness parameters according to DIN EN ISO 4827 [11] are reported below:

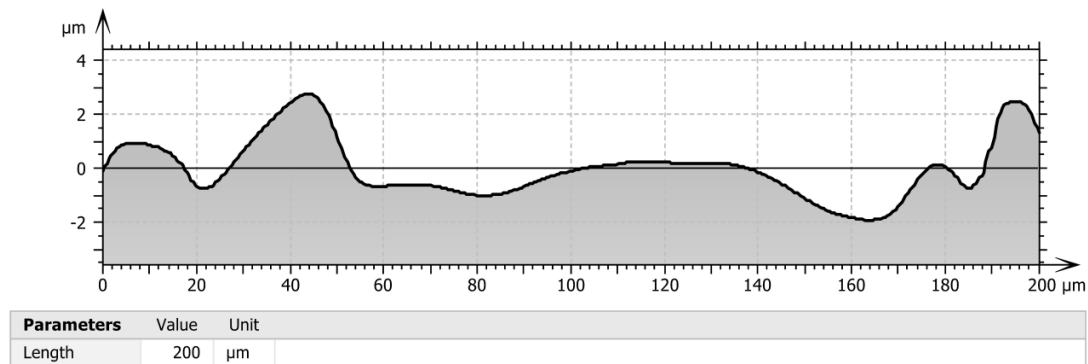
*Table 3.7: Roughness data evaluated according to DIN EN ISO 4287 [11] for the finned tube, measuring point positioned in the fin valley.*

	<b>P<sub>a</sub></b> [μm]	<b>P<sub>q</sub></b> [μm]	<b>P<sub>p</sub></b> [μm]	<b>P<sub>t</sub></b> [μm]	<b>P<sub>pm</sub></b> [μm]	<b>Number of measurements</b>
<b>Mean</b>	0.68	0.81	1.59	3.28	1.59	1371 measurement runs measured at 3 positions
<b>Max</b>	1.66	1.77	3.94	6.83	3.94	
<b>Min</b>	0.20	0.25	0.50	1.15	0.50	
<b>Standard deviation</b>	0.31	0.36	0.69	1.39	0.69	

To determine the roughness parameters, 1371 measurement runs were carried out, which were measured at three positions. The values of these measurements are combined in order to then calculate the mean value, extreme points and the standard deviation  $\sigma$ . The arithmetic mean roughness value  $P_a$  is 0.68 μm, taken from Table 3.7. The square mean roughness value  $P_q$  has a value of 0.81 μm and is increased by approx. 13% compared to  $P_a$ . Fig. 3.16 and Fig. 3.17 show the surface structure and two-dimensional profile cross sectional area of the first measurement in the rib valley.



*Figure 3.16: Surface topography of the first measurement in the rib valley (image captured via MountainsMap Universal).*



*Figure 3.17: Two-dimensional profile cross-section of the first measurement in the rib valley (diagram captured via MountainsMap Universal).*

The surface structure shows a stochastic distribution of peaks and grooves for a homogeneous surface and the various depressions present of different sizes as seen previously can be seen as potential nucleation sites.



#### 4. THE EXPERIMENTAL PLANT AND TEST SUBSTANCES

The heat transfer measurements investigated in this work are carried out on a standard boiling apparatus based on the proposal by Gorenflo (1982 [22] and 1987 [23]), mainly consisting of an evaporator and a condenser. The condenser is mounted above the evaporator, so that a gravity circulation is realized. This eliminates the need of a pump and the fluid, thanks to the principle of natural convection, can flow through the circuit. The electrically heating test tube is installed horizontally inside the evaporator, on the surface of which the test substance evaporates. The vapor flows through a riser into the condenser (first loop) and is liquefied there. The liquid then flows back into the evaporator via a downpipe (second loop). In order to reduce heat losses through heat transfer to the environment, the entire apparatus is located in a climate cell.

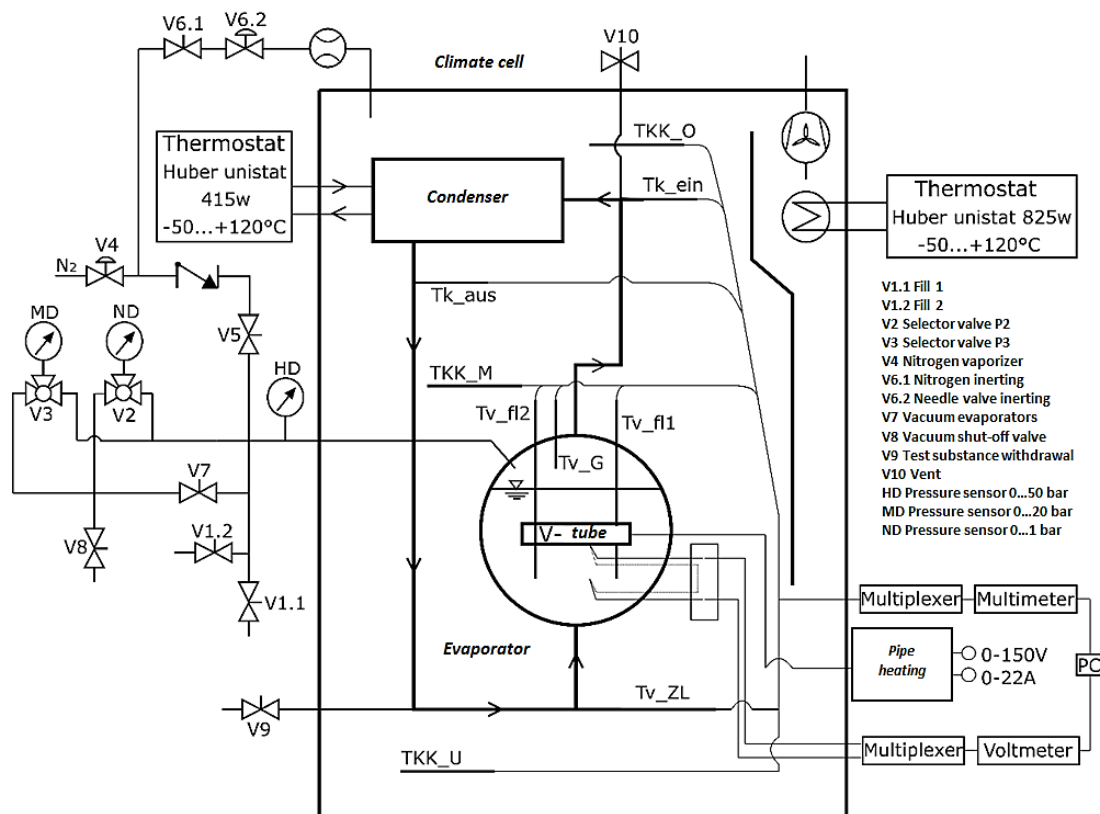


Figure 4.1: Schematic representation of the test facility for the heat transfer measurements [6].

## **4.1 Test facilities**

### **4.1.1 Climate cell**

The test substance circuit can be loaded with an operating pressure up to 40 bar. The entire test substance circuit is located in a climate cell which is thermally insulated from the environment. It consists of metal sheets, which are connected with struts, and it is tempered with the help of a tube bundle heat exchanger in combination with the heat transfer oil ("Therminol D12") that limit the maximum allowed temperature of the air-conditioning cell to 150 °C . The desired cell temperature is set on the "unistat 825w" thermostat from Huber and regulated as a function of the measured cell temperature. Having a different density compared to the rest of the chamber, the hot air tends to go up and the cold air goes down, in this way an adiabatic state is reached, and a constant boiling state is thus made possible. The possible lower operating temperature of -50°C is determined by the "unistat 415w" thermostat connected for the re-cooling of the condenser. In order to exclude environmental influences as far as possible, the air inside the climate cell is circulated by a fan. The climate chamber is made inert with nitrogen through a line located on the top left of the rear wall, transporting nitrogen into the cell. The so-called inerting of the cell with nitrogen is particularly important for two reasons. First of all, the nitrogen prevents, during the measurement, in very low temperature ranges, the formation of condensate or ice on walls and sight glasses. On the other hand, during measurements with highly flammable substances, prevent the penetration of oxygen in the experimental material cycle avoiding in this way the formation of a flammable mixture.

### **4.1.2 Evaporator**

The evaporator installed in the standard boiling apparatus has a total capacity of 2.9 liters, is made of corrosion-resistant stainless-steel and measures 200 x 200 x 180 mm. The test (boiling) surface is placed in the middle of the boiler so that the boiling mechanism can be easily visualized through the glass windows. Sight glasses made of borosilicate are embedded on the front and back and these holds are designed for pressures of up to 40 bar. To document the boiling process, the interior of the

evaporator is illuminated with a cold light source to ensure that the boiling process can be observed using a high-speed camera on the front sight glass. If this is not required, it is replaced with an insulating cover sealed to prevent heat transfer to the environment. The heat pipe is inserted into the evaporator from left to right, so that the face of the pipe from thermocouple in the eighth position to thermocouple in the eleventh position can be observed in the sight glass.

#### **4.1.3 Condenser**

The condenser located above the evaporator consists of a tube bundle heat exchanger surrounded by stainless steel tubes. The heat exchanger consists of fourteen ribbed copper pipes for improving heat transfer and it is connected to the "Unistat 415w" thermostat from Huber and has "Therminol D12" heat transfer oil flowing through it. In this way, the heat supplied via the test tube is dissipated in the condenser and transferred to the thermal oil.

#### **4.1.4 Test tubes**

Three different test tubes are used in this work: two smooth tubes one in copper (R27) and one in stainless-steel (R30) and one stainless-steel finned tube (R29). These pipes are characterized by a coaxial structure: the internal part of the tubes has a diameter equal to 9.5 mm and it is made with a copper tube surrounded by a conducting wire equally for all the tubes. This conductive part can be electrically heated being connected to a DC power source thus making it possible for the substance surrounding it to evaporate on the surface.

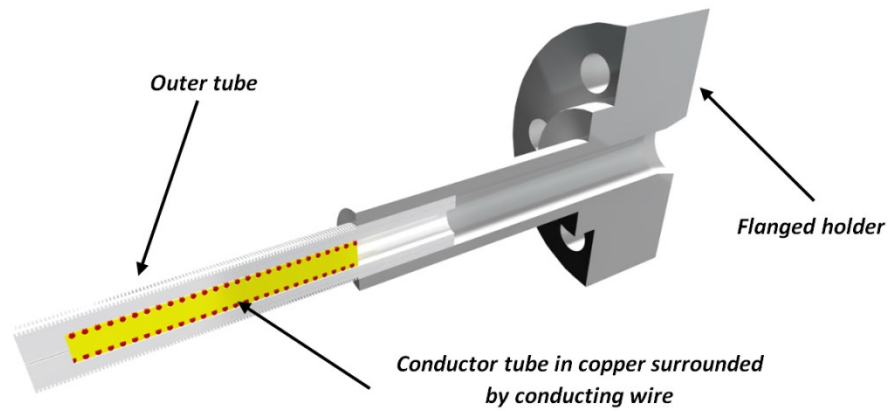


Figure 4.2: Schematic representation of the test tube.

All the tubes have a total length of about 125 mm with a core diameter of 19.05 mm. The heating length, from which we are going to calculate the heating area for the calculation of the heat flux, is equal 80 mm ( $125-35-10=80$  mm), as it is possible to note from Fig 4.3 (a) and 4.3 (b).

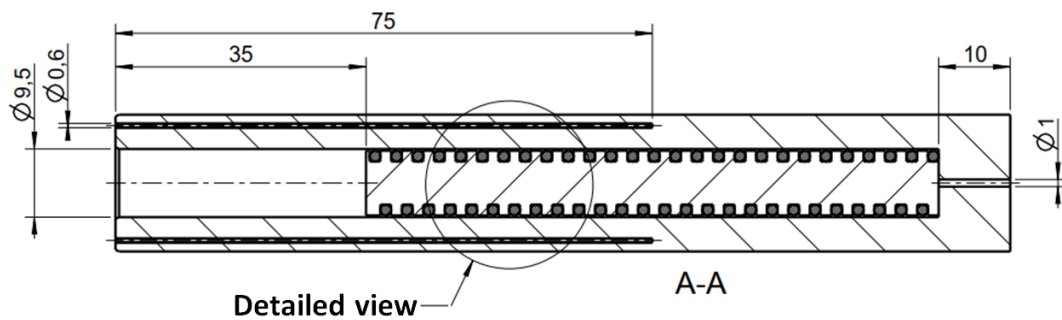


Figure 4.3 (a): Frontal section of the smooth tube.

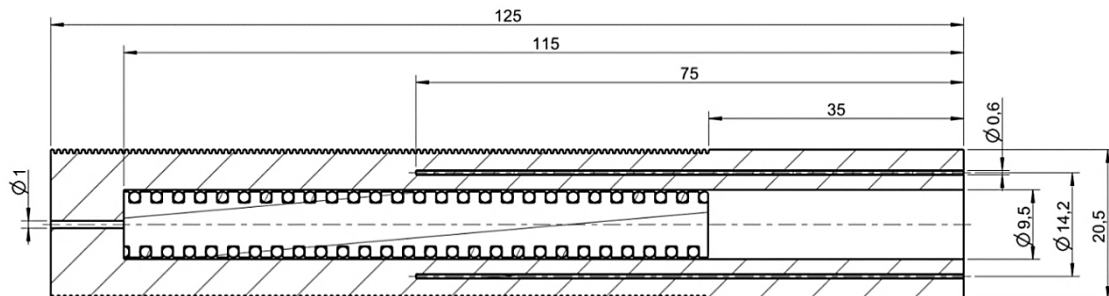


Figure 4.3 (b): Frontal section of the finned tube.



Regarding the finned tube, the geometrical data of the structure are described below in Table 4.1 and for the sake of clarity they are illustrated in Fig. 4.4.

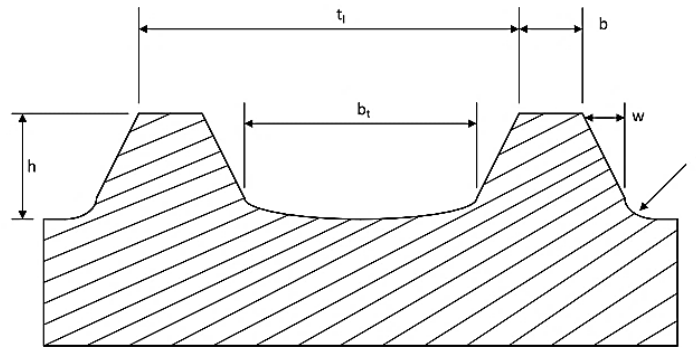


Figure 4.4: Representation of an example rib geometry [7].

Table 4.1 shows that the fin height is equal to 0.51 mm, so since the fins run around all the circumference of the pipe, this value has to be doubled for evaluating the outer diameter. Adding, in this way 1 mm to the core diameter of 19.05 mm it is possible to obtain an outer diameter equal to 20.05 mm for the finned tube.

Table 4.1: Geometrical data of the rib structure.

fin height $h$	0.51 mm
fin width $b$	0.35 mm
clear fin spacing $t_l$	0.84 mm
radius at the base $r_b$	0.25 mm
fin pitch $b_t$	0.4 mm
distance between base and fin tip $w$	0.04 mm
area increase $\varphi$	1.4884

For a defined pressure and a certain temperature (in saturation condition), the heat transfer coefficient  $\alpha$  is determined. For this purpose, the heat flux  $\dot{q}$  and the overheating  $\Delta T$  must be measured, as can be seen from Equations 2.1 to 2.3 in chapter 2. The reference heat transfer area  $A$  in equation 2.1 is calculated from the known

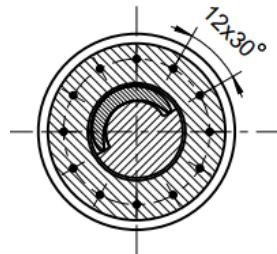
dimensions of the pipe (the pipe diameter and the pipe length). In this way the heat flow, equal to the electrical power, could be calculated as the product of the directly measured heating voltage  $U$  and the heating current  $I$ :

$$\dot{Q} = P = UI - R_0 I^2 \quad (4.1)$$

As it is possible to see from equation 4.1 (reported above) to calculate a value that is as exact as possible, the cable resistance  $R_0$  must be subtracted, so that the cable loss is not neglected. So, knowing the heat transfer area from the geometry of the tube, the heat flux is equal to:

$$\dot{q} = \frac{P}{l \cdot d \cdot \pi \cdot 10^{-6}} \quad (4.2)$$

It is necessary to multiply for  $10^{-6}$  because all our measurements related to the dimensions of the tube are in *mm*.



*Figure 4.5: Placement of the thermocouples around the pipe circumference [6].*

Twelve coaxial grooves with a diameter of 0.6 mm and a length of 75 mm are embedded in a diameter of 14.2 mm, in which the thermocouples (type K with a working range of 0 to 1100°C) are soldered. For better understanding, the positions of the thermocouples are also shown above in Fig. 4.5. The electrical power of the heating surface is controlled by a manually operated voltage converter and measured by a power transducer. So, setting the heat flow  $\dot{Q}$  and determining the temperature difference  $\Delta T$  is possible to evaluate the heat transfer coefficient from the following equation:

$$\alpha = \frac{\dot{Q}}{\Delta T} = \frac{\dot{q}}{A \cdot (T_w - T_{sat})} \quad (4.3)$$

#### 4.1.5 Pipe wall correction

The thermocouples are installed inside the test tubes in a thermocouple carrier, which is below the surface. A direct measurement of the wall temperature  $T_w$  is not possible because the thermocouples would be attached directly to the surface, and this would influence the heat transfer. This difference is due to the fact that the holes are covered with different materials and therefore different thermal conductivities. The different layers and the position of the thermocouples are shown in Fig. 4.6. The thermocouples are positioned with an angle of  $30^\circ$  from each other over the circumference to prevent overheating of the test material. The correction factor takes into account the difference between the temperature measured by the thermocouples and the temperature of the outer diameter of the test tubes. It is possible to define the correction factor as:

$$\Delta T_{corr} = \dot{q} K_{corr} \quad (4.4)$$

Assuming that the heat transfer is developed only radially, this correction factor exclusively assumes radial heat conduction from the heat conductor (carrier) to the outer tube surface:

$$\Delta T_{corr} = \dot{q} K_{tube} \quad (4.5)$$

where  $K_{tube}$  is calculated as:

$$K_{tube} = \frac{1}{2} \cdot d_{outer} \cdot \sum_i \frac{1}{\lambda_i} \cdot \ln \left( \frac{d_{outer,i}}{d_{inner,i}} \right) \quad (4.6)$$

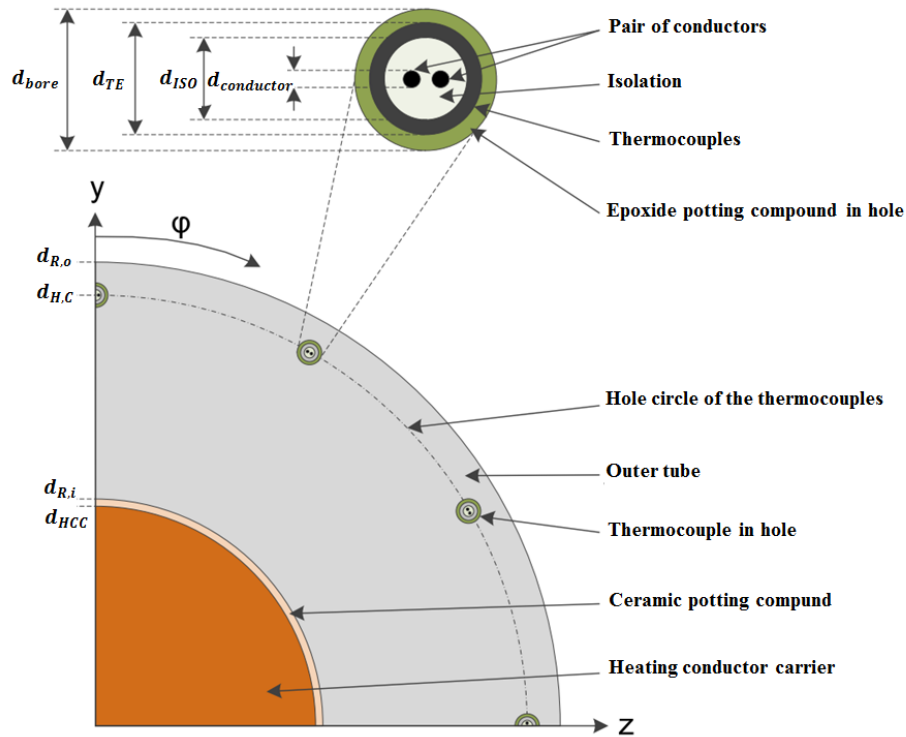


Figure 4.6: Schematic representation of the materials used [7].

In addition to the tube wall, the thermal conductivity of the thermally conductive paste, the magnesium oxide and Inconel are taken into account for the calculation, as these surround the thermocouples. According to equation below, the correction factor is subtracted from the measured value  $\Delta T_{meas}$  for evaluating the real temperature interval between the wall and the fluid that is going to be used in the following calculation related to the heat transfer coefficient  $\alpha$ :

$$\Delta T = \Delta T_{meas} - \Delta T_{corr} \quad (4.7)$$

Tube wall superheat is formed by averaging all twelve local temperature differences. During the experiment, it is observed that there may be defective thermocouples in the test tube or defected reference thermocouples in the fluid. So, in order to maintain the weighting in the averaging, missing temperature differences are subsequently replaced. For this purpose, it is assumed that the heat transfer at the test tube is symmetrical along the test tube  $\varphi=0^\circ$  (see chapter 5.3).

## **4.2 Thermostats**

The temperature of the cell is controlled with the help of the thermostat "unistat 825w" and the temperature of the secondary fluid while for rejecting the heat inside the condenser, by the thermostat "unistat 415w" from the company "Huber". A temperature sensor (Pt100) is connected to the unistat 825w model, which measure the temperature inside the cell. So, in this way, in the so-called process regulation it is possible to control the internal temperature of the thermostat. In this case, the setpoint temperature does not correspond to the process temperature, but to the internal temperature in the thermostat. The same happens for the thermostat that controls the temperature of the condenser and both thermostats are connected to the measuring computer with the "SpyControl" software.

## **4.3 Measuring device**

In this paragraph, the measurement technology (temperature sensors, pressure sensors and activity recording) used in this analysis, is explained in detail. In addition, the required safety technology is briefly discussed as the measurement program used.

### **4.3.1 Temperature measurement technology**

It is necessary that in our apparatus the temperature is always the same and equal to the saturation temperature. As it is possible to observe in Fig. 4.1 there are three temperature sensors located one in the bottom, one in the middle, one in the upper part, to be sure of having a homogeneous temperature inside the chamber (TKK\_O, TKK\_M, TKK\_U). Inside the evaporator are located three temperature sensors (two for the temperature of the liquid and one for the temperature of the gas). During the process these three temperatures have to be the same and equal to the saturation temperature and to TK\_ein (see Fig. 4.1). There are also other two temperature sensors for the temperature at the outlet of the condenser (Tk\_aus) and the temperature at the inlet of the evaporator that have to be the same (Tv\_ZL).

### 4.3.2 Resistance thermometer

The temperatures in the cell and in the test circuit are measured with Pt100 resistance thermometers. Inside these devices the platinum has a positive temperature coefficient, so the electrical resistance of the platinum increases with increasing temperature. The advantages of these sensors are their small dimensions, one short response time and a closed structure. The measuring resistor attached to the sensor tip is very low constant current. This leads to the following equation:

$$P = R \cdot I^2 \quad (4.8)$$

The power loss at the measuring resistor causes self-heating of the resistance (Joule effect). The associated increase in the resistance value falsifies the measurement result. Manufacturer of platinum resistance sensors usually give a maximum value of 1 mA for the measuring current, since with this value it is possible to have negligible self-heating. The voltage drops resulting from the applied current is measured using this equation:

$$U = R \cdot I \quad (4.9)$$

Where U is the voltage, R the resistance and I the applied measuring current. The sensors will be connected via a line to a multimeter, which converts the analog into the digital signal and transmits it to the PC. To be as precise as possible, the cable resistances must be considered:

$$R_l = \rho \frac{l}{A} \quad (4.10)$$

The line resistance is calculated with the ratio between the specific line resistance  $\rho$  multiply by the length  $l$  and the cross-section  $A$  of the cable.

### 4.3.3 Thermocouples

The temperature difference  $\Delta T$  between the surface of the test tube and the surrounding liquid is measured with thermocouples. These are suitable due to its compact design and, so for the installation inside the pipe. The basis of measurement with thermocouples is the thermoelectric effect. The temperature gradient within an electrical conductor creates an electromotive force, which is proportional to the temperature

gradient. This force causes a flow of electrons inside the conductor and the magnitude, and the direction of this force depend on the temperature gradient and on the material of the conductor. The tensions between the two free terminals of the conductor results in a voltage difference. It is therefore possible to measure the desired temperature difference  $\Delta T$ , without knowing the absolute temperatures of the two ends.

#### **4.3.4 Pressure measurement technology**

The pressure measurement is necessary for the evaluation of the pressure inside the evaporator because this pressure corresponds to the saturation pressure of the liquid that is considered. In the upper part of the evaporator is present a capillary pipe because the pressure sensors have to stay outside the chamber. There are three pressure sensors for different ranges of pressure:

- 0 – 1 *bar*
- 1 – 16 *bar*
- 16 – 50 *bar*

In the case considered, the second range is used for the n-pentane hydrocarbon (being characterized by higher pressures) and the pressure sensor relative to the first range is used for the two alcohols (having lower pressures).

#### **4.3.5 Safety device**

To avoid damages, if dangerous substances such as propane are used (which is a highly flammable refrigerant), the system is equipped with a pipe which constantly introduces nitrogen particles into the chamber, passing through valve V4 (see Fig. 4.1). In this way, in the event of a propane leak, from the evaporator or condenser, it would bind with the nitrogen present inside the chamber (V6.1 and V6.2 and flow rate sensor). An additional safety device is present within the system. It consists of a gas alarm system, that with the presence of air inside the chamber, blocks any heating system and all the valves (even if in the system used there are all manually adjustable valves). Observing another time Fig. 4.1, through valve V8 is possible to make vacuum inside the plant, so when the valve V2 is closed is also possible to create a vacuum in the piece of pipe between

V2 and V8. Through valve V9, being in the bottom part of the chamber is possible to take away some samples of the substances. In case of emergency in the test area is also present an emergency bottom, when the superheating goes above the 80 K, it is necessary to cut the electricity from the pipe.

#### 4.3.6 Measuring program

The measurement program is set in the LabView development environment. It enables the conversion, visualization and storage of measured values. In the main interface of the program is possible to watch and so to control the trend of the current values, of the heat flux  $\dot{q}$ , of the heat transfer coefficients  $\alpha$  and of the reduced pressure  $p^*$ , while in the lower graph is reported the absolute pressure  $p_{sat}$ . In addition, the mean deviation of the reduced pressure from its setpoint and also the measured data of the platinum temperature sensors are visualized.

### 4.4 Preparation and performance of the measurements

#### 4.4.1 Starting the measurement

The heat transfer measurements take place on the test tubes described varying the test materials. The influence of the surface quality and the influence of the substance can thus be examined and evaluated. In order to achieve the highest possible reproducibility of the measurements and to be able to make an exact statement, several series of measurements are carried out. In the following tables (Table 4.1, Table 4.2) the series of measurements for the smooth and finned tube are shown.

Table 4.2: Hydrocarbons to be examined.

Normalized pressure $p^* = p_{sat} / p_{crit}$	n-pentane	
	$p_{sat}$ [bar]	$T_{sat}$ [°C]
0.1	3.37	76.56
0.05	1.69	51.84
0.03	1.01	36.00

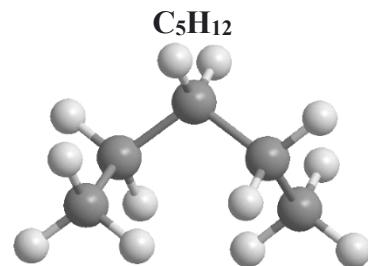
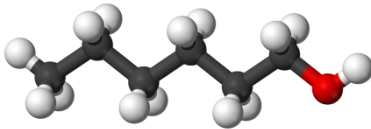
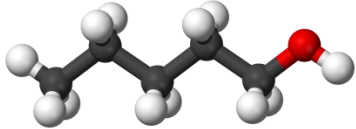




Table 4.3: Alcohols to be examined.

Normalized pressure $p^* = p_{\text{sat}} / p_{\text{crit}}$	1-hexanol		1-pentanol	
	$p_{\text{sat}}$ [bar]	$T_{\text{sat}}$ [°C]	$p_{\text{sat}}$ [bar]	$T_{\text{sat}}$ [°C]
0.01	0.36	126.51	0.37	110.99
0.007	0.25	117.68	0.25	102.16
	$C_6H_{14}O$		$C_5H_{12}O$	
				

The test procedure can be divided into different steps, which are described in more detail below:

a) Cleaning and installation:

The first step is to clean the test tubes with isopropanol before installing them in the boiling apparatus. In this way particles and dust, as well as other impurities such as fats and oils, are removed. After flushing with isopropanol, the surface is dried using a hot air gun. As soon as this step is done, the test tube is installed parallel to the evaporator. The cover of the evaporator is also provided with a specially tailored PTFE (polytetrafluoroethylene) seal to prevent leaks and the test substance from escaping.

b) Pressure test:

A pressure test is required to identify further leakage points. For this purpose, forming gas (a mixture of up to 10% hydrogen and nitrogen) is filled into the test circuit and then increased to a pressure of 40 bar. Leaks can then be detected using a suitable leak detector, as this emits an acoustic signal when such a leak is identified. A 14-hour pressure test is then carried out. The pressure in the test circuit depends on the ambient temperature, so the temperature of the climate cell is set to a constant value. A pressure loss of less than 15 mbar after the duration described above can be approved, and then the filling with the desired test substance follows.

c) Filling process:

A vacuum pump is required to fill the system. This is used for evacuation and thus for the removal of foreign matter and the ambient air from the test facility. The storage container with the corresponding test substance is connected via a needle valve so that it flows through a capillary into the condenser and condenses there. The evaporator is filled via the supply lines described in chapter 3. The filling process is continued until the fill level can just be seen in the sight glass.

d) Hermit process:

The temperatures of the climate cell and the condenser are adjusted to the highest possible saturation temperatures of the test substance without exceeding the maximum temperature of the system. The heat flow density  $\dot{q}$  of the test tube is regulated to  $100 \text{ kW/m}^2$ . The degassing valve on the top of the system is then briefly opened several times to allow the low-boiling components (possible impurities) to be removed.

#### **4.4.2 Recording of the measuring points**

First of all, the test facility is regulated to the desired boiling temperature, which is a function of the desired reduced pressure  $p^*$  to be measured. This state is reached as soon as the reduced pressure shows a maximum deviation of  $\pm 0.05\%$  from the setpoint after approx. 20 minutes. The values to be set for the various test substances can be found in the database in VDI-Atlas-2013 [24]. At the beginning, two initial value measurements are taken, the so-called “zero values”. The first measuring point is recorded after about ten minutes, the second point after another ten minutes. These are used to document the voltage difference between the thermocouples and their comparison points. The electrical pipe heating is then switched on and increased in small steps up to a heat flow density equal to  $100 \text{ kW/m}^2$ . For the first law of thermodynamic the heat that enters inside the evaporator has to be rejected by the condenser.

So, the thermal power absorbed by the evaporator has to be the same of the thermal power rejected by the condenser:

$$\dot{Q}_{evap} = \dot{Q}_{cond} \quad (4.11)$$

To keep the pressure in the evaporator constant, as this increases with the heat temperature supplied via the pipe, the thermostat connected to the condenser is used in correlation of this. It must be ensured that the maximum permissible temperatures for the various pipe materials are not exceeded, as this will lead to the test pipe being destroyed. If the maximum deviation of  $\pm 0.05\%$  is exceeded, the condenser temperature must be controlled. If the pressure deviation is  $\geq 0.05\%$ , the temperature of the secondary fluid in the condenser is lowered. In this way, an increase of the heat flow in the condenser occurs, the temperature of the inflowing liquid in the evaporator drops and it results in a pressure reduction. As soon as the maximum  $0.05\%$  is undershot, the condenser temperature must be increased accordingly. To avoid the hysteresis effects, a high heat flow density equal to  $100 \text{ kW/m}^2\text{K}$  is started and gradually reduced. This is based on the premise that all nucleation sites should be activated. If the nucleation site activation is not complete, the heat transfer coefficients show smaller and therefore incorrect values, which falsify the measurement results. If a stationary course is recognizable after a waiting time of 20 minutes, the measuring point is recorded. Immediately afterwards, for each heat flow density, the test tube surface is documented with the digital single-lens reflex camera "Nikon D800E". For this purpose, the cold light source inside the climate cell is switched on to ensure sufficient exposure. The last measurement point is recorded for a heat flux of  $50 \text{ W/m}^2$  and then the heating pipe is switched off.



## 5. TEST EVALUATION

In this chapter, the results of the measurement carried out on the standard boiling apparatus are presented, discussed and compared with the values from the literature. The required heat transfer coefficient  $\alpha$  between the test material and the tubular heating surface is calculated using the equation 2.3. The current and the voltage are measured at the test tube and the heat flux is calculated using the equation 4.3 by relating these values to the heating surface of the tube. The evaluated heat transfer coefficients of all measurement series for the test materials n-pentane, 1-hexanol and 1-pentanol are stored in the Appendix (chapter 8).

### 5.1 Measurement results on smooth stainless-steel and copper tubes

The following diagram in Fig. 5.1 shows the data for the heat transfer coefficients investigated experimentally for the hydrocarbon n-pentane with the fine sandblasted smooth stainless-steel and copper tubes. The heat transfer coefficient  $\alpha$  is shown as a double logarithmic function of the heat flow density  $\dot{q}$ .

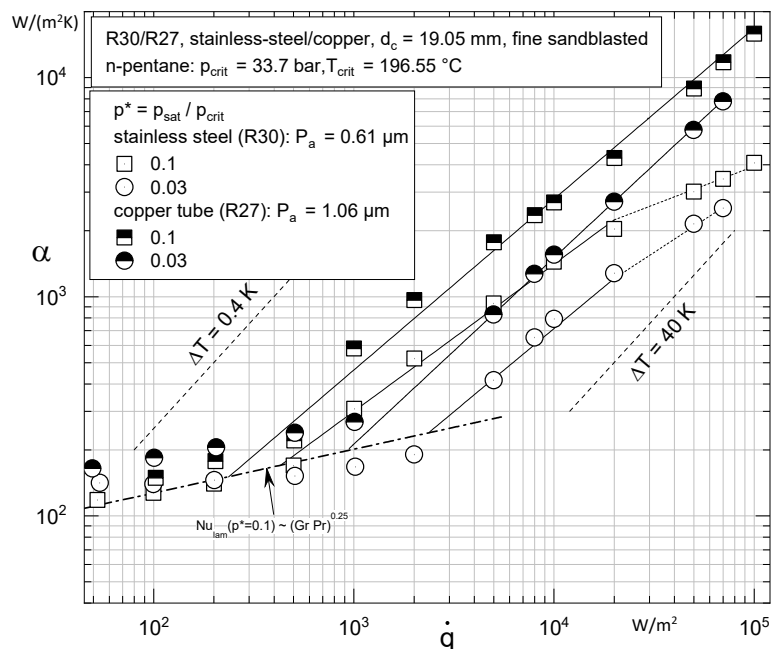


Figure 5.1: Heat transfer coefficient as a function of the heat flow density for the smooth stainless-steel and copper tubes on the test substance n-pentane under pressure variation (graph created using Origin 2016).

To avoid overlapping of multiple lines and for a greater understanding of the graph, in the Fig. 5.1 only the values for the highest reduced pressures  $p^*$  equal to 0.1 and the lowest one equal to 0.03 have been represented, while the values referring to the reduced pressure 0.05 are reported in the Appendix. Observing the trend of these values, it is possible to note that in the zone of natural convection, in which, as shown in equations 2.4 and 2.5 there is a strong dependence on the properties of the fluid, on the geometry and not a significant influence on the heat transfer coefficient of the heat flow, regarding the stainless-steel tube only a slight increase in  $\alpha$  can be observed in the range of heat flux densities from 50 W/m<sup>2</sup> to 2000 W/m<sup>2</sup>. While for the copper tube, the measured values do not agree with the values calculated with the Nusselt correlation, as they, for all the values of the heat flux in the free convection zone, are located in a much higher position, especially for the values referring to the reduced pressure equal to 0.03. On the other hand, in the area of nucleate boiling, it is possible to notice that the correlation 5.1, according to [1], as likewise the correlation demonstrated by Cooper's (1984) [17], is respected:

$$\alpha \sim \dot{q}^n \quad (5.1)$$

To get a clearer view of the trend of the measured values, interpolation lines through all these points are used. In addition to the considerations just stated, it is possible to note an improvement of the heat transfer coefficients due to an increase in pressure. All nucleation sites are activated due to the sufficiently high overheating as it is also explained in [25]. In general, it is possible to have this proportionality:

$$N \sim (T_w - T_{sat})^m \quad (5.2)$$

The measured values in Fig. 5.1, illustrate this by a decreasing distance between the interpolation lines for increasing heat flux densities (especially for the stainless-steel tube). For copper pipe values, as will also be shown for the two alcohols considered, after approximately a height flux value of 20000 W/m<sup>2</sup> instead of having a reduction in slope, the lines don't change their inclination. Therefore, the maximum heat flux  $\dot{q}_{crit}$  in

saturated pool nucleate boiling on horizontal flat plates or plain tubes can be calculated from the correlation by Kutateladze and Zuber [1] et al.:

$$\dot{q}_{crit} = K_1 \Delta h_v \rho_G^{0.5} (\sigma (\rho_L - \rho_G) g)^{0.25} \quad (5.3)$$

Where  $\Delta h_v$  is the enthalpy of vaporization,  $\sigma$  is the surface tension and  $\rho_G$  and  $\rho_L$  are the densities of the vapor and the liquid respectively.  $K_1$  is a constant whose value depends on the geometry of the heating surface; Zuber derived a numerical value of 0.13 for this constant from a simplified model for the development of instability in the counter flow of liquid and vapor to a horizontal plate. Kutateladze obtained  $K_1=0.13$  to  $K_1=0.16$  by fitting the measured values. Many other correlations exist in literature for the calculation of  $\dot{q}_{crit}$ , most of them contain the terms  $\Delta h_v \rho_G^{0.5}$  and  $(\rho_L - \rho_G)^m$  in which the exponent  $m$  is  $1.25 < m < 1.5$ . Of all the parameters important for  $\dot{q}_{crit}$  the effect of the pressure has been investigated most. From studies by Borishanskij and Mostinskij and the existing experimental data on  $\dot{q}_{crit}$ , the following function can be interpolated for the relative pressure dependence of  $\dot{q}_{crit}$ , which is analogous to the equation for the  $\alpha(p^*)$  relationship:

$$\dot{q}_{crit} / \dot{q}_{crit,0} = 2.8 p^{*0.4} (1 - p^*) \quad (5.4)$$

where  $\dot{q}_{crit,0}$  is the value for the maximum heat flux at the reference pressure  $p_0^* = 0.1$ . The interpolation line of the graph reported below is characterized by two functions similar to one of Borishanskij and Mostinskij seen previously.

$$\dot{q}_{crit} / \dot{q}_{crit,0} = 3.2 p^{*0.45} (1 - p^*)^{1.2} \text{ for } p^* \geq 0.1 \quad (5.5)$$

$$\dot{q}_{crit} / \dot{q}_{crit,0} = 1.2 (p^{*0.17} + p^{*0.8}) \text{ for } p^* \leq 0.1 \quad (5.6)$$

Without measurements related to the critical value the correlation of Noyes is recommended:

$$\dot{q}_{crit} = A_3 \Delta h_v [(\rho_L - \rho_G) \rho_G]^{0.5} [(g\sigma)/\rho_L]^{0.25} Pr^{-0.245} \quad (5.7)$$

Where  $A_3$  is equal to 0.144. Motion of the bubbly mixture that directs liquid toward the heated wall may also increase the maximum heat flux. Factors that modify the maximum heat flux in saturated pool boiling include the roughness of the heated surface, the type of heating, impurities and the wetting of the heated surface. The results of studies on these effects are inconsistent, so they cannot yet be included in correlations. Therefore, all that can be derived from the equations already analyzed is an approximate estimate for the maximum heat flux in saturated pool nucleate boiling. It is therefore only possible to make assumptions based on the behavior observed in the graph in Figures 5.1-5.3, because as analyzed in chapter 2 in more detail, the surface tension also depends on the surface material used, since depending on the material used and its roughness, the contact angle will be different. In addition, we also know that each material has a different Gibbs energy, and this leads to different behavior in relation to the use of different materials. Since all the equations described above were evaluated using mainly copper, to gain a better understanding of how much the material can influence the value of the critical heat flux, a graph was subsequently plotted showing the value of  $\dot{q}_{crit}$  as a function of reduced pressure for the measured values calculated using the equation 5.6 of Noyes, since no critical point measurements were carried out in this work.



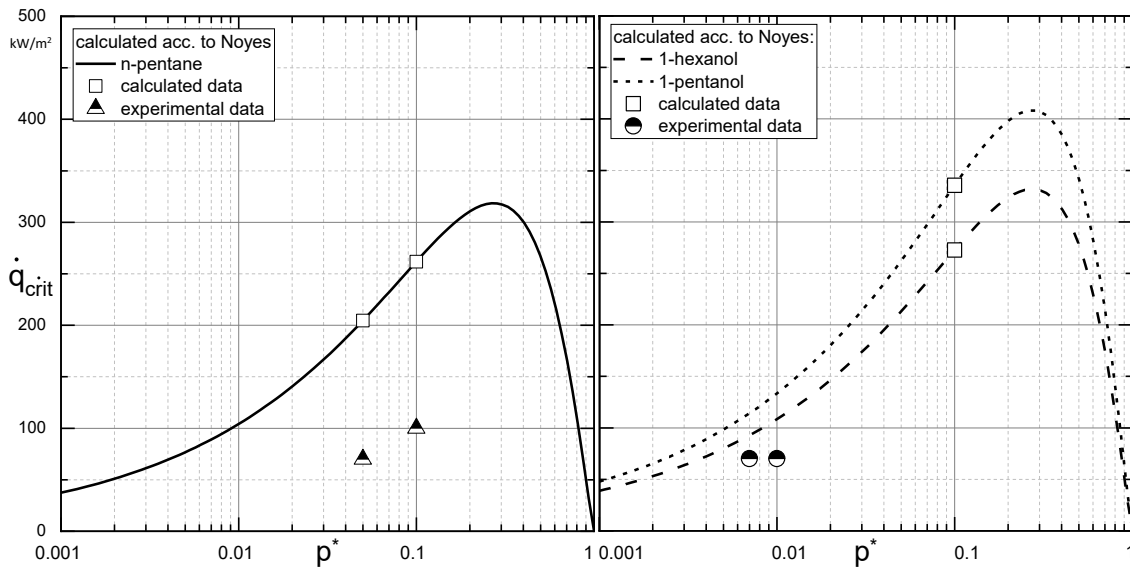


Figure 5.2: Representation of the critical heat flow density  $\dot{q}_{crit}$  depending on the reduced pressure for the test substances *n*-pentane, 1-hexanol and 1-pentanol (graphs created using Origin 2016).

The calculated course of the critical heat flow density in Fig. 5.2 has a maximum at the point  $p^* = 0.3$  and another increase leads to a strong decrease in the critical heat flow density. As it is possible to notice from the figure above, there is a strong material dependency, as the values for stainless-steel are far below those for copper, and thus below the curve for calculated critical heat flux density. In addition, for the alcohols it is possible to observe that for a reduced pressure of  $p^*=0.007$ , the distance between the calculated data and the experimental values is less than for a reduced pressure  $p^*=0.01$ . A physical motivation can also be given as a reason for the trend of interpolation lines. Since copper has a higher thermal conductivity than stainless-steel, it will have a lower surface temperature, as the heat from the heating tube will be better transferred to the liquid, whereas with the stainless-steel tube will be more difficult to transfer heat, resulting in a higher surface temperature. Thus, as we will see in paragraph 5.3, the copper tube will result in less overheating than the stainless-steel tube. In addition, the start of nucleate boiling (ONB) is shifted to lower heat flux densities specially for low pressures and for having a more clarity of the range in which the ONB point is located it is possible to use high speed recordings found with more details in the Appendix

(chapter 8). Looking at measured values for the copper tube, it can be confirmed that this point for a reduced pressure equal to 0.1 will be found around 500-1000 W/m<sup>2</sup>, while for a reduced pressure of 0.03 it appears to be more shifted towards 1000 W/m<sup>2</sup>, ranges confirmed by Table 8.15. The same consideration can be made for the stainless-steel pipe because from the diagram it is possible to see that the point of onset of nucleation site at 0.1 is before 500 W/m<sup>2</sup> and for the reduced pressure of 0.03, as was in the case with the copper pipe, we will have higher values and from the images in Appendix Tab. 8.12 it is possible to find it around 2000 W/m<sup>2</sup>. A similar behavior can be observed by going with the two alcohols considered in this analysis (1-hexanol and 1-pentanol), reported in Fig. 5.3, where also in this case the scaling is double-logarithmic in both axis and the measured values of both substances are shown at the reduced pressures  $p^* = 0.01$  and 0.007. Observing Fig. 5.3, the same trend can be observed as for n-pentane. As lower reduced pressures have been considered, the lines referring to the largest and smallest pressure are less distant from each other.

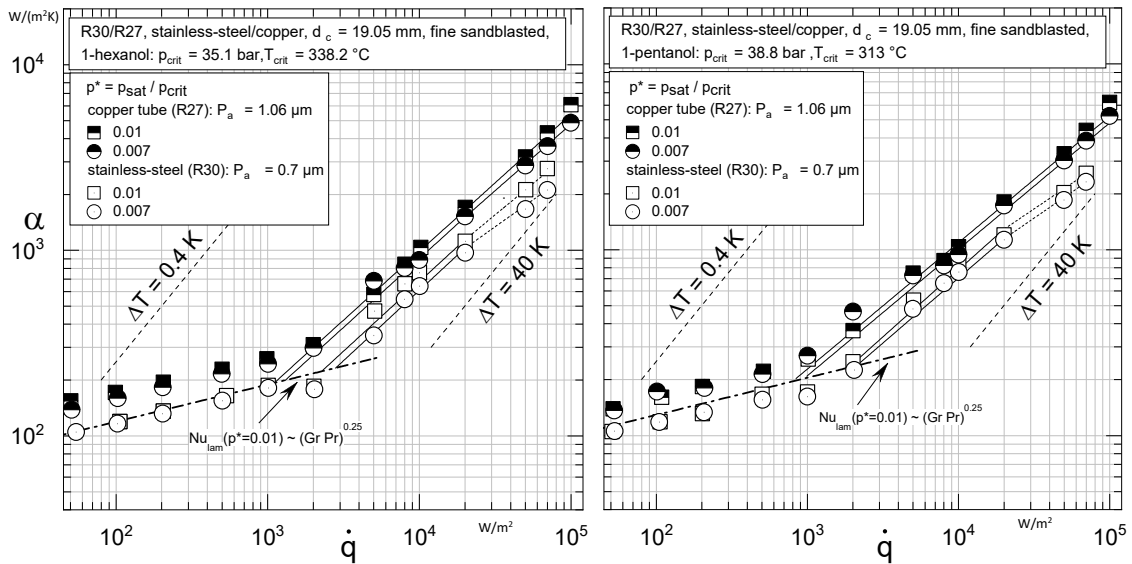


Figure 5.3: Heat transfer coefficient as a function of the heat flow density for the smooth stainless-steel and copper tube on the test substances 1-hexanol (left side) and 1-pentanol (right side) under pressure variation (graph created using Origin 2016).

Also in this case, from the graphs it is difficult to determine a precise value of the onset of nucleate boiling, but as a confirmation of the range in which it can be found, it is possible to use the high speed recordings in which can be noted that for the copper tube

and the substance 1-hexanol at a pressure equal to 0.01, at a heat flux value equal to 2000 W/m<sup>2</sup> no bubbles are present, while for a heat flux equal to 5000 W/m<sup>2</sup> the point at issue has already been passed and this goes to prove what is observed in Fig. 5.3. While for the reduced pressure equal to 0.007 the point is closer to 5000 W/m<sup>2</sup> and for both the reduced pressure analyzed the stainless-steel pipe present more or less the same ranges. Regarding the graph referring to 1-pentanol it can be made evident that from the  $\alpha - \dot{q}$  graph it is possible to see that the onset of nucleate boiling, for the same reduced pressure equal to 0.01, would seem to be earlier than in the case of 1-hexanol and this as will be seen in the next paragraph will be confirmed in the case of the finned tube. This behavior is justified by the saturation curves shown in the figure below.

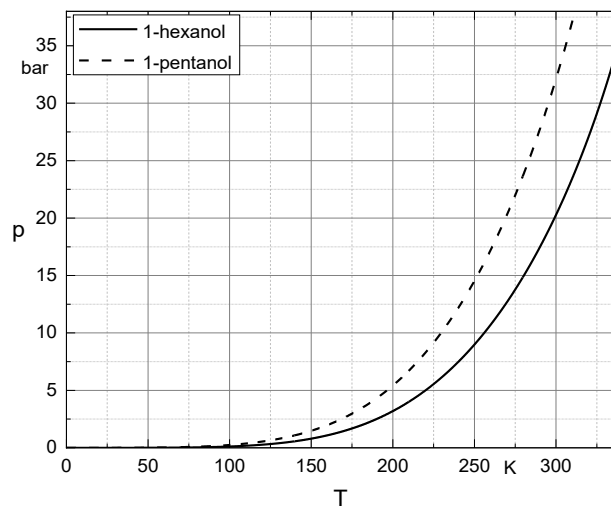


Figure 5.4: Comparison of the saturation curve of alcohol 1-hexanol and alcohol 1-pentanol (graph created using Origin 2016).

As can be seen in Fig. 5.4, the saturation curve referred to 1-pentanol is shifted to the left in relation to the 1-hexanol curve. Therefore, if we imagine a horizontal line, with constant pressure, it will intersect first the curve referring to 1-pentanol and consequently it will evaporate before. Regarding the alcohol 1-pentanol and a reduced pressure equal to 0.01, it will most likely be in the range between 1000 and 2000 W/m<sup>2</sup>, while for the reduced pressure equal to 0.007 it appears to be shifted towards greater heat fluxes in a range between 2000 and 5000 W/m<sup>2</sup> and more or less the same for the stainless-steel pipe. The heat transfer coefficient of both the alcohols considered

increases as pressure grows and with the increasing of the heat flow density. For an increase in pressure, the tube wall overheating  $\Delta T$  required to activate the nucleation sites decreases, which results in a decrease in the critical bubble radius as demonstrated in the equation 2.21. More nucleation sites are activated,  $\alpha$  increases. For a sufficiently high heat flux density, the pressure dependence is negligible, the overheating is large enough and all nucleation sites are already activated. In the range of the heat flow density from 50 W/m<sup>2</sup> to 2000 W/m<sup>2</sup>, the measurement results of both substances are slightly below the Nusselt correlation. In this section, there is a little or no pressure dependence and there is no formation of bubbles, the heat transfer coefficient shows only a slight increase. As was observed for n-pentane for high values of the reduced pressure, we have a reduction in the slope of the interpolation curves. This is due also to the fact that when I have an increase of the reduced pressure it is obtained at the same time a decrease in the specific vaporization enthalpy, as can be observed by means of Fig. 5.5. From the Clausius Clapeyron equation (2.17) shown in chapter 2.2, it can be seen that when there is a low value of  $\Delta h_v$  for high reduced pressures, there is at the same time a slope  $dp/dT$  descent.

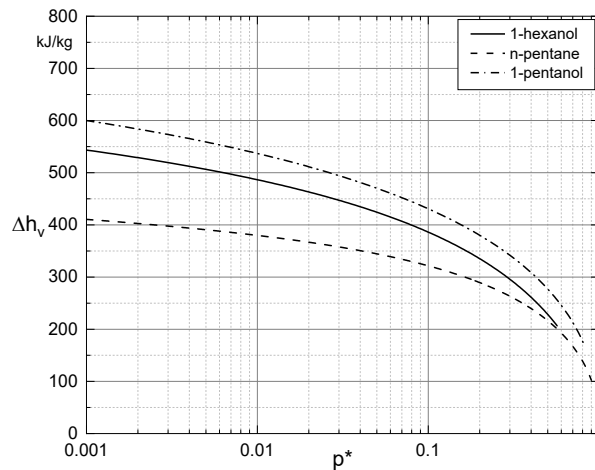


Figure 5.5:  $\Delta h_v - p^*$  diagram referred to the three substances analyzed: 1-hexanol, n-pentane and 1-pentanol (graph created using Origin 2016)

For justifying this behavior, another physical reason can be given because at higher reduced pressure for the bubble formation a lower tube wall overheating  $\Delta T$  is required, since most of the nucleate sites have been activated. Furthermore, it is possible to

evaluate from the equation 2.21 that the critical radius necessary for bubble survivability decreases, so smaller bubbles are activated (as shown in the figure below on the left side) and an improvement in heat transfer is achieved. On the right side of the Fig. 5.6, it is possible to notice in the  $\sigma - p^*$  diagram in which the surface tension decreases with the increasing of the reduced pressure, and this goes to confirm that for higher values of  $p^*$  a lower critical radius is obtained. This appears reasonable as wetting depends on surface tension. As well known the well wetting liquids have a small surface tension and consequently a small critical radius. In the same equation it is possible to notice at denominator the difference in density between the liquid and the gas phase and this underscores the behavior analyzed so far, because as the reduced pressure increases this difference in density grows. For lower pressures there is a higher enthalpy difference, a lower specific volume difference and so a lower density difference with a higher surface tension and contact angle and thus a higher diameter  $d_B$ .

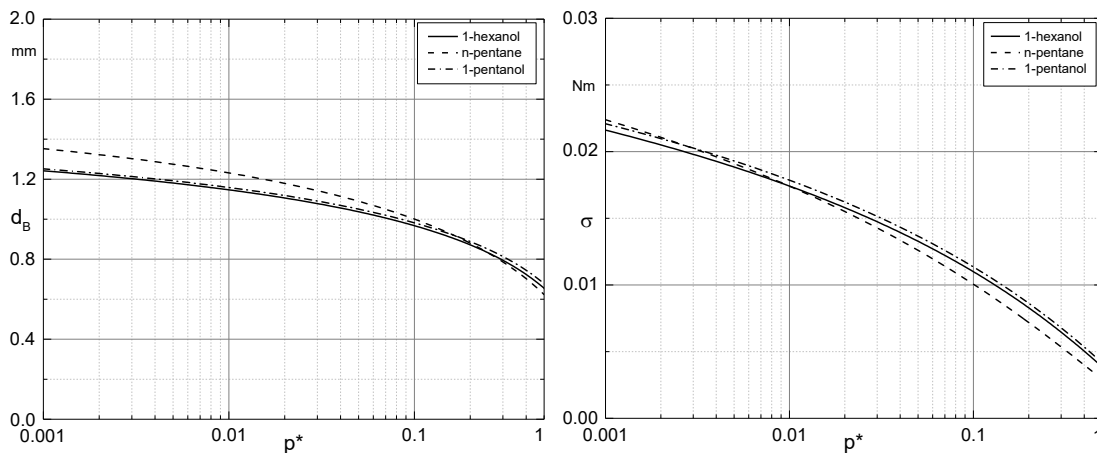


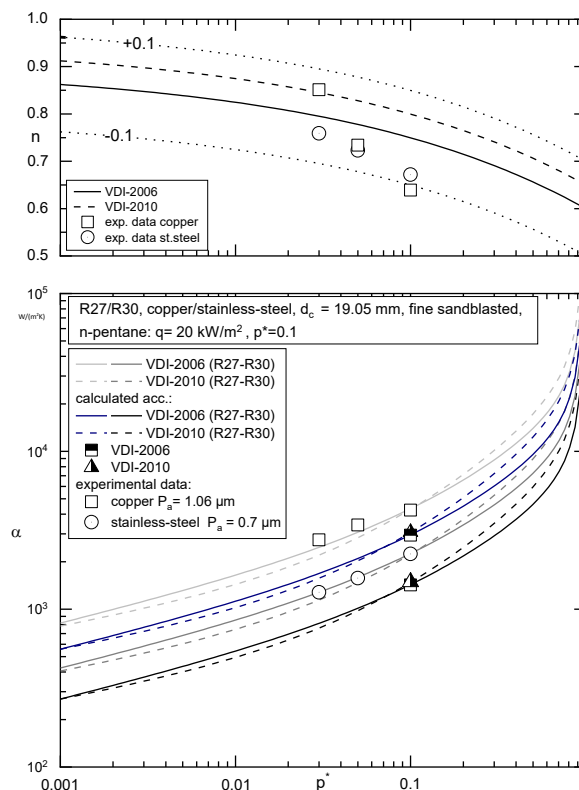
Figure 5.6:  $d_B - p^*$  (left side) and  $\sigma - p^*$  (right side) referred to the three substances analyzed: 1-hexanol, n-pentane and 1-pentanol (graph created using Origin 2016).

To conclude this paragraph, in the following figures (Fig. 5.7-5.8) two diagrams for each substance, in which the slope  $dp/dT$  (in the upper part) and the heat transfer coefficient (in the below part) are reported as function of the reduced pressure  $p^*$ . The two equations for the slope  $n$  are chosen in order to show the difference between the calculations according with VDI-2006 and VDI-2010 compared to the experimental

data. The measurement points shown correspond to the calculated slope  $n$  for  $p^*$  equal to 0.03, 0.05 and 0.1. In the diagram below the calculate curves of the heat transfer coefficients according to Gorenflo for  $\dot{q}= 20000 \text{ W/m}^2$  over the reduced pressure are entered in a double logarithmic form. The circular points represented the measured values of the heat transfer coefficients for a reduced pressure equal to 0.1, 0.05 and 0.03 with the stainless-steel tube, while the square ones referred to the copper smooth tube. Thanks to these values it is possible to build the four grey lines (light grey for the copper tube and dark grey for the stainless-steel tube) using the two equations 2.27 and 2.29 according to VDI-2006 and VDI-2010, obtaining in this way the trend of the heat transfer coefficient as a function of the reduced pressure:

$$\alpha = \alpha_0 * F(p^*) \quad (5.8)$$

Using the same procedure, it is possible to plot the curves (blue and black) referring to the values calculated according to VDI-2006 and VDI-2010.



*Figure 5.7: Influence of the reduced pressure on  $n$  and  $\alpha$  for the test substance n-pentane at  $\dot{q}=20000\text{ W/m}^2$ ,  $\alpha_0$  for  $\dot{q}_0=20000\text{ W/m}^2$  and  $p^*$  referred to the copper and stainless-steel tube (graphs created using Origin 2016).*

As it is possible to notice from the Fig. 5.7, in the upper graph, in which it is reported the slope as a function of the reduced pressure, the old correlation according to VDI-2006 fixes better the measured values. The experimental data have a decreasing trend with the increasing of the reduced pressure, as the curves obtained by means of Equation 2.26 have, because it is known that the number of active nucleation sites increases with the increasing of the heat flow density, however the relative increase in active nucleation sites falls for high reduced pressure [25]. In addition, it is possible to observe that the experimental data are located below the two monotonically decreasing curves obtained by means of the two equations previously described in the second chapter (2.27, 2.29), but at the same time all the points lie within the range of  $\pm 0.1$ . As can be seen from the graph below, starting with higher reduced pressures, the curve in accordance with VDI-2010 is initially higher than that in accordance with VDI-2006 until the value of the reduced pressure value equal to 0.1 in which they cross, changing their trend for lower reduced pressure values. As can be seen, the measured points in this case are more in agreement with the old VDI-2006 correlation both for the case of stainless-steel and copper smooth tubes. As previously done with the other graphs, diagrams referring to 1-hexanol and 1-pentanol alcohols are also shown below.

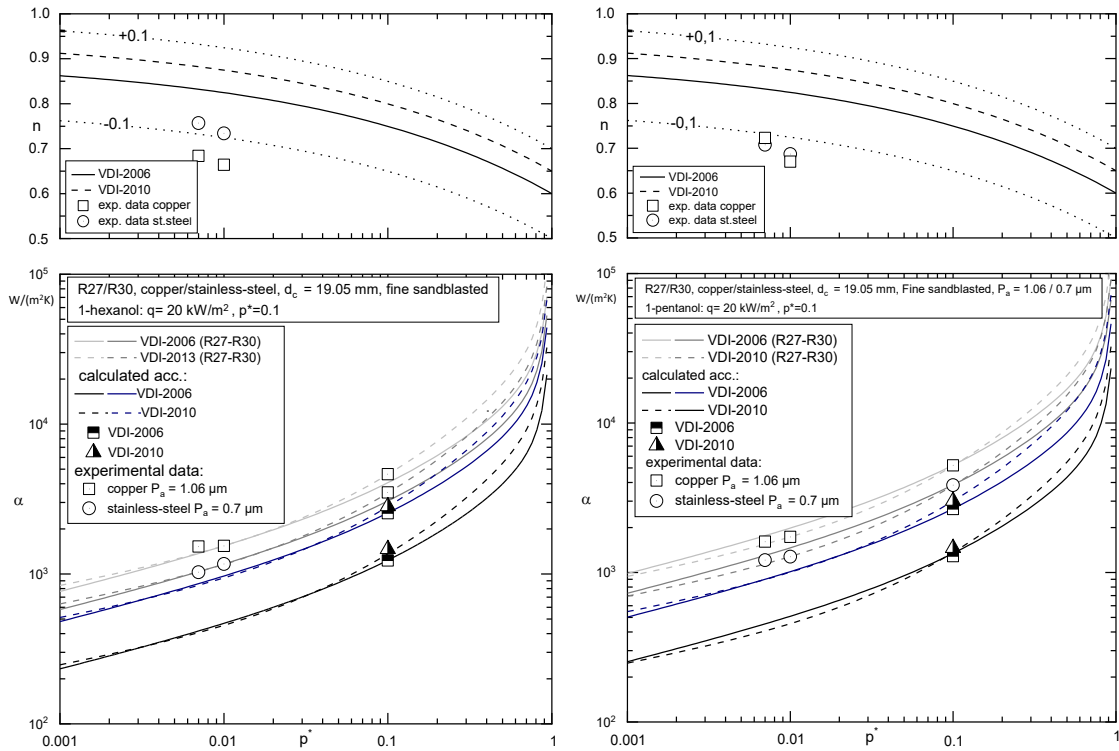


Figure 5.8: Influence of the reduced pressure on  $n$  and  $\alpha$  for the test substances 1-hexanol and 1-pentanol at  $\dot{q}=20000 \text{ W/m}^2$ ,  $\alpha_0$  for  $\dot{q}_0=20000 \text{ W/m}^2$  and  $p^*$  referred to the copper and stainless-steel tube (graphs created using Origin 2016).

On the left side of Fig. 5.8, it is possible to notice in the upper graph a decreasing gradient as a function of increasing reduced pressure, as previously it was for n-pentane. The measured values are in greater agreement with the new 2006 correlation and are also very close to the lower limit reduced pressures tolerance limit of  $\pm 10\%$ . In the graph below, since only the pressures of 0.01 and 0.007 were measured to avoid too high temperatures not compatible with the experimental apparatus, the 2010 correlation was used to get the value of the heat transfer coefficient to 0.1. It is possible to notice that the correlation VDI-2010 fits better the measured values for both values measured with the smooth copper pipe (see light gray lines) and those referring to the smooth stainless-steel pipe (see dark gray). On the right side of the Fig. 5.8, the values entered for the slopes of the regression line are below the allowed tolerance of  $\pm 10\%$  for correlation according to equation 2.24. An increase in reduced pressure from  $p^*=0.007$  to  $p^*=0.01$  results in a decrease in slope. Regarding the graph below in which the heat transfer coefficient has been represented as a function of reduced pressure, the measured



values of the heat transfer coefficient are more in agreement with the new 2010 correlation, except for the value referred to the stainless-steel pipe at the pressure of 0.007. In addition, for both alcohols it is possible to note that there is a greater distance between the measured values and the values calculated with the two correlations VDI-2006 and VDI-2010. This behavior can be due to various factors such as for example the fact that there is a certain error given by the calculation using the correlation according to VDI also in the case of n-pentane, but in this case there is a double error due to the fact that it is necessary to subsequently calculate the value referred to the pressure equal to 0.1, which is then necessary to trace the curves as a function of the reduced pressure. Furthermore, it is possible to note that there is a strong influence of the material from which the curves referred to the calculated and experimental values with the copper pipe appear to be closer than those referred to the stainless-steel values. A further discrepancy between the measured and calculated values using the copper pipe can be determined by the value of the higher roughness value (1.06 and not 0.4 as for the correlations according to VDI).

## 5.2 Measurement results for the stainless-steel finned tube

Before starting the discussion of the measured values for the finned tube, a  $\alpha - \dot{q}$  graph has been reported below taking as an example n-pentane at the reduced pressure equal to 0.1. In the graph in Fig. 5.10, the heat flux has been calculated as the ratio between the product  $U \cdot I$  (Power [W]) and the area considered. As an objective of this representation, there is to show how the heat transfer coefficient changes when we consider the core diameter ( $d_c$ ) and therefore the area  $A_c$  or the outer diameter ( $d_o$ ) and so the area  $A_o$ . For greater clarity of the areas considered, an explanatory figure (Fig. 5.9) has been provided below.

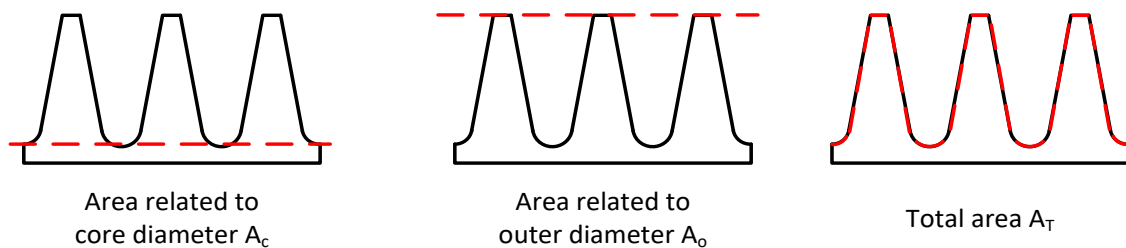


Figure 5.9: Representative figure of the different areas considered in the analysis [25].

From the formulas dealt with in chapter 2 (equations 2.1 and 2.3) it is obtained that the heat flux is inversely proportional to the heat transfer area and so at the same time to the diameter considered and being the heat transfer coefficient directly proportional to the heat flux, it is possible to deduced that by increasing the area (therefore considering the outer diameter) with the same superheating ( $\Delta T$ ) a lower value of the heat flux ( $\dot{q}$ ) is obtained and therefore a smaller value of the heat transfer coefficient ( $\alpha$ ). As for all the previous evaluations, also in this case is considered only the heat transfer coefficient in the radial direction and this is due to the construction of the experimental apparatus as the heated pipe is inserted on one side of the evaporator to allow it to stay in the desired position (horizontal) inside it and furthermore, as already explained in chapter 4 (in particular in paragraph 4.1.3), the thermocouples, which allow to detect the  $\Delta T$  are not found in the entire length of the pipe but in the 80 mm of the heating element inside the pipe. In this analysis, the heat transfer coefficient is always calculated for an average

superheat on the base of the fins considering the core diameter, instead of the true, locally variable (unknown) surface temperature along the fins.

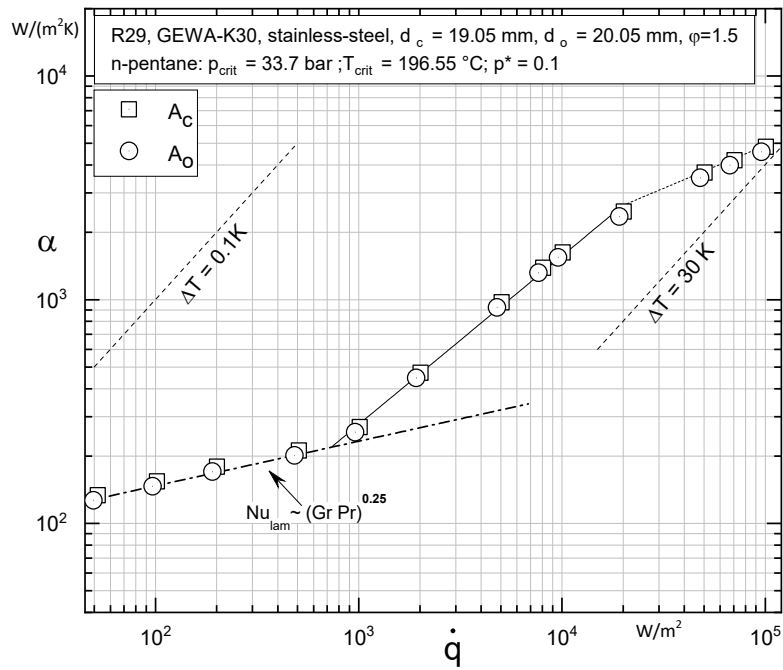


Figure 5.10: Heat transfer coefficient as a function of the heat flow density for the stainless-steel finned tubes on the test substance n-pentane under pressure variation (graph created using Origin 2016).

After this brief introduction to better understand how much the presence of an increased area can affect the heat transfer coefficient, it is possible to start analyzing the measured values obtained in the laboratory as previously done for the smooth pipes. The following diagrams (from Fig. 5.11 to Fig. 5.13) show the measurement results of the heat transfer coefficients as a function of the heat flux for tube R29 with n-pentane, 1-hexanol and 1-pentanol in comparison with the obtained result with the pipe R30.

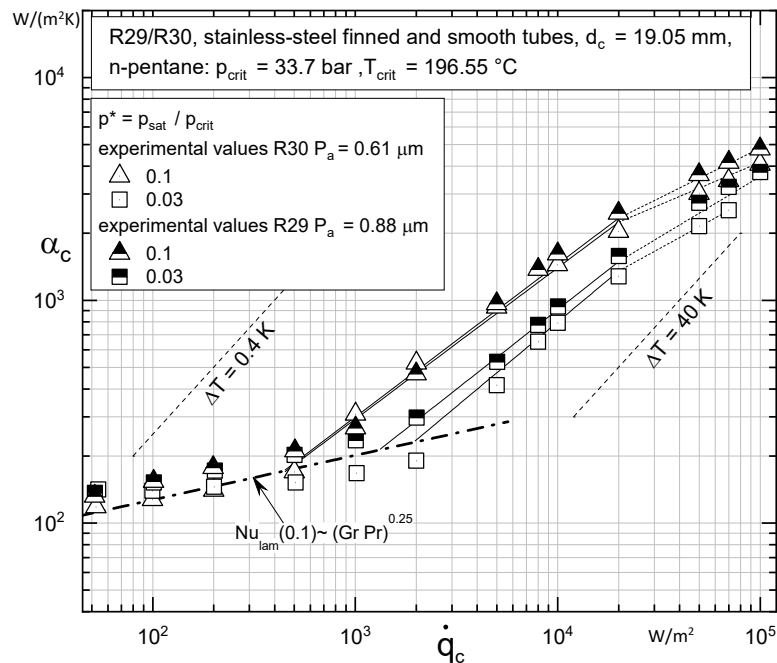


Figure 5.11: Heat transfer coefficient as a function of the heat flow density for the stainless steel finned and smooth tubes on the test substance n-pentane under pressure variation (graph created using Origin 2016).

As previously done, they have been reported in a double logarithmic graph using only the values referring to the pressures 0.1 and 0.03 to avoid the superimposition of too many curves in the graph. In Fig. 5.11 the experimental values referring to the core diameter of the stainless-steel finned tube were compared with those obtained from the smooth stainless-steel tube. The zone of low heat flux densities up to a value of 2000 W/m<sup>2</sup>, where there is mild increase in the heat transfer coefficients, displays only a slight pressure dependency. While, in the nucleate boiling zone, as has been seen for smooth tubes, there is a remarkable improvement in  $\alpha$  when the pressure increases for constant heat flux densities and higher pressures lead to an earlier onset of nucleate boiling. Within the range of initial nucleate boiling where the heat flux is low, tubes with external fins transfer heat more efficiently than smooth tube because the increase in  $\alpha$  can be derived to the great roughness at the crest of the fins and to the additional convection caused by the bubbles that rise along the flanks of the fins. The enhancement vanishes for the pressures range investigated at high heat fluxes due to trapped vapor within the grooves hinder the mass flow of superheated liquid. As a confirmation of the

fact that the point of onset of nucleate boiling is anticipated in the finned tube it is possible to use the high-speed recordings, to have a confirmation of the range in which such a point can be found. From the diagram shown in Fig. 5.11 for  $p^* = 0.1$  the heat flux value at which the first bubble is formed would appear to be between 500 and 1000  $W/m^2$  and this range can be confirmed by the images present in the Appendix in Table 8.18, where it is possible to note that the ONB point is just before 500  $W/m^2$ . Regarding the reduced pressure equal to 0.03, based on what has been said above we would expect that for lower pressures the point of formation of the first bubble will be postponed. From Fig. 5.11 it is expected a value between 1000 and 2000  $W/m^2$  and from the high-speed recordings shown in the Appendix in Table 8.18 it is possible to see that for heat flux equal to 1000  $W/m^2$  no bubbles are present while for heat density equal to 2000  $W/m^2$  the ONB was exceeded. From the trend shown in Fig. 5.11 for the hydrocarbon n-pentane, and as will be possible to see in the following graphs referring to the two alcohols analyzed (1-hexanol and 1-pentanol) after a certain heat flux the influence of the same affects less the value of the heat transfer coefficient than it did previously. One of the reasons of this behavior is because after a certain value of the heat flux there is the presence of a conspicuous number of active nucleated sites, so the greater external area due to the fins has less influence on that. In addition, the increase in surface area exerts less and less influence as the heat flux increases because after a certain time there is the formation of a vapor layer composed of bubbles and so the influence of the macrostructure on the heat transfer coefficient decreases. A physical reason for this behavior can be found in the finite thermal conductivity of the fin's material. For both the reduced pressures, the comparison shows that in the area of the natural convection, the values of the smooth tube are always below those of the finned tube and for finned tube the onset of nucleate boiling is anticipate. In the area of nucleate boiling, it is possible to observe that up to the value of the heat flow equal  $\dot{q}=10 \text{ kW}/m^2$ , the values of R29 and R30 for  $p^* = 0.1$  are really close, while for larger heat flow the slope for the smooth tube falls significantly. As it is possible to note also through the comparison of the following graphs for the two alcohols, for the hydrocarbon n-pentane there is a greater difference between the smooth and finned tubes mainly because with n-pentane were analyzed higher values of pressures, while for the two alcohols the pressures taken

into consideration are smaller, so lower will be the difference between them and therefore between the various lines in the graphs.

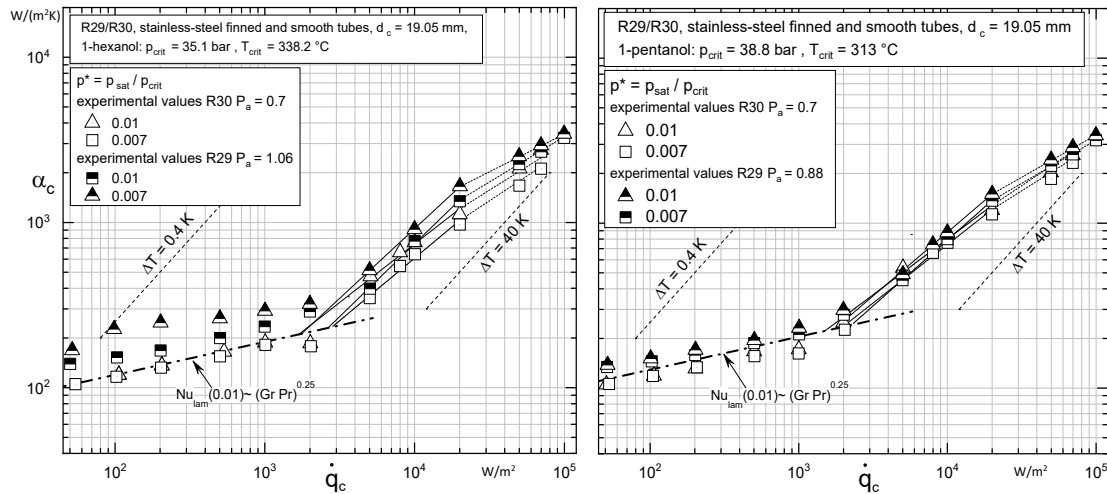


Figure 5.12: Heat transfer coefficient as a function of the heat flow density for the stainless steel finned and smooth tubes on the test substance 1-hexanol and 1-pentanol under pressure variation (graphs created using Origin 2016).

As can be seen from Fig. 5.12 on the left side (1-hexanol) during natural convection, we have that the measured values for the reduced pressure equal to 0.01 are most in agreement with the Nusselt correlation compared to the ones referred to the reduced pressure equal to 0.007. As for all the previous graphs for higher values of the reduced pressure the heat transfer coefficient is higher because for low reduced pressure there are bigger bubbles and so less liquid is in contact with the wall surface (for the larger interface between vapor and wall surface given by the high surface tension). For this reason, for higher values of the reduced pressure more we have an increase of the heat transfer by convection. Furthermore, it is possible to notice that thanks to the fins the bubbles has more time to grow between them because as it increases in size it has more time to stay in contact with the wall of the surface in the space between them. For what concern the presence of the fins it is possible to notice that in all graphs analyzed the heat transfer coefficient of the finned tube is higher than those of the plain tube for the reduce pressure taken in consideration and for both the convective and nucleate boiling area. This is due to the increase in surface area caused by the finned tube geometry and for this reason it is enhanced the formation of the bubble and greater tendency of the

liquid to remain in contact with the surface of the wall thanks to the presence of the fins which constitute a capillary structure. So, additional convective effect set in, because the bubbles through the ribs ensure better removal of the superheated boundary layer. Regarding 1-pentanol graph (on the right side of Fig. 5.12), the measured values in natural convection are for the most part higher than the Nusselt correlation for a pressure of 0.01 (except for heat flux values from 200 to 1000 W/m<sup>2</sup> lying on the line). In order to understand exactly whether the onset of nucleate boiling is anticipated due to the presence of the fins, it is worth analyzing high-speed recordings reported below. From Fig. 5.12 for the reduced pressure equal to 0.01 it is possible to assume that the ONB point is between 2000 and 5000 W/m<sup>2</sup> and the images in the Appendix in table 8.18 confirm this trend. For the lowest pressure, a higher ONB heat flux value is expected. In fact, from graph 5.12 it is possible to notice that is between 5000 and 10000 W/m<sup>2</sup>, a range also this time confirmed by the images in table in the chapter 8. While from 1-pentanol it is possible to note from table 8.19 that both for the reduced pressure equal to 0.01 and for that equal to 0.007 we have a range from approximately 2000 to 5000 W/m<sup>2</sup>. As previously done for the smooth pipes, the values of the slope of the interpolation line of the nucleate boiling and the values of the heat transfer coefficient as a function of the reduced pressure have been shown in the figures Fig 5.14 and Fig. 5.15. From equation 2.23 it is possible to obtain that the effect of the heat transfer coefficient is a function of the slope  $n$  which in turn is a function of the reduced pressure. In addition, from equation 2.24 and observing the trend of the values of  $n$  for different reduced pressures shown in the figures below, it can be deduced that having finned tubes lower slope values are obtained. This could already be guessed from equation 2.42 in which to obtain the slope of the finned tubes it is necessary to subtract a term given by the ratio between the height of the fins and the free space between them. For these reasons it is possible to reach the conclusion that the effect of heat flux on  $\alpha$  is weaker for finned tubes than for smooth ones. In figure 5.14 the influence of the pressure on the slope and on the heat transfer coefficient for the test substance n-pentane was represented. It can be seen that the experimentally measured slope values agree with the old VDI-Atlas (2006) correlation. Furthermore, even if it has been demonstrated theoretically that the slope of the interpolation line of the measured values

should be lower than that referred to smooth pipes, we have that in the analyzed case it turns out to be contrary to the expected trend. The same thing can be observed for alcohols, as can be seen from the figures shown below (see Fig. 5.15). In the diagram on the bottom part ( $\alpha - p^*$ ) it is possible to notice that the correlation VDI-2006 fits better the measurement results especially for the reduced pressures  $p^* = 0.1$  and  $p^* = 0.05$ , while for  $p^* = 0.03$  the measured value is above both the correlations. The distance between the curves referring to the measured and calculated values is not large and can be determined by various factors including the fact that, unlike what is taken into consideration by VDI (copper tube with trapezoid shape and  $t_l$  not much smaller than 1 mm); in this case a stainless-steel threaded tube with different geometry and roughness was used.

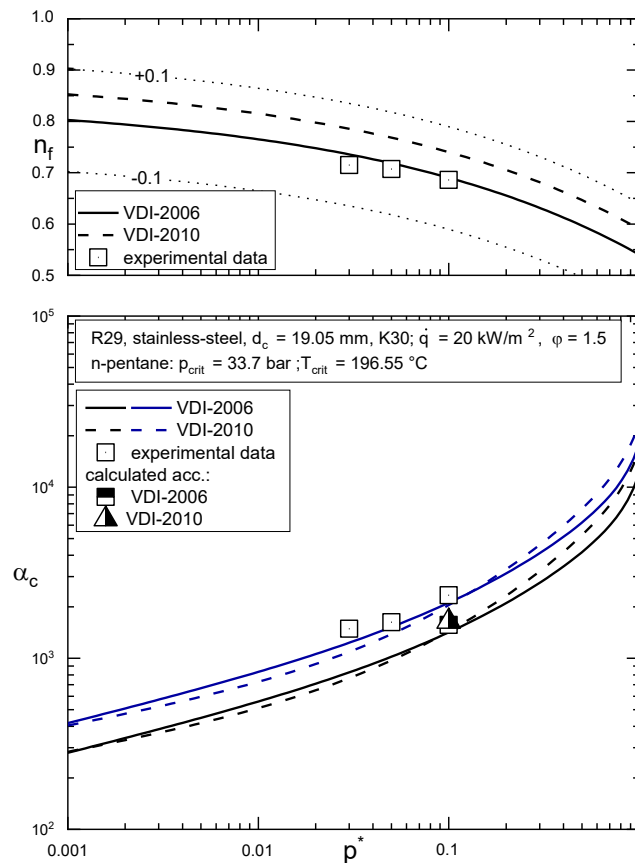


Figure 5.13: Influence of pressure on  $n$  and  $\alpha$  for the test substance  $n$ -pentane at  $\dot{q} = 20 \text{ kW/m}^2$ ,  $\alpha_0$  calculated for  $\dot{q}_0 = 20 \text{ kW/m}^2$  and  $p^* = 0.1$  (graph created using Origin 2016).



The figure below shows the two graphs for the two alcohols analyzed, the one referring to 1-hexanol on the left side and the one referring to 1-pentanol on the right side. In both graphs the square points represent the slope of the experimental data for the values measured with the finned tube. These values for both substances are in or very close to the  $\pm 0.1$  range. As far as the values for 1-hexanol are concerned, they are more in agreement with the VDI-2010 correlation, especially the value referring to the reduced pressure of 0.01. As far as the slope values for 1-pentanol are concerned, the value referring to the reduced pressure of 0.07 is more in agreement with the VDI-2010 correlation, while the value referring to the pressure of 0.01 is more in agreement with the VDI-2006 correlation. With regard to the values referring to the  $\alpha - p^*$  diagram for both alcohols, the new correlation fits better the experimental results. In addition, it is possible to note that unlike what can be observed from Fig. 5.14 referred to the hydrocarbon in which the curves are closer; in this case the difference between the curves referred to the experimental values and those calculated according to VDI is considerable. The justification for this behavior can be given by the fact that (as has been seen for smooth pipes) in this case a double calculation was carried out to obtain the value of the heat transfer coefficient, starting from the experimental data referred to the reduced pressure equal to 0.01. Therefore, since there is probably an error in the VDI calculation methodology, it consequently also appears to be carried forward in subsequent calculations. The conspicuous difference between the curves is also determined by the fact that unlike the copper tube used for the equations according to VDI, in the case analyzed in this work a stainless-steel threaded tube with a different geometry and roughness was used.

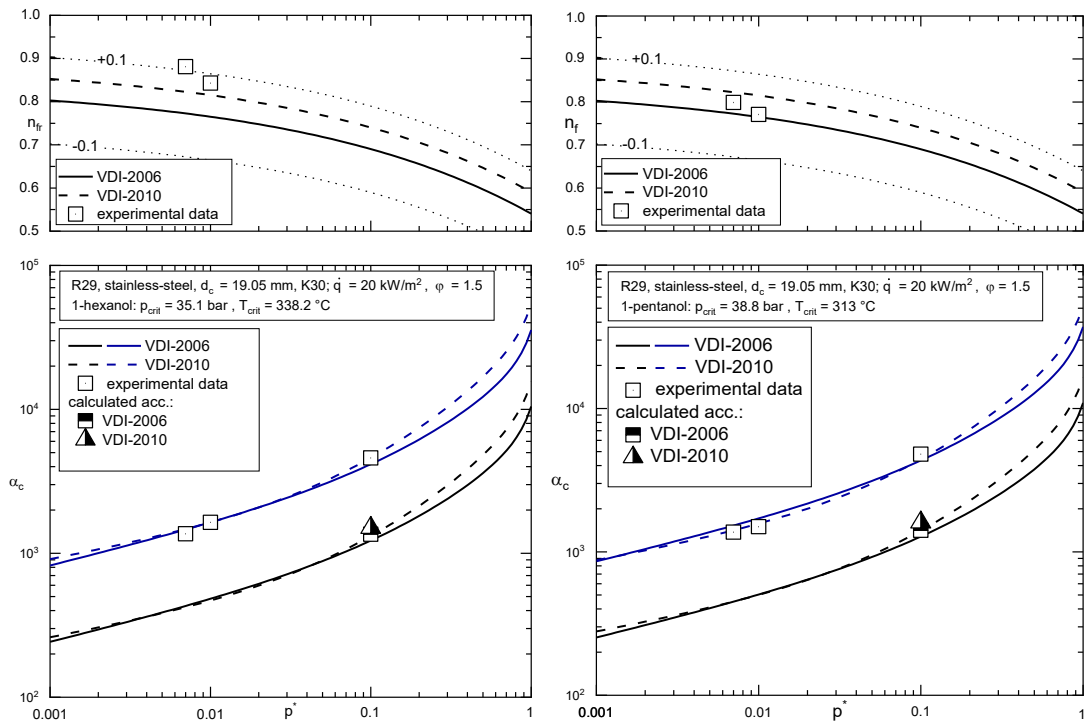


Figure 5.14: Influence of the reduced pressure on  $n$  and  $\alpha$  for the test substance 1-hexanol and 1-pentanol at  $\dot{q}=20$  kW/m<sup>2</sup>,  $\alpha_0$  calculated for  $\dot{q}_0=20$  kW/m<sup>2</sup> and  $p^*=0.1$  (graphs created using Origin 2016).

### 5.3 Comparison on the tube wall superheating for the different substances

This paragraph will consider all azimuthal temperature distributions with respect to the angle of thermocouple positioning, for all pipes and substances used to understand the influence of overheating on the heat transfer coefficient. As described in chapter 4.1.4 the thermocouples are arranged symmetrically all around the heat pipe, with a distance between one and the other of  $30^\circ$ . For this reason, given the symmetry of the arrangement of the thermocouples and of the tube structure, the temperature measurement of one of them can be approximated by the measurement of the thermocouple placed symmetrically to it like a mirror, as shown in Fig. 5.15.

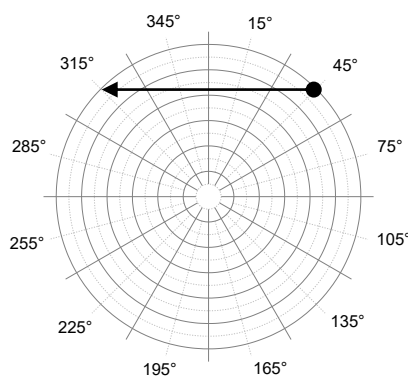


Figure 5.15: Disposal around the heating pipe of the thermocouples (graph created using Origin 2016).

In the following Fig. 5.16 it is reported the comparison between the azimuthal temperature distribution for the hydrocarbon n-pentane at a selected pressure equal to 0.1 with copper and stainless steel smooth tube in two  $\Delta T - \varphi$  diagrams. It should be noticed that for n-pentane with copper tube R27 (on left side) the measured values for the thermocouples at points  $75^\circ$  and  $285^\circ$  are not taken into account, as they are defected. While the superheating at point  $\varphi = 135^\circ$  is a reflection of the data from  $\varphi = 225^\circ$  and the same is for the point  $345^\circ$  respect to the angle  $15^\circ$ . Regarding the stainless steel tube R30 (on the right side) there are the same thermocouples that are defected and the overheating entered at point  $\varphi = 315^\circ$  is a reflection of the data from  $\varphi = 45^\circ$  and the same is for the point  $345^\circ$  respect to the angle  $15^\circ$ . The data for  $p^*=0.05$  and  $0.03$  for both the tubes are reported in the Appendix (chapter 8) and are not considered in detail

in this chapter. To begin comparing the two graphs, it is necessary first to analyze the properties of the two materials used (stainless-steel and copper) summarized in Table 5.7 below, taken from the web site of the Wieland, company producing the tubes used.

*Table 5.7 Material values ( $\vartheta = 20\text{ }^{\circ}\text{C}$ ) for stainless steel and copper, as well as thermal conductivity, heat penetration coefficient and influence of the thermal heating wall properties calculated according to the VDI HEAT ATLAS [10]:*

<b>Material</b>	<b>Material number</b>	$\lambda$ [W/m·K]	<b>Cp</b> [J/kg·K]	$\rho$ [kg/m <sup>3</sup> ]	<b>a</b> [m <sup>2</sup> /s]	<b>b</b> [Ws <sup>0.5</sup> /m <sup>2</sup> ·K]
stainless-steel	14571	15	500	8000	$3.75 \cdot 10^{-3}$	7745.96
copper	20040	394	385	8960	$114.2 \cdot 10^{-3}$	36866.54

In this way it is possible to notice that the diagrams referred to the copper smooth tube (reported on the left side of the Fig. 5.16), thanks to the really high thermal conductivity of the copper (around 394 W/m·K) compared to the one of stainless-steel (around 15 W/m·K) has really low tube wall superheating  $\Delta T$  than the stainless-steel tube. In fact the copper tube has a really high ability to conduct heat and a high value of the thermal diffusivity that is the ratio between the thermal conductivity and the product between the density and the specific heat capacity. In this way, with the copper tube it is possible to reach really high value of the heat transfer coefficient because this is due to the fact that the thermal conductivity influences the Nusselt number, which in turn influences the heat exchanged through convection.

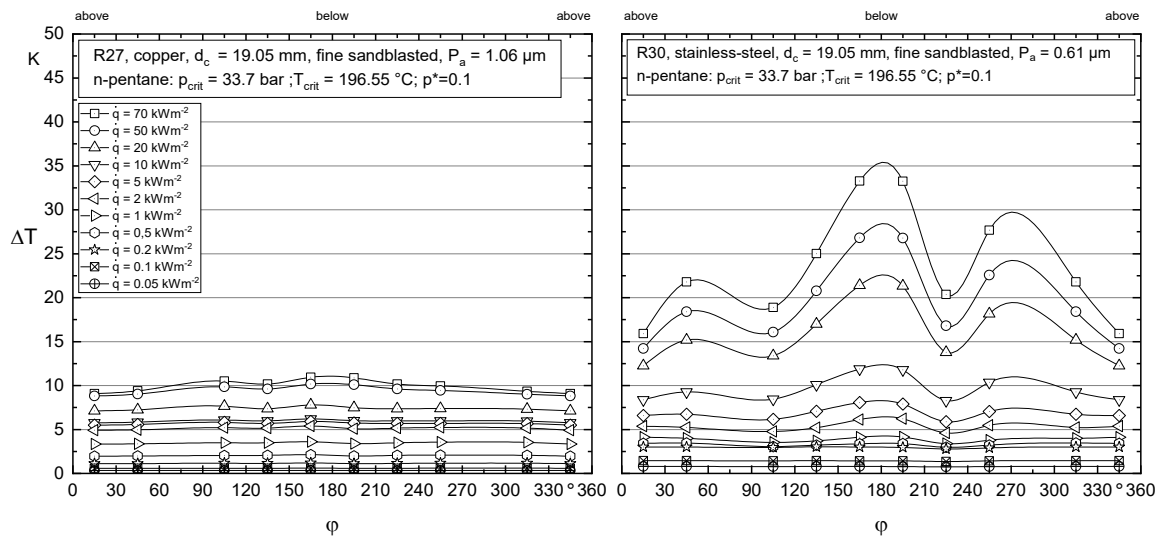
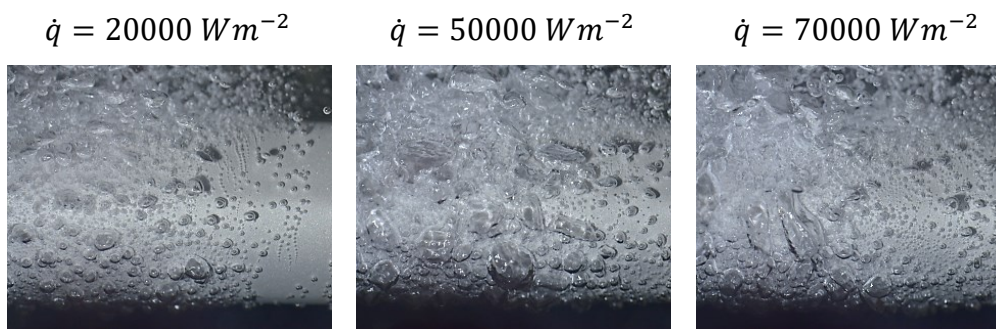


Figure 5.16: Comparison on the tube wall overheating with *n*-pentane (hydrocarbon) between the copper smooth tube and the stainless-steel tube, shown in the  $\Delta T - \phi$  diagram for a reduced pressure of  $p^*=0.1$  (graph created using Origin 2016).

In addition, it is possible to observe, from the trend of the tube wall overheating, shown in Fig. 5.16 (especially for the stainless-steel pipe), that the tube wall overheating increases with the rise of the heat flux density. Depending on the azimuthal position of the thermocouples, the degree of overheating varies due to the influence of the reduced pressure, the pipe diameter and the respective heat flow density. From  $\dot{q}=5000\text{ W/m}^2$ , it is clear that the overheating of the pipe increases at the bottom and decreases towards the sides. A physical justification of this is provided by the principle of the convective effect. As the heat flow density increases, the growing bubbles accumulate on the underside of the tube, causing them to act as an insulating layer, impairing the heat transfer. After the bubbles have broken off, they scroll further the outside of the tube due to lower density, taking more bubbles with them. Due to the rising bubbles, the liquid is mixed on the flanks of the tube, and the heat transfer improves due to the streams that are created. This effect is less pronounced for lower heat flux densities, and a clear difference between the local overheating is not discernible. This is due to a lower nucleation site activity for lower heat flux densities and a larger bubble break-off diameter. As we will see later thanks to the comparison between smooth and finned tube, the bubbles formed in the lower part of the smooth tube tend to stay longer in that

position before leaving that location and heading for the upper part of the tube thanks to the lower density. The behavior thus described can be confirmed by the high-speed recordings reported below where we can see, as suggested by the diagram in Fig. 5.16, that from more or less 20 kW onwards, a conspicuous layer of bubbles can be seen at the bottom of the pipe surface. These bubbles with the increasing of the heat flux rise in the lower part of the surface and at the same time they tend to become larger moving to the upper part of the tube due to the lower density. This is due to the fact that they tend to boost in number by having a higher number of active nucleation sites and therefore they tend to collide with each other more, increasing their volume.

Table 5.8: High speed recordings of the stainless-steel smooth tube (R30) with n-pentane at  $p^*=0.1$ .



A similar comparison can be made for the two alcohols 1-hexanol and 1-pentanol between the copper and stainless-steel smooth tube. To avoid falling into repetition of concepts already mentioned, the comparison will be performed only using the alcohol 1-hexanol at the reduced pressure equal to 0.01, as shown in the figure below (Fig. 5.17). On the left side it is displayed the tube wall overheating distribution with copper tube (R27) in which the superheating entered at point  $\varphi = 135^\circ$  is a reflection of the data from  $\varphi=225$ , the one at  $\varphi=285^\circ$  of  $\varphi=75^\circ$  and the one at  $\varphi=345$  of  $\varphi=15^\circ$ . While on the right side it is reported the graph for the stainless-steel smooth tube (R30) in which the measured values for the thermocouples at points  $75^\circ$ ,  $135^\circ$ ,  $225^\circ$ ,  $285^\circ$  are not taken into account, as they are defected. The overheating entered at point  $\varphi= 315^\circ$  is a reflection of the data from  $\varphi=45^\circ$  and the one at  $\varphi=255^\circ$  of  $\varphi=105^\circ$ .

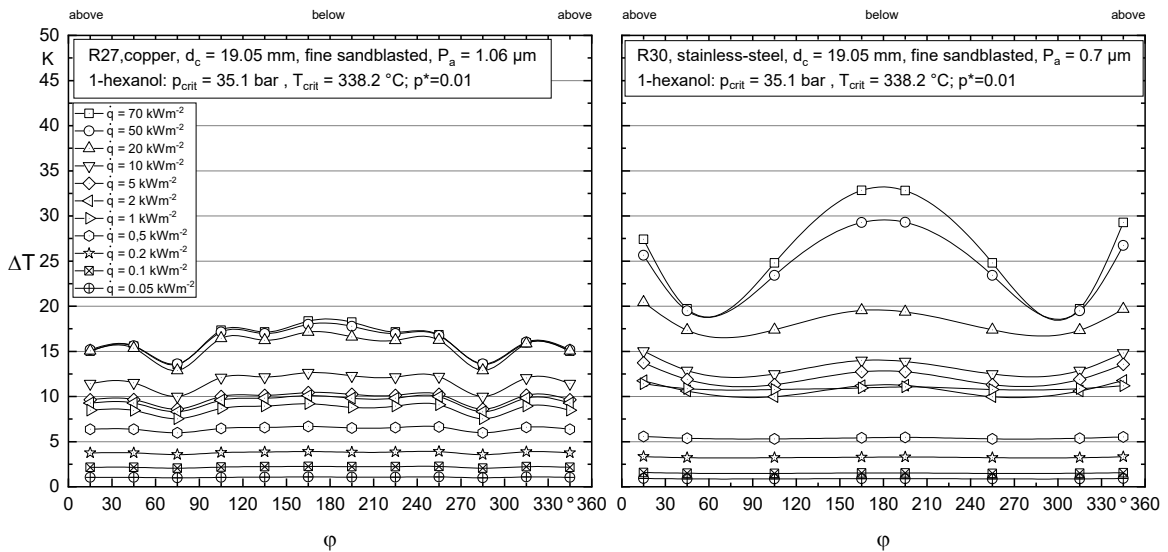


Figure 5.17: Comparison on the tube wall overheating with 1-hexanol (alcohol) between the copper smooth tube and the stainless-steel tube, shown in the  $\Delta T - \phi$  diagram for a reduced pressure of  $p^* = 0.01$  (graph created using Origin 2016).

The curves shown in Fig. 5.17 show that the pipe wall overheating  $\Delta T$  up to a heat flow density of  $q = 500 \text{ W/m}^2$  is evenly distributed around the circumference. While, as shown previously with an increase of the heat flux density there is an increase in tube wall superheat. From  $q = 1 \text{ kW/m}^2$ , different levels of overheating occur at the various thermocouple positions. Overheating is most pronounced on the underside, and it decreases over the flank side. The justification for this trend is comparable to the explanation seen previously. For a complete view of the phenomenon in the figure below (Fig. 5.18) there is the comparison between the smooth (R30) and finned (R29) stainless-steel tube.

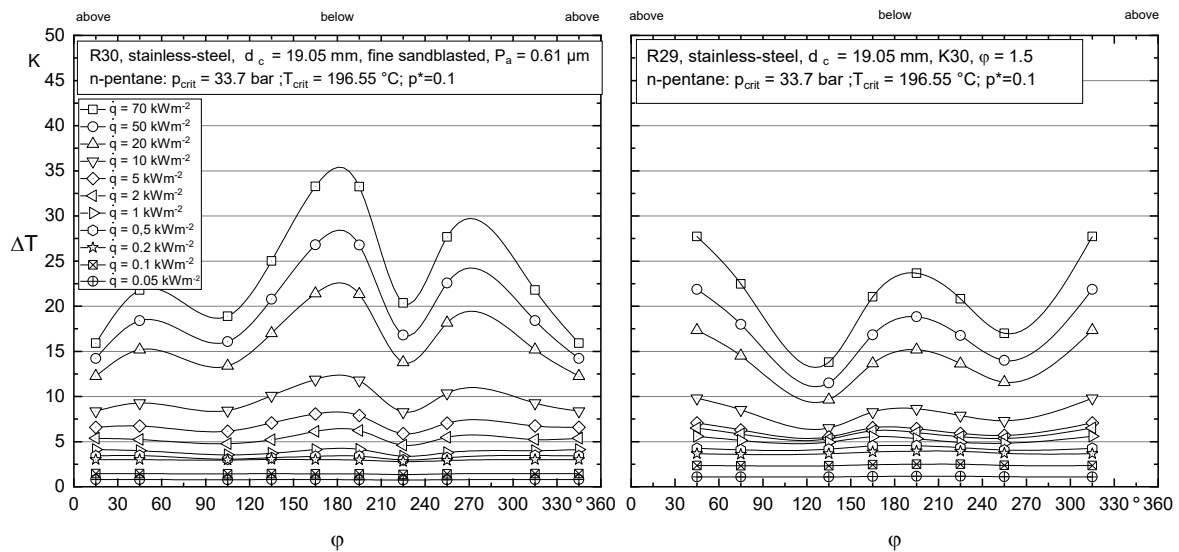


Figure 5.18: Comparison on the tube wall overheating with n-pentane (hydrocarbon) between the stainless-steel smooth tube and the stainless-steel finned tube, shown in the  $\Delta T - \phi$  diagram for a reduced pressure of  $p^* = 0.1$  (graph created using Origin 2016).

The Fig. 5.18, reported above, shows the comparison between the azimuthal temperature distribution for the hydrocarbon n-pentane at a selected reduced pressure equal to 0.1 with smooth tube and with finned tube in two  $\Delta T - \phi$  diagrams. The same consideration related to the thermocouples used in the stainless-steel smooth tube described previously is now considered. For what concern the stainless-steel finned tube the thermocouples at  $\phi = 15^\circ$  and  $\phi = 345^\circ$  are not taken into account, as they are defected. The overheating entered at point  $\phi = 315^\circ$  is a reflection of the data from  $\phi = 45^\circ$  and the same for  $\phi = 285^\circ$  and  $75^\circ$ . As it is possible to observe, the superheating  $\Delta T$  of the finned tube is diminished below the plain tube, particularly at the bottom of the tube. This heat transfer enhancement is caused by the nucleation sites getting activated mainly by the superheat near the bases of the fins being somewhat higher than on the rest of the fin surface, and by the bubbles sliding upwards between the fins. With increasing heat flux and pressure, nucleation increases and the gaps between the fins are filling up with vapour, so this effect loses importance. This behavior is determined by the geometry of this tube due to the presence of the fins and thus to the fact that we have more surface available, because the bubbles are formed inside two cavities (capillary structure). In addition, it is possible to give a further physical motivation of such behaviour because, as mentioned at the beginning of this chapter, when we have smooth



tubes the bubbles find it more difficult to go up the tube, when we have finned tubes the bubbles stay less time in the area below being driven by the geometry of the tube upwards thus increasing the convective exchange of fluid around the surface. This effect is most evident for higher heat flux densities, thus demonstrating that the relative effect of convection on the enhancement is highest when a comparatively small number of big bubbles is generated [27]. It is also possible to go and make a comparison for the finned tube between the graph shown in Fig. 5.18 referring to the reduced pressure of 0.1 and the one in the Appendix in Fig. 8.7 referring to the reduced pressure of 0.03. At the lowest reduced pressure, the same relative heat transfer enhancement occurs at higher heat fluxes because less and bigger bubbles are generated, and therefore a smaller part of the vapor-liquid interface is exposed to the superheated liquid layer near the finned wall. In addition, the fact that for lower reduced pressures there is more superheating is due to the fact that for higher reduced pressure the many small bubbles produced near the bottom of the tube and the sliding upwards between or on the fins will enhance local heat transfer on the lower parts of the tube against the situation at lower pressure with a much smaller number of bubbles growing at the bottom [27]. As the convective motion of the liquid surrounding the tube increases, overheating decreases, so it improves the heat transfer coefficient by convection and additional evaporation. At high heat fluxes, the sliding bubbles lose importance and the differences in  $\Delta T$  between bottom and top of the tube tend to vanish, because the surface is more or less entirely covered by the bubbles. A similar behavior can be also observed in the case reported below in Fig. 5.19 for alcohol 1-hexanol. The diagrams show the test substance 1-hexanol related to the core diameter  $d_c = 19.05$  mm of the smooth tube (on the left side) and on the finned tube (on the right side). As previously explained, the comparison demonstrates the significant influence of convective effects caused by the sliding bubbles streaming upwards along the tube surfaces.

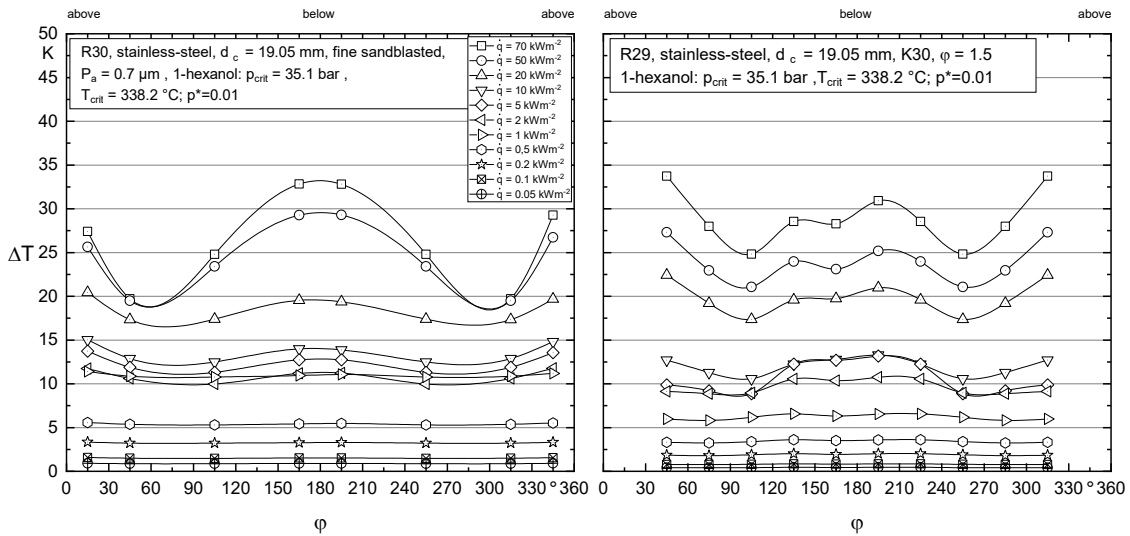


Figure 5.19: Comparison on the tube wall overheating with 1-hexanol (alcohol) between the stainless-steel smooth tube and the stainless-steel finned tube, shown in the  $\Delta T - \varphi$  diagram for a reduced pressure of  $p^* = 0.01$  (graph created using Origin 2016).

For the smooth tube, the same thermocouples working and the same ones reflected, as in the case previously analysed, are considered in Fig. 5.17. While for the finned tube the thermocouple at position  $\varphi = 15^\circ$  and  $345^\circ$  are not taken in consideration and the thermocouples at the position  $\varphi = 105^\circ$ ,  $135^\circ$ ,  $285^\circ$  and  $315^\circ$  are mirrored with respect to their symmetrical positions. It should be noted the influence of heat convection due to the presence of the fins in this diagram because, as in the case of n-pentane, we can see that this leads to a lower  $\Delta T$  that increases the heat transfer coefficient. Given this analysis it would seem that the use of finned tubes has only advantages over the use of plain tubes, but obviously for a complete analysis it should also be considered the fact that with the use of finned tubes there is an increase in the possibility of deposits forming on them, that with time leads to a decrease in performance. In addition, it should be considered economic and production aspects as there is an increase in cost and the production of these tubes is more complex having metal ribs for the increase of the external surface. These aspects are not considered in this analysis, because it was only attempted to describe what was obtained through experimental data through possible physical justifications of that phenomenon.

## 5.4 Comparison with other correlations

In order to explain the experimental results obtained in this work for finned tubes in this passage, the correlation according to Slipcevic [2] described in the paragraph 2.4.3, is used for the comparison. For this purpose, the following Fig. 5.20 shows the experimental values of the exponents of the interpolation lines, as well as the calculated curves in the  $n$  over  $p^*$  diagram. The lower plot compares the experimental values of the heat transfer coefficients with the calculated curves according to Gorenflo [1] and Slipcevic [2] in a  $\alpha - p^*$  diagram. The exemplary test substances used for the comparison are hydrocarbon n-pentane (on the left side) and the alcohol 1-hexanol (in the right side).

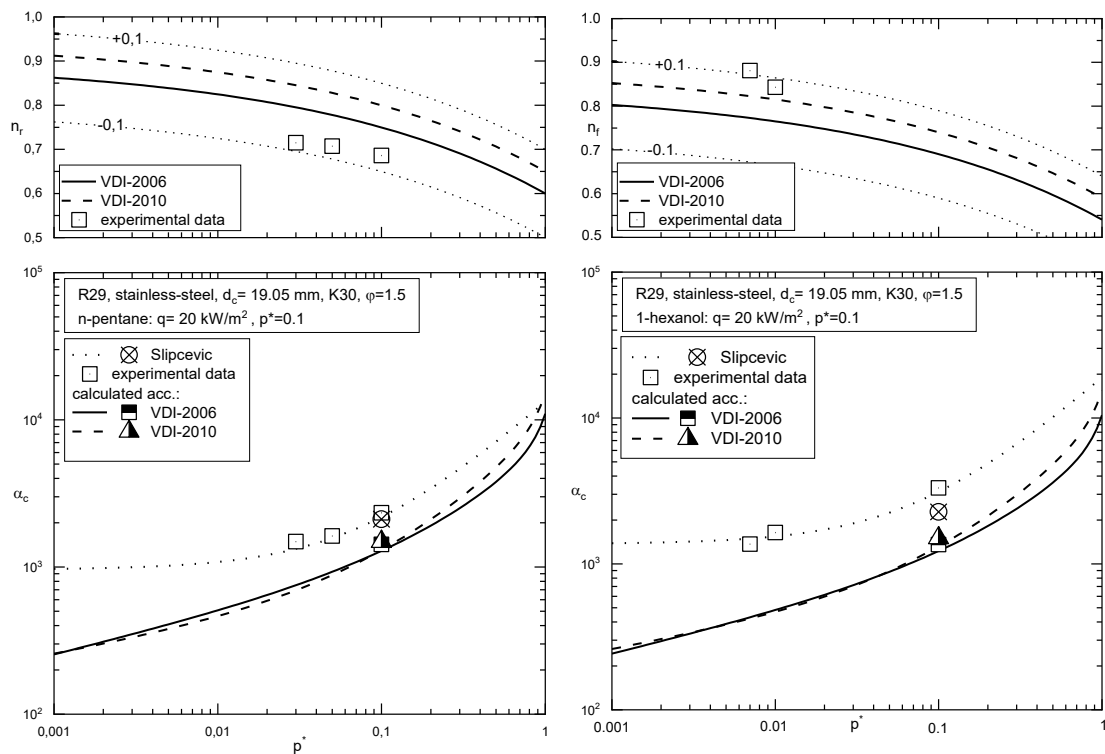


Figure 5.20: Comparison of the correlations according to VDI-Heat-Atlas [10] and Slipcevic [19, 20] with n-pentane and 1-hexanol (graph created using Origin 2016).

For the calculation of the heat transfer coefficient as a function of the reduced pressure, the empirical formula for the pressure dependence of the heat transfer in the boiling of the refrigerants according to Gorenflo [28] is used:

$$\frac{\alpha_{p^*=0.1}}{\alpha_{p_0^*=0.03}} = \frac{F_{(p^*=0.1/1.225)}}{F_{(p^*=0.03/1.225)}} = 0.68 + 10.68 \cdot \left( \frac{p^*}{1.225} \right) \quad (5.9)$$

where 1.225 is the ratio between one and the increase of the area (1/0.488). As can be seen from graphs in Fig. 5.20, for both the substances the Slipcevic correlation is in better agreement with the experimental data than the values calculated according to VDI-Heat-Atlas (2010). This may be motivated by the fact that, as previously seen, the correlations of VDI are obtained by analyzing copper pipes, while in the case of Slipcevic, as seen in the chapter 2, there is a direct dependence on the fin's material because the thermal conductivity of which the fins are made is present in the equation 2.51. If we analyze the two graphs separately, in the graph for n-pentane, all the three experimental values lie on the curve. The dashed curve for Slipcevic is created using formula 5.9, which, unlike the calculations carried out so far in this analysis, has the reduced pressure as a reference value of 0.03 and not 0.1, as it was in the old version of [1]. The values calculated by means of VDI [1] are below the experimental values, especially for lower values of the reduced pressure, while with the increasing of the reduced pressure, the Slipcevic correlation and the correlation according to VDI; tend to converge at the same point. So, whereas the measured value referred to pressure 0.1 is 2334 W/m<sup>2</sup>, the value calculated by means of the formulas described in chapter 2 according to Slipcevic's theory, referring to the same reduced pressure, turns out to be 2115 W/m<sup>2</sup>. Regarding the 1-hexanol case, on the right side of the Fig. 5.20, it is possible to notice as was also done earlier in this chapter, that the experimental values and those calculated according to the VDI correlation can be further apart. Also in this case, the dashed curve is constructed using equation 5.9 referring to the reduced pressure of 0.03, but since it is not possible to measure high pressures with this substance in the used apparatus, the experimental value referring to the reduced pressure of 0.1 is calculated using equation 5.9, passing first from the reference pressure of 0.03. Here too, the experimental values lie on the curve created in this way, although the

value referring to the reduced pressure of 0.007 lies slightly below it. In addition, it can be seen here that the calculated value according to Slipcevic is evidently below the curve referring to the experimental values, in contrast to the previous observation for n-pentane hydrocarbons, where they almost coincided. It is important to note, however, that the calculated point is still well above the correlations calculated via VDI-2010, and that it is therefore better to predict the behavior of these values. It is therefore possible to assume that this correlation is better suited for certain substances than others (in this case the hydrocarbon n-pentane compared to alcohol 1-hexanol) and that this correlation is probably usable for low pressures rather than high ones as it is possible to note the two curves converge for higher values of the reduced pressure. Obviously, these assumptions will have to be confirmed through other experimental checks. At the University of Kassel, they are currently studying a possible solution for obtaining a correlation that can better predict this behavior in threaded pipes with the use of different materials in a wide range of reduced pressures and thus update the formulas present in VDI.

## 5.5 Comparison of measurement results for hydrocarbons

Various literature data are available on boiling in free convection, which will be compared with experimental data in this section. The following diagram in Fig. 5.21 represents in a  $\alpha - \dot{q}$  diagram the comparison among the experimental values measured by P. Bujok (2015) [29], those measured by Buchholz (2023) [30] and those calculated according to VDI-Heat-Atlas [1] with a reduced pressure of  $p^* = 0.1$  and the substance n-pentane. For this purpose, the following Table 5.10 lists the most important information of the test tubes used in the literatures for the comparison.

Table 5.10: Characterizes of the smooth tubes used in the research works of P.Bujok [29] and N. Buchholz [30].

author	material	$P_a[\mu\text{m}]$	surface processing	heated length [mm]	outer diameter [mm]
P. Bujok	mild steel	0.50	drawn	80	19.05
N. Buchholz	copper	0.43	fine sandblasted	200	19.05

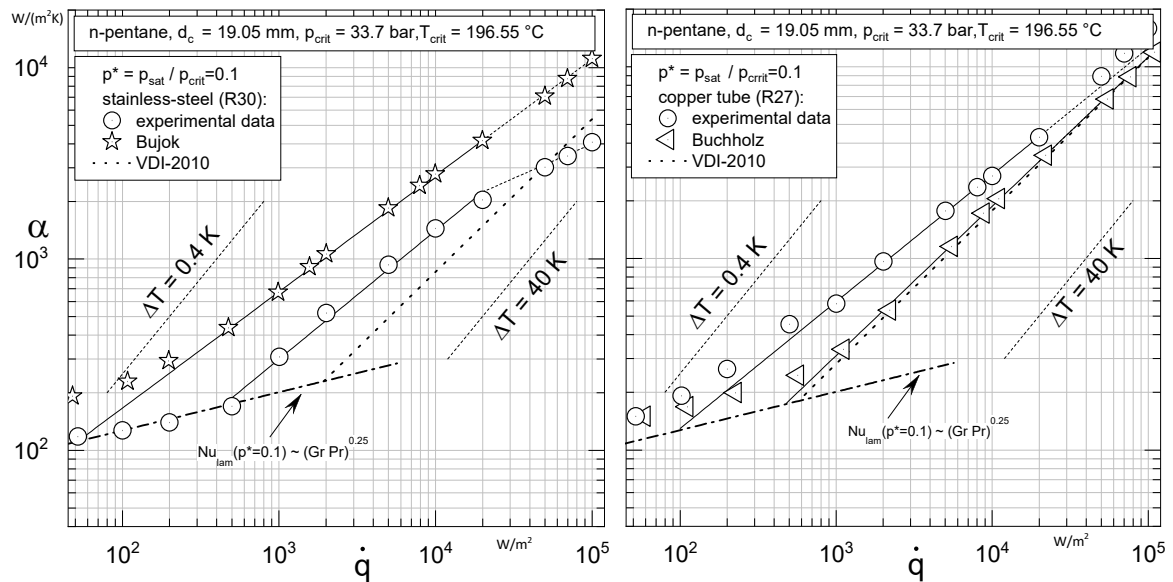


Figure 5.21: Comparison of measurement results for the hydrocarbon n-pentane on smooth stainless-steel and copper pipes (graph created using Origin 2016).

From Fig. 5.21 (on the left side), it can be seen that the experimentally measured values in this analysis are more in agreement with those calculated according to VDI-2010 compared to the Bujok ones; although the ONB point appears to be earlier and then has a strong slope variation in the developed part of the nucleate boiling zone. While the values obtained from Bujok turn out to be much higher than both the measured and calculated values according to VDI, just as the ONB point turns out to be much earlier. As far as the copper tube is concerned, the values obtained experimentally by Buchholz (on the right side) are very much in agreement with the values calculated with VDI, unlike the experimental data obtained in this work. As can be seen from the picture, for high heat flux values, the measured values are in better agreement with the lines referred to in the literature, while a conspicuous difference can be seen for the ONB value. This behavior can be attributed to the fact that the copper pipe has a roughness of 0.43 in Buchholz's case, and likewise, as explained in chapter 2, a reference roughness of 0.4 is used for the values calculated according to VDI, whereas the experimental values have a higher roughness of 1.06, and thus, as explained in the previous chapters, increased surface roughness tends to move the nucleate lines to the left, implying improvement in the nucleate boiling heat transfer characteristics. In addition, it is possible to see that the influence of the roughness tends to decrease with increasing heat flux and reduced pressure [32]. In the following Fig. 5.22, the measurement results of the finned tube of this work with the substance n-pentane for the reduced pressure equal to 0.1, are compared with the experimental data obtained by Bujok [29] for  $p^*=0.1$ . Bujok used a low finned GEWA-K30 tube, and the technical data are listed in Table 5.11.

*Table 5.11: Characteristics of the finned tubes by Bujok [29].*

<b>author</b>	<b>material</b>	<b>fin height <math>h</math> [mm]</b>	<b>fin width <math>b</math> [mm]</b>	<b><math>\varphi</math></b>	<b>heated length [mm]</b>	<b>outer diameter [mm]</b>
Bujok	Mild steel	0.90	0.20	2.6	65	17.2

The experimental results of Bujok are above compared to the calculated values according to VDI and the first bubble formation occurs earlier. While the values obtained experimentally are more consistent with the values obtained with the correlations of VDI-Heat-Atlas, which are obtained from equation 2.43 in which the heat transfer coefficients for finned tube and smooth copper tubes at about  $100 \text{ kW/m}^2$  and  $p^* = 0.1$  are the same. Probably this variation between the calculated values obtained through the correlations according to VDI and the experimentally measured values lies in the use of different fin geometry and the use of a different heating surface material. In fact, the correlation used for the calculation of the values in accordance with VDI is valid only for values with the free space greater than 1 mm and moreover, and as often happens in the literature available at the moment, this correlation refers to a copper pipe while in this analysis a finned stainless-steel tube is used. As it is possible to notice, initially the values obtained by Bujok looks to be very distant from those obtained measured in this work, but for higher values of the heat flux this difference appears to be smaller.

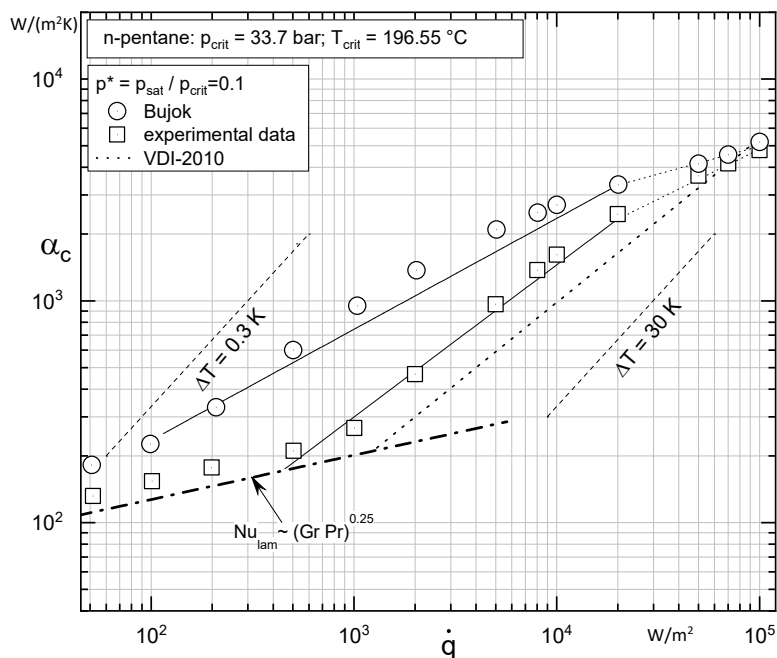


Figure 5.22: Comparison of measurement results for the hydrocarbon n-pentane for a reduced pressure equal to 0.1 on finned tube and the values in the available literature (graph created using Origin 2016).



Also in this case the conspicuous variation between Bujok and the experimental data can be associated with a different geometry of the tube as well as the fact that, unlike in the case studied, the tube used by Bujok was made of mild steel. The test substances 1-pentanol and 1-hexanol rarely appear in the available literature, so it would lose its significance to consider the comparison by having to evaluate too many variables other than those analyzed in this study.

### 5.6 Effect of the material on the thermal heating wall properties

To increase the heat transfer on evaporator tubes, optimized surface structures and heating wall materials with a high heat penetration rate are used. In the specialist literature, empirical and semi-empirical calculation method are mainly for the heat transfer during the boiling of refrigerants on differently structured treated surfaces and heating wall materials under moderate pressure. However, investigations into the influence of the heating wall material are largely limited on copper, although further and more recent studies are now moving towards the use of different materials. As was seen at the beginning of this work, it is possible to obtain the influence of the material on the heat transfer coefficient according to VDI-2010 [1], from the equation 2.33. However, according to a recent study, it is possible to extract a more appropriate value for the exponent of this equation from the PhD thesis of doctoral student Christian Wengler [32] in which there is, compared to the VDI-Heat-Atlas a reduction of the exponent of the heat penetration coefficient from 0.5 to 0.33, as shown in equation 5.10:

$$F_{WM_w} = \sqrt{\left(\frac{e}{e_{Cu}}\right)^{0.33}} \quad (5.10)$$

This gives an increase of the digressive course for the influence of the thermal heating wall property with decreasing heat penetration coefficient (effusivity) and so with a lower rate at which the material can absorb heat. As we can see from the Table 5.8, it is possible to make a comparison between the calculated and measured values with the

new and old VDI-Heat-Atlas correlation, also considering the influence of the material. In the table shown below, values calculated with the VDI-Atlas formula are presented in black, while values calculated with the new version of Wengler are shown in orange. As it is possible to observe, for stainless-steel pipe for a reduced pressure of 0.1 according to VDI-Heat-Atlas [1], too low values are obtained compared to the measured values, whereas the values taken with the Wengler correlation are more consistent, although not completely accurate. The same can be noted for the values measured using the alcohols 1-hexanol and 1-pentanol with stainless-steel, although the difference between the two is greater.

Table 5.8: Comparison on the influence of the material respect to the copper according to VDI-2006 [14], VDI-2010 [1] and Wengler [31].

substance	n-pentane C <sub>5</sub> H <sub>12</sub>		1-hexanol C <sub>6</sub> H <sub>14</sub> O		1-pentanol C <sub>5</sub> H <sub>12</sub> O	
	Cu	st. steel	Cu	st. steel	Cu	st. steel
$\alpha_{0,calc,p^*=0.1}$ (Gorenflo-2006)	2947	1424 1823	254 4	1229 1574	2659	1285 1645
$\alpha_{0,calc,p^*=0.1}$ (Gorenflo-2010)	3078	1487 1905	282 9	1367 1751	3019	1459 1868
$\alpha_{0,calc,p^*=0.03}$ (Gorenflo-2006)	1684	814 1033	152 0	627 803	1520	734 932
$\alpha_{0exp,p^*=0.03}$	2731	1209	236 3	1779	2655	1979
$\alpha_{0exp,p^*=0.1}$	4313	2239	463 0	3485	5201	3936

This behavior shown in Table 5.8 can also be explained graphically with Fig. 5.23 in which the comparison of the experimentally measured data with the smooth copper and stainless-steel tube with the n-pentane substance and those calculated using the correlation according to VDI-Heat-Atlas and Wengler respectively was reported. As can be seen from the graph, the line referred to Wengler is closer to the measured

experimental values, so it fits better the values obtained in the laboratory. At the University of Kassel, researchers and students are currently working for trying to confirm empirically this assumption, using different materials to achieve a better correlation that could consider the use of a different material than copper. They are furthermore studying the effects of the presence of a material on the surface since this can affect the nucleation behavior of the surface by deactivating some cavities, by providing new nucleation sites and by changing the wettability of the surface.

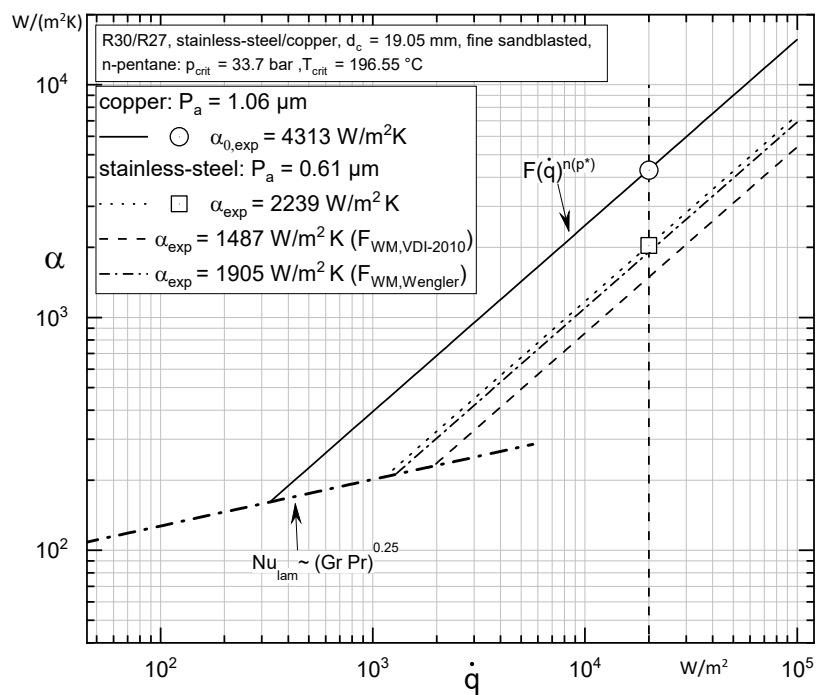


Figure 5.23: Influence of the heater material according to VDI-Atlas (2010) and Wengler (2018) for copper and stainless-steel tubes (graph created using Origin 2016).



## 6. SUMMARY AND OUTLOOK

Even if relatively, little is known about the quantitative effects of the surface properties, the micro and the macrostructure, of the heating wall, it is possible to draw some conclusions from the obtained results, trying to improve the correlations currently available for the calculation of the heat transfer coefficient in nucleate boiling:

- $\alpha$  augments strongly with increasing heat flux and reduced pressure in the regime of nucleate boiling, and the results at constant pressures can be described by straight lines with  $\alpha \approx q^n$  which slopes decreasing with rising pressure. For copper pipe values, after approximately a heat flux value of 20000 W/m<sup>2</sup>, instead of having a reduction in slope, the lines don't change their inclination, so with the stainless-steel pipe we are closer to the critical point as it is possible to observe with change in slope. For plain tubes, the increase of  $\alpha$  with  $q$  is more pronounced at low pressures, but the effect decreases more rapidly when the pressure is raised. That means that the differences existing between plain and finned tubes in the relative increases of the heat transfer coefficient with increasing heat flux, tend to vanish at high normalized saturation pressure.
- Copper has a higher thermal conductivity than stainless-steel, which means that it will have a lower surface temperature, as the heat from the heating tube will be better transferred to the liquid, whereas with the stainless-steel tube will be more difficult to transfer heat, resulting in a higher surface temperature. Thus, the copper tube will result in less overheating than the stainless-steel tube. In addition, the pipe wall overheating increases with the rise of the heat flux density. The superheating  $\Delta T$  of the finned tube is diminished below the plain tube, particularly at the bottom of the tube. This heat transfer enhancement is caused by the nucleation sites getting activated mainly by the superheat near the bases of the fins being somewhat higher than on the rest of the fin surface, and by the bubbles sliding upwards between the fins. With smooth tubes the bubbles find more difficult to go up the tube, when we have finned tubes the bubbles stay less time in the area below being driven by the geometry of the tube

upwards thus increasing the convective exchange of fluid around the surface. This effect is most evident for higher heat flux densities, thus demonstrating that the relative effect of convection on the enhancement is highest when a comparatively small number of big bubbles is generated.

- The onset of nucleate boiling for the alcohol 1-pentanol, for the same reduced pressure, is earlier than in the case of 1-hexanol because the saturation curve referred to 1-pentanol is shifted to the left compared to the 1-hexanol curve.
- For an increase in pressure, the tube wall overheating  $\Delta T$  required to activate the nucleation sites decreases, which results in a decrease in the critical bubble radius. More nucleation sites are activated,  $\alpha$  increases. For a sufficiently high heat flux density, the pressure dependence is negligible, the overheating is large enough and all nucleation sites are already activated. Considering the slope as a function of the reduced pressure, the old correlation according to VDI-2006 fixes better the measured values, except for the case with n-pentane for the copper tube at the reduced pressure equal to 0.03, for the finned tube with 1-hexanol and for the finned tube at the reduced pressure of 0.007 with 1-pentanol in which the new correlation turns out to be better.
- The measured points of the heat transfer coefficient as a function of the reduced pressure are more in agreement with the old VDI-2006 correlation with n-pentane for all the cases of stainless-steel and copper smooth tubes and finned stainless-steel tube, while for the two alcohols the VDI-2010 correlation is in greater agreement.
- In the nucleate boiling zone, it is possible to observe a greater agreement with respect to the values calculated according to VDI-Heat-Atlas with the experimental values obtained using the copper smooth pipe compared to the stainless steel one. Furthermore, there is a smaller distance between the experimental values and the calculated ones due to the different value of roughness and also a different behavior between the substance n-pentane compared to the two alcohols considered (1-hexanol and 1-pentanol). In addition, it is possible to see that for higher pressures the difference between the

calculated and measured values tends to get thinner, since the influence of the roughness tends to decrease with increasing heat flux and reduced pressure [32].

- Regarding the finned tube the measurement results show that the initiation of nucleate boiling is promote for lower superheats. Finned tubes are used in shell and tube evaporators of refrigerating machines and heat pumps at comparatively low saturation pressures. In this pressure range, the heat flux  $q$  and the heat transfer coefficient  $\alpha$  are higher than with pool boiling on the outside of smooth tubes, at the same superheat  $\Delta T$  of the heating surface, while the relative dependence of  $\alpha$  from  $q$  and from the saturation pressure  $p_{sat}$  is lower.
- Tubes with external fins transfer heat more efficiently than smooth tube because an increase in  $\alpha$  can be derived to the great roughness at the crest of the fins and to the additional convection caused by the bubbles that rise along the flanks of the fins. The increase in surface area exerts less and less influence as the heat flux increases because after a certain time there is the formation of a vapor layer composed of bubbles and so the influence of the macrostructure on the heat transfer coefficient decreases.
- The Slipcevic correlation better approximates the values obtained for the stainless-steel finned tube than the more current versions according to VDI-Heat-Atlas [1] used as calculated method in this work. It is therefore possible to assume that Slipcevic's correlation is better suited to certain substances than others (in this case the hydrocarbon n-pentane compared to alcohol 1-hexanol).
- In similar conditions the heat transfer on the copper tube is higher than the one on the stainless-steel tubes and the influence of the wall material is lower than the one postulated by VDI-Heat-Atlas, so the recently developed correlation by Wengler [31] shall be introduced into VDI in future.

Based on the conclusions obtained, the parts of the predictive methods which should be improved more are the influence of the structure and material of the heating wall, reconsidering (especially for the case of finned tubes) old equations from past editions of VDI (1977), from which Slipcevic's theory is based, with also a conspicuous comparison with data from the literature. The difficulty in finding a theory that could fit

the different parameters and so the complexity of the results lies from both solid surface effects and liquid characteristics because real solid surfaces are usually heterogeneous, anisotropic, rough and are affected by adsorption and oxidation [33]. Thus, the effect of surface roughness on heat transfer must be described by a modified VDI-Atlas correlation, because evidently the single roughness parameter is insufficient to characterize the different surface textures and to define the cavity size distribution, as Stephan has pointed out already in his pioneering work of 1963 [16]. Furthermore, it is necessary to carry out multiple measurements with different refrigerants, since after the EU-F-gas regulation we are increasingly moving towards natural refrigerants such as HC refrigerants and inorganic refrigerants, while in most of the writings present in the literature available today, refrigerants based on halogen molecules have been used.



## 7. REFERENCES

- [1] Gorenflo D., Kenning D., «Pool Boiling», VDI-Heat Atlas, University of Paderborn, Paderborn (Germany), Brunel and Oxford University, UK., Springer Verlag Berlin Heidelberg, 11th edition, 2010, p. Part Hab. 2.
- [2] Zimmermann F. Slipcevic B., «Heat transfer coefficients at bubble boiling of refrigerants on individual finned tubes», Magazine klima kalte heater, pp. Vol. 3, pag 115-120., 1982.
- [3] Luke A., «Heat transfer evaporation on micro- and macro- structured tubes,» 2018.
- [4] Pil-Hyun Yoon, Jinhee Jeong, Yong-Tae Kang, «Boiling hysteresis at low temperature on enhanced tubes», International Journal of Refrigeration, vol. 27, n. 1, pp. 4-9, 2004.
- [5] Collier J., «Boiling and Evaporation», in Heat Exchanger Design Handbook, Düsseldorf, Washington New York London, Verlag des Vereins Deutscher Ingenieure, Hemisphere Publishing Corporation , 1983, pp. 2.7.1-2.7.8.
- [6] Deeb M., «Einfluss der Oberflächenbearbeitung durch Sandstrahlen auf die Keimbildung in gesättigten Flüssigkeiten», University of Kassel: Masterarbeit, 2017.
- [7] Maximilian Naß B. Sc., «Der Einfluss der mikro- und makrostrukturierten edelstahlheizflächen auf den Wärmeübergang beim», University of Kassel: Masterarbeit, 2023.
- [8] Baehr H. D., Stephan K., «Heat and mass transfer», Springer Verlag, 10th edition, Berlin, Heidelberg, New York, 2016.
- [9] Stephan K., «Fundamentals of steam bubbles», in VDI Heat Atlas, University of Stuttgart, Springer-Verlag, 11th edition , 2010, p. Hab. 1.
- [10] Fritz W., «Calculation of the maximum volume of vapor bubbles», Physical Journal, pp. 379-384, 1935.
- [11] DIN EN ISO 4287, «Geometrical Product Specification (GPS) - Surface finish: profile method - designations and surface parameters of surface texture», Beuth Verlag GmbH, Berlin, 2010.
- [12] Gorenflo D., «Influence of thermophysical properties on pool boiling heat transfer of refrigerants», International Journal of Refrigeration, vol. 27, n. 5, pp. 492-502, 2004.
- [13] Stephan K., Preusser P, «Heat transfer and maximum heat flow density during container boiling of binary and ternary liquid mixture», Journal Chemie Ingenieur Technik, vol 5, 1978.
- [14] Gorenflo D., Kenning D.,«Pool boiling», in VDI Heat Atlas, University of Paderborn, Paderborn (Germany), Brunel and Oxford University, UK., Springer-Verlag 10th edition, Berlin Heidelberg, 2006, Part. Hab. 2.
- [15] Siebert M., «Untersuchung zum Einfluß des Wandmaterials und des Rohrdurchmessers auf den Wärmeübergang von horizontalen Rohren an siedende Flüssigkeiten», PhD thesis, University (TH) of Karlsruhe, 1987.
- [16] Stephan K., «Wärme- und Stoffübertragung», in Mechanismus und Modellgesetz des Wärmeübergangs bei der Blasenverdampfung, Springer Verlag, 1963, pp. 11, 775-784.
- [17] Cooper M., «Heat flow rates in saturated nucleate pool boiling- a wide ranging examination using reduced properties», p. 158-202, Department of Engineering

Science, Oxford University, England, 1984.

- [18] J. Jones, J. P. McHale, S. Garimella, «The Influence of Surface Roughness on Nucleate Pool Boiling Heat Transfer», Birck and NCN Publications, vol. 131, n. Paper 480, pp. 1-14, 2009.
- [19] Luke A., Kruck O., «Heat transfer Measurements of R134a and Propane Boiling at Evaporator Tubes with plain and enhanced finned surface», Purdue e-Pubs, pp. 1-8, 2008, Leibniz University of Hannover, Institute of Thermodynamics, Hannover, Germany.
- [20] Luke A., «Heat transfer mechanisms of R134a and propane boiling on horizontal steel tubes with enhanced surface structures», Proc. 14th Int. Heat Transfer Conf., Washington (USA), n. IHTC14-22887, pp. 553-561, 2010.
- [21] Koch D., «Einfluss der Oberflächenrauheit auf den Wärmeübergang beim Sieden von Propan und R134a», University of Kassel, Masterarbeit, 2014.
- [22] Gorenflo D. J. Goetz, K. Birra, «Vorschlag für eine Standard-Apparatur zur Messung des Wärmeübergangs beim Blasensieden», Wärme- und Stoffübertragung, Springer-Verlag 16, pp. 69-78, 1982.
- [23] Gorenflo D., Faith W., «Heat transfer in pool boiling on the outside of finned tubes at high saturation pressures», In. Congr. Refrig., vol.B, P. 955-60, Wien, 1987.
- [24] Span R., «Material properties of important pure fluids», in VDI-Heat-Atlas, Berlin Heidelberg, Springer-Verlag, 2013, Part Hab.1.
- [25] Mostafa Ghiaasiaan S., «Two- phase flow, boiling and condensation in conventional and miniature systems», Georgia institute of Technology: Cambridge University Press., 2007.
- [26] Luke A., Deeb M., Margraf E., «Influence of finned and porous structures in nucleate boiling of Hydrocarbons», 2018.
- [27] Hübner P., Gorenflo D., Luke A., «Circumferential temperature distributions on plain and finned tubes in pool boiling», Paderborn, Germany, 2008.
- [28] Gorenflo D., «Wärmeübergang bei Blasensieden, Filmsieden und einphasiger freier Konvektion in einem großen Druckbereich», Prof. Dr.-Ing. Rudolf Plank, no 22, Karlsruhe, 1977.
- [29] Bujok P., «Zum Wärmeübergang beim Blasensieden an eng berippten Stahlrohren», Doctor Engineer dissertation, University of Kassel, 2015.
- [30] Niklas Buchholz M. Sc., «Analyse mikrostrukturierter Heizflächen hinsichtlich der Blasenbildung bei der Verdampfung», Dissertation to obtain the academic degree doctor of Engineering, University of Kassel, 2023.
- [31] Wengler C., «Einfluss des Heizwandmaterials auf den Wärmeübergang beim Blasensieden», Doctor of Engineering dissertation, University of Kassel, 2018.
- [32] Luke A., «Pool boiling heat transfer from horizontal tubes with different surface roughness», International Journal of Refrigeration, vol. 20, n. 8, pp. 561-574, 1997.
- [33] Bräuer H., Mayinger F., «Onset of nucleate boiling and hysteresis effects under forced convection and pool boiling».

## 8. APPENDIX

Table 8.1: Heat transfer measurements on the smooth stainless-steel tube with n-pentane.

Measurement MR394 R30/ stainless-steel	$\dot{q}$ [W/m <sup>2</sup> ]	$\alpha$ [W/m <sup>2</sup> K]	$\Delta T$ [K]	Measurement MR395 R30/ stainless-steel	$\dot{q}$ [W/m <sup>2</sup> ]	$\alpha$ [W/m <sup>2</sup> K]	$\Delta T$ [K]
$p^* = 0.1$	100026	4080	24.52	$p^* = 0.05$	70032	2873	24.38
$\alpha_0 = 2239 \text{ W/m}^2\text{K}$	70005	3448	20.30	$\alpha_0 = 1609 \text{ W/m}^2\text{K}$	50020	2481	20.16
$n = 0.672$	50002	3019	16.56	$n = 0.723$	20099	1574	12.77
$T_{sat} = 76.56 \text{ }^\circ\text{C}$	19999	2037	9.82	$T_{sat} = 51.84 \text{ }^\circ\text{C}$	10142	1048	9.68
	10000	1443	6.93		5069	584	8.67
	5007	932	5.37		2030	294	6.91
	2005	522	3.84		1002	190	5.26
	1006	308	3.27		502	166	3.03
	501	170	2.95		204	144	1.41
	200	140	1.43		102	133	0.77
	100	127	0.78		49	120	0.41
	52	118	0.44				
Measurement MR398 R30/ stainless-steel	$\dot{q}$ [W/m <sup>2</sup> ]	$\alpha$ [W/m <sup>2</sup> K]	$\Delta T$ [K]				
$p^* = 0.03$	69993	2537	27.59				
$\alpha_0 = 1351 \text{ W/m}^2\text{K}$	50008	2150	23.26				
$n = 0.841$	19990	1279	15.63				
$T_{sat} = 36 \text{ }^\circ\text{C}$	10008	792	12.64				
	8011	652	12.28				
	5001	416	12.02				
	2004	191	10.52				
	1017	168	6.07				
	508	152	3.34				
	201	145	1.38				
	100	139	0.71				
	54	141	0.38				

Table 8.2: Heat transfer measurements on the smooth stainless-steel tube with 1-hexanol.

Measurement MR455 R30/ stainless-steel	$\dot{q}$ [W/m <sup>2</sup> ]	$\alpha$ [W/m <sup>2</sup> K]	$\Delta T$ [K]	Measurement MR456 R30/ stainless-steel	$\dot{q}$ [W/m <sup>2</sup> ]	$\alpha$ [W/m <sup>2</sup> K]	$\Delta T$ [K]
$p^* = 0.01$	69980	2753	25.42	$p^* = 0.007$	70033	2116	33.09
$\alpha_0 = 1139 \text{ W/m}^2\text{K}$	50373	2119	23.77	$\alpha_0 = 1626 \text{ W/m}^2\text{K}$	50111	1668	30.09
$n = 0.672$	20063	1119	17.93	$n = 0.757$	20059	970	20.67
$T_{sat} = 126.51 \text{ }^\circ\text{C}$	10046	758	13.26	$T_{sat} = 117.68 \text{ }^\circ\text{C}$	1006	641	15.70
	8027	659	12.18		8002	544	14.70
	5089	471	10.81		5022	348	14.43
	2017	185	10.90		2032	178	11.41
	1008	187	5.39		1010	181	5.57
	536	165	3.25		502	155	3.25
	205	136	1.51		203	132	1.54
	106	119	0.89		102	116	0.88
					55	105	0.52

Table 8.3: Heat transfer measurements on the smooth stainless-steel tube with 1-pentanol.

Measurement MR451 R30/ stainless-steel	$\dot{q}$ [W/m <sup>2</sup> ]	$\alpha$ [W/m <sup>2</sup> K]	$\Delta T$ [K]	Measurement MR453 R30/ stainless-steel	$\dot{q}$ [W/m <sup>2</sup> ]	$\alpha$ [W/m <sup>2</sup> K]	$\Delta T$ [K]
$p^* = 0.01$	69956	2575	27.17	$p^* = 0.007$	69896	2319	30.14
$\alpha_0 = 1287 \text{ W/m}^2\text{K}$	49923	2029	24.60	$\alpha_0 = 1143 \text{ W/m}^2\text{K}$	49890	1853	26.92
$n = 0.687$	20033	1200	16.70	$n = 0.613$	20004	1130	17.70
$T_{sat} = 110.99 \text{ }^\circ\text{C}$	10055	853	11.78	$T_{sat} = 102.17 \text{ }^\circ\text{C}$	10052	760	13.23
	5043	535	9.42		8009	661	12.12
	2003	250	8.03		4992	480	10.39
	1003	172	5.85		2038	225	9.05
	502	167	3.01		1000	162	6.17
	202	131	1.54		504	156	3.23
	106	119	0.89		207	133	1.55
	51	105	0.48		105	118	0.89
					53	106	0.50

Table 8.4: Heat transfer measurements on the smooth copper tube with n-pentane.

Measurement MR467 R27/ copper	$\dot{q}$ [W/m <sup>2</sup> ]	$\alpha$ [W/m <sup>2</sup> K]	$\Delta T$ [K]	Measurement MR468 R27/ copper	$\dot{q}$ [W/m <sup>2</sup> ]	$\alpha$ [W/m <sup>2</sup> K]	$\Delta T$ [K]
$p^* = 0.1$	100076	15868	6.31	$p^* = 0.05$	100061	12080	8.28
$\alpha_0 = 4245 \text{ W/m}^2\text{K}$	70257	11741	5.98	$\alpha_0 = 3415 \text{ W/m}^2\text{K}$	70065	8805	7.96
$n = 0.639$	50172	8905	5.63	$n = 0.734$	50093	6594	7.60
$T_{sat} = 76.56 \text{ }^\circ\text{C}$	20058	4288	4.68	$T_{sat} = 51.84 \text{ }^\circ\text{C}$	20127	3230	6.23
	10020	2693	3.72		10077	2098	4.80
	8032	2356	3.41		8060	1830	4.40
	5020	1772	2.83		5038	1279	3,94
	504	221	2.28		2005	624	3.21
	204	178	1.15		511	227	2.25
	102	149	0.69		204	197	1.04
	52	118	0.44		100	173	0.58
Measurement MR469 R27/ copper	$\dot{q}$ [W/m <sup>2</sup> ]	$\alpha$ [W/m <sup>2</sup> K]	$\Delta T$ [K]				
$p^* = 0.03$	69951	7788	8.98				
$\alpha_0 = 2747 \text{ W/m}^2\text{K}$	49894	5777	8.64				
$n = 0.851$	20025	2712	7.38				
$T_{sat} = 36 \text{ }^\circ\text{C}$	10005	1557	6.43				
	7992	1270	6.29				
	4995	830	6.02				
	1010	268	3.77				
	507	239	2.12				
	205	205	1.00				
	101	184	0.55				
	49	165	0.30				

Table 8.5: Heat transfer measurements on the smooth copper tube with 1-hexanol.

Measurement MR463 R27/ copper	$\dot{q}$ [W/m <sup>2</sup> ]	$\alpha$ [W/m <sup>2</sup> K]	$\Delta T$ [K]	Measurement MR465 R27/ copper	$\dot{q}$ [W/m <sup>2</sup> ]	$\alpha$ [W/m <sup>2</sup> K]	$\Delta T$ [K]
$p^* = 0.01$	99993	6083	16.44	$p^* = 0.007$	99837	4873	20.49
$\alpha_0 = 1652 \text{ W/m}^2\text{K}$	70027	4285	16.34	$\alpha_0 = 1712 \text{ W/m}^2\text{K}$	70129	3642	19.26
$n = 0.734$	50166	3183	15.76	$n = 0.744$	50055	2869	17.45
$T_{sat} = 126.51 \text{ }^\circ\text{C}$	20086	1699	11.82	$T_{sat} = 117.68 \text{ }^\circ\text{C}$	20048	1524	13.15
	10258	1036	9.90		10000	887	11.28
	8027	841	9.55		8005	804	9.95
	5011	578	8.67		5007	683	7.33
	2002	310	6.46		2008	298	6.74
	988	260	3.80		1006	244	4.12
	500	228	2.19		497	216	2.30
	205	194	1.06		203	183	1.11
	99	172	0.58		103	160	0.64
	50	154	0.33		51	138	0.37

Table 8.6: Heat transfer measurements on the smooth copper tube with 1-pentanol.

Measurement MR459 R27/ Copper	$\dot{q}$ [W/m <sup>2</sup> ]	$\alpha$ [W/m <sup>2</sup> K]	$\Delta T$ [K]	Measurement MR462 R27/ Copper	$\dot{q}$ [W/m <sup>2</sup> ]	$\alpha$ [W/m <sup>2</sup> K]	$\Delta T$ [K]
$p^* = 0.01$	99967	6201	16.12	$p^* = 0.007$	99991	5253	19.04
$\alpha_0 = 1731 \text{ W/m}^2\text{K}$	70076	4382	15.99	$\alpha_0 = 1607 \text{ W/m}^2\text{K}$	70057	3860	18.15
$n = 0.670$	50076	3281	15.26	$n = 0.723$	50063	3019	16.58
$T_{sat} = 110.99 \text{ }^\circ\text{C}$	20022	1804	11.10	$T_{sat} = 102.17 \text{ }^\circ\text{C}$	20016	1729	11.58
	10015	1036	9.66		10010	943	10.62
	8013	874	9.17		8009	823	9.73
	5011	749	6.69		5009	728	6.89
	2008	367	5.48		2007	465	4.32
	1012	258	3.93		1004	269	3.73
	511	222	2.31		505	215	2.36
	202	183	1.10		208	181	1.15
	109	161	0.68		101	172	0.59
	52	139	0.37		53	137	0.39

Table 8.7: Heat transfer measurements on the finned stainless-steel tube with n-pentane.

Measurement MR378 R29/ stainless-steel	$\dot{q}_c$ [W/m <sup>2</sup> ]	$\alpha_c$ [W/m <sup>2</sup> K]	$\Delta T$ [K]	Measurement MR379 R29/ stainless-steel	$\dot{q}_c$ [W/m <sup>2</sup> ]	$\alpha_c$ [W/m <sup>2</sup> K]	$\Delta T$ [K]
$p^* = 0.1$	100109	4783	20.93	$p^* = 0.05$	100007	4165	24.01
$\alpha_0 = 2334 \text{ W/m}^2\text{K}$	70100	4167	16.82	$\alpha_0 = 1624 \text{ W/m}^2\text{K}$	70031	3585	19.53
$n = 0.686$	50011	3665	13.64	$n = 0.707$	50005	3051	16.39
$T_{sat} = 76.56 \text{ }^\circ\text{C}$	20001	2458	8.14	$T_{sat} = 51.84 \text{ }^\circ\text{C}$	20043	1768	11.33
	10008	1613	6.20		10014	1070	9.36
	8016	1377	5.82		8019	898	8.93
	5008	966	5.19		5012	614	8.16
	2003	467	4.29		2006	288	6.96
	1004	267	3.76		1012	235	4.32
	504	211	2.40		500	205	2.44
	199	177	1.12		202	172	1.17
	101	154	0.66		101	150	0.67
	52	132	0.39		50	130	0.38
Measurement MR380 R29/ stainless steel	$\dot{q}_c$ [W/m <sup>2</sup> ]	$\alpha_c$ [W/m <sup>2</sup> K]	$\Delta T$ [K]				
$p^* = 0.03$	100104	3766	26.58				
$\alpha_0 = 1489 \text{ W/m}^2\text{K}$	70008	3228	21.69				
$n = 0.715$	50013	2742	18.24				
$T_{sat} = 36 \text{ }^\circ\text{C}$	20035	1581	12.67				
	10041	938	10.71				
	8002	774	10.34				
	5025	529	9.49				
	2010	297	6.76				
	1008	235	4.29				
	501	202	2.48				
	203	172	1.18				
	101	152	0.67				
	52	137	0.38				

Table 8.8: Heat transfer measurements on the finned stainless-steel tube with 1-hexanol.

Measurement MR390 R29/ stainless-steel	$\dot{q}_c$ [W/m <sup>2</sup> ]	$\alpha_c$ [W/m <sup>2</sup> K]	$\Delta T$ [K]	Measurement MR456 R29/ stainless-steel	$\dot{q}_c$ [W/m <sup>2</sup> ]	$\alpha_c$ [W/m <sup>2</sup> K]	$\Delta T$ [K]
$p^* = 0.01$	99856	3437	29.05	$p^* = 0.007$	99980	3247	29.05
$\alpha_0 = 1641 \text{ W/m}^2\text{K}$	70063	2928	23.93	$\alpha_0 = 1365 \text{ W/m}^2\text{K}$	70115	2677	23.93
$n = 0.843$	49942	2513	19.87	$n = 0.881$	50037	2253	19.87
$T_{sat} = 126.51 \text{ }^\circ\text{C}$	20087	1653	12.15	$T_{sat} = 117.68 \text{ }^\circ\text{C}$	20078	1344	12.15
	10021	910	11.01		10012	771	11.01
	5019	513	9.78		5040	397	9.78
	2000	321	6.23		2002	289	6.23
	1005	292	3.45		999	234	3.45
	502	262	1.91		503	200	1.91
	202	247	0.81		202	168	0.81
	99	226	0.44		103	152	0.44
	52	168	0.31		50	139	0.31

Table 8.9: Heat transfer measurements on the finned stainless-steel tube with 1-pentanol.

Measurement MR386 R29/ stainless-steel	$\dot{q}_c$ [W/m <sup>2</sup> ]	$\alpha$ [W/m <sup>2</sup> K]	$\Delta T$ [K]	Measurement MR387 R29/ stainless-steel	$\dot{q}_c$ [W/m <sup>2</sup> ]	$\alpha_c$ [W/m <sup>2</sup> K]	$\Delta T$ [K]
$p^* = 0.01$	100108	3402	29.42	$p^* = 0.007$	100118	3402	31.52
$\alpha_0 = 1597 \text{ W/m}^2\text{K}$	70033	2883	24.29	$\alpha_0 = 1371 \text{ W/m}^2\text{K}$	70034	2883	26.83
$n = 0.806$	50009	2422	20.65	$n = 0.799$	50044	2422	22.52
$T_{sat} = 110.99 \text{ }^\circ\text{C}$	20037	1501	13.35	$T_{sat} = 102.17 \text{ }^\circ\text{C}$	20047	1501	14.67
	10016	878	11.40		10022	878	12.55
	8009	741	10.81		4998	741	11.09
	5028	489	10.28		2013	489	7.22
	2004	297	6.75		1006	297	4.76
	1007	232	4.35		502	232	2.68
	503	195	2.58		201	195	1.27
	202	170	1.19		103	170	0.71
	101	151	0.67		51	151	0.38
	52	138	0.38				

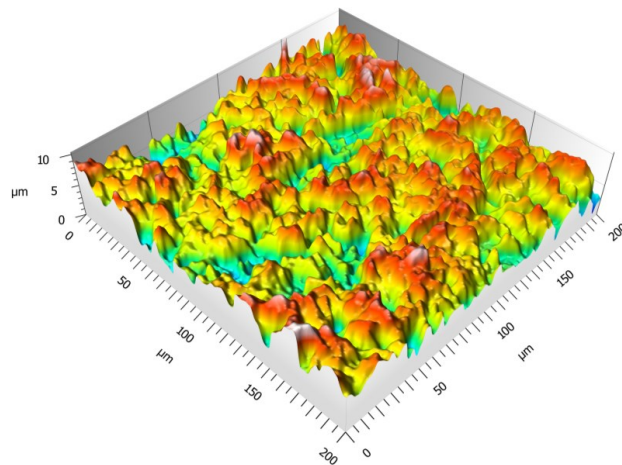


Table 8.10: Parameters of roughness measurement, profile and topography for the copper smooth tube for the third measurement on the radial direction.

Test tube designation	R27			
Heating wall material, Outer diameter	Copper, $d_c=19.05$			
Surface treatment	Fine Sandblasting (EKF220)			
Surface measurement	Non-contact focus variation			
Magnification	50 x			
Lateral resolution	1 $\mu\text{m}$			
Vertical resolution	20 nm			
Contrast	0.98			
Profile	Standard roughness parameters according to DIN EN ISO 4287 [8]			
	$P_a$	$P_q$	$P_p$	$P_t$
Mean	1.16	1.45	3.09	6.93
Max	1.97	2.50	6.79	14.33
Min	0.65	0.86	1.48	3.77
Standard deviation	0.23	0.29	0.79	1.49

13728 measurements runs  
12 measured positions

**Surface topography of the third measurement in the radial direction of the smooth copper tube**



**Two-dimensional profile cross section of the third measurement in the radial direction of the smooth copper tube**

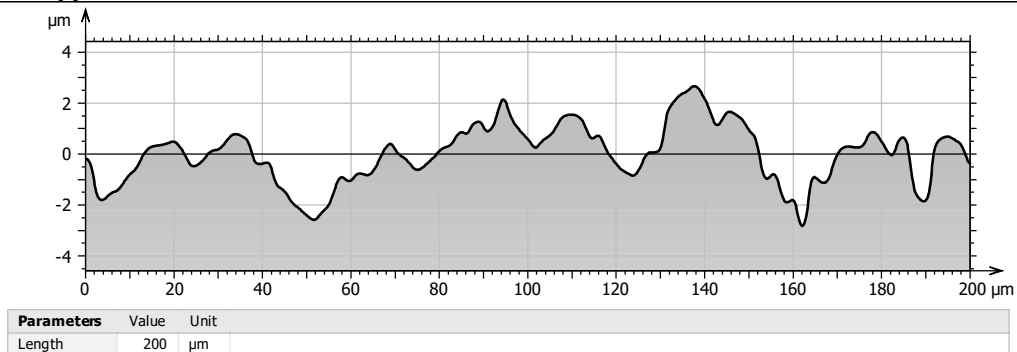
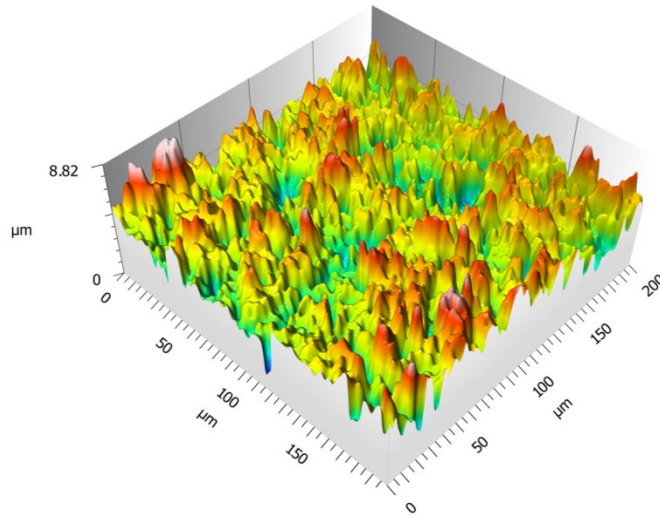


Table 8.11: Parameters of roughness measurement, profile and topography for the stainless-steel tube smooth tube for the sixth measurement on the radial direction.

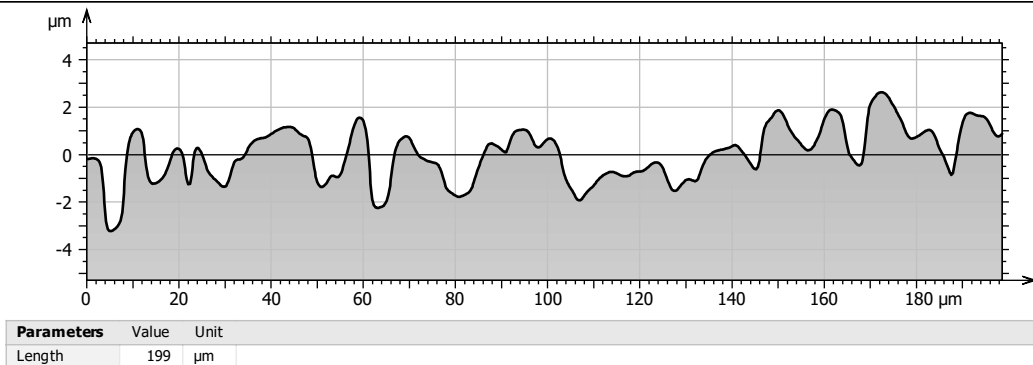
Test tube designation	R30			
Heating wall material, Outer diameter	Stainless-steel, $d_c=19.05$			
Surface treatment	Fine Sandblasting (EKF220)			
Surface measurement	Non-contact focus variation			
Magnification	50 x			
Lateral resolution	1 $\mu\text{m}$			
Vertical resolution	20 nm			
Contrast	0.98			
Profile	Standard roughness parameters according to DIN EN ISO 4287 [8]			
	$P_a$	$P_q$	$P_p$	$P_t$
Mean	0.75	0.95	2.21	4.74
Max	1.31	1.67	5.99	10.12
Min	0.40	0.49	0.92	2.09
Standard deviation	0.16	0.20	0.63	1.12

13728 measurements runs  
12 measured positions

Surface topography of the sixth measurement in the radial direction of the smooth stainless-steel tube



Two-dimensional profile cross section of the sixth measurement in the radial direction of the smooth stainless-steel tube



## Diagrams $\Delta T - \varphi$

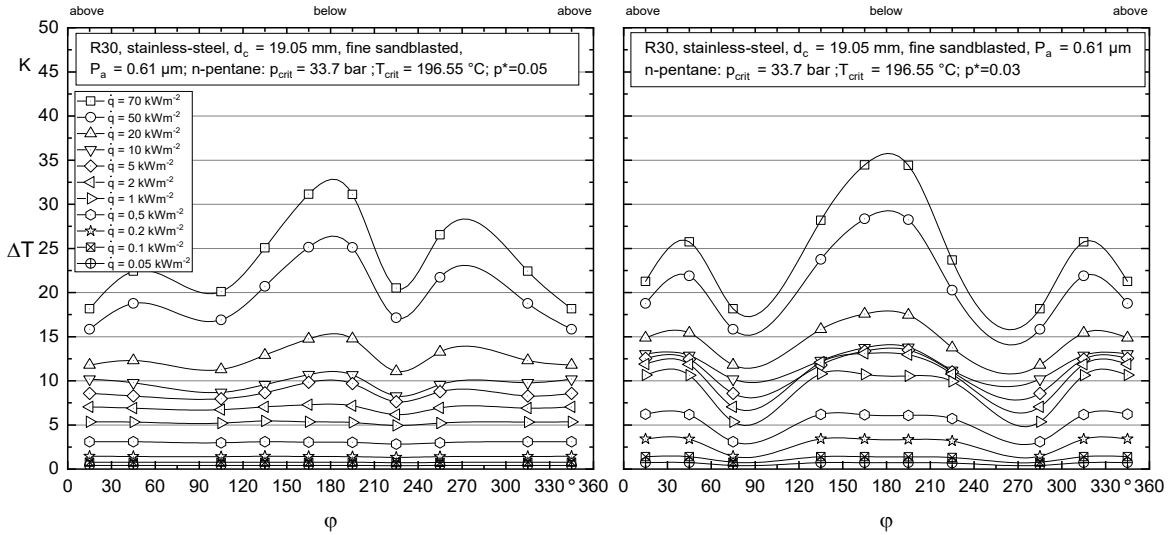


Figure 8.1: Tube wall superheating for the substance *n*-pentane,  $p^* = 0.05$  (left side) and  $p^* = 0.03$  (right side), stainless-steel smooth tube (R30).

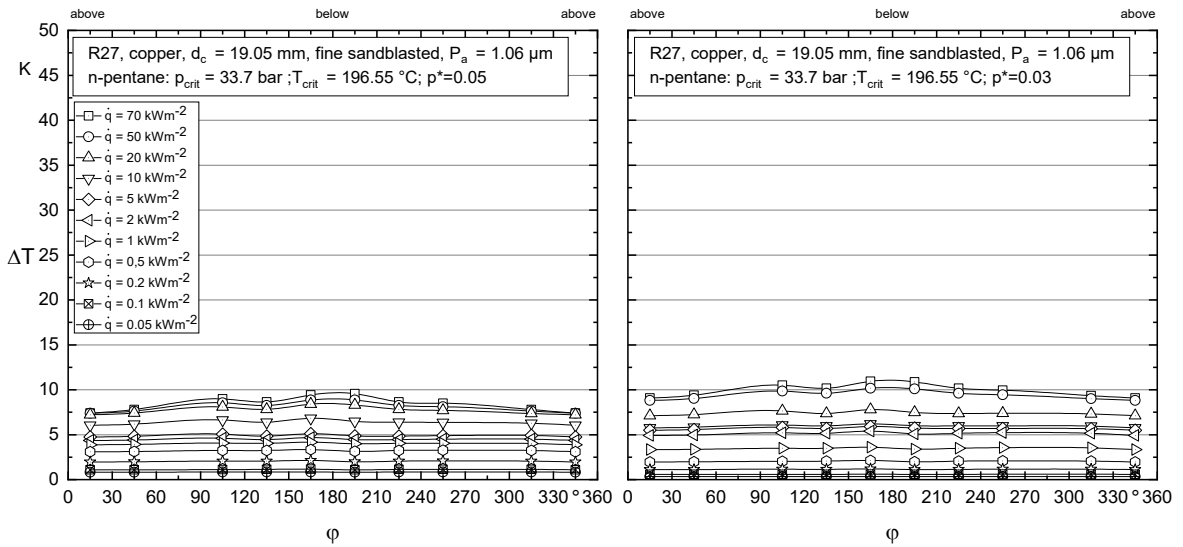


Figure 8.2: Tube wall superheating for the substance *n*-pentane,  $p^* = 0.05$  (left side) and  $p^* = 0.03$  (right side), for copper smooth tube (R27).

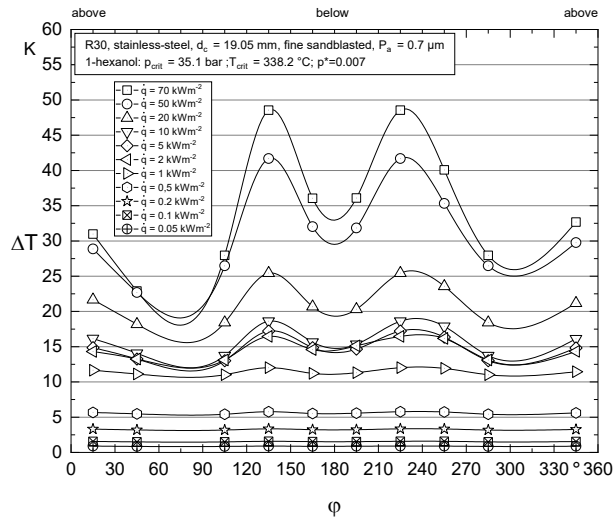


Figure 8.3: Tube wall superheating for the substance 1-hexanol,  $p^* = 0.007$ , for stainless-steel smooth tube (R30).

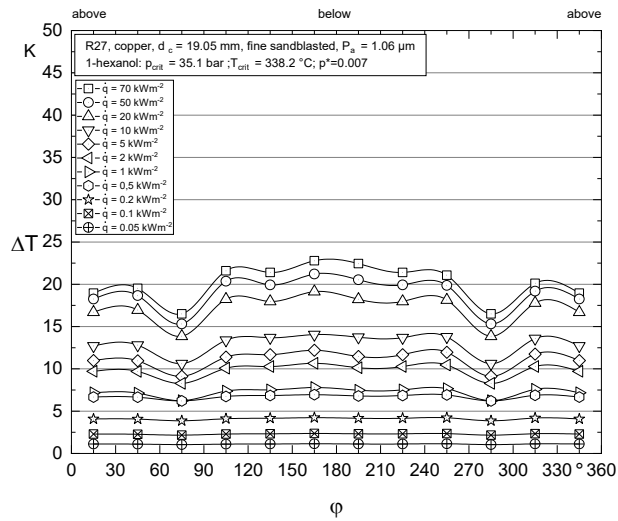


Figure 8.4: Tube wall superheating for the substance 1-hexanol,  $p^* = 0.007$ , for copper smooth tube (R27).

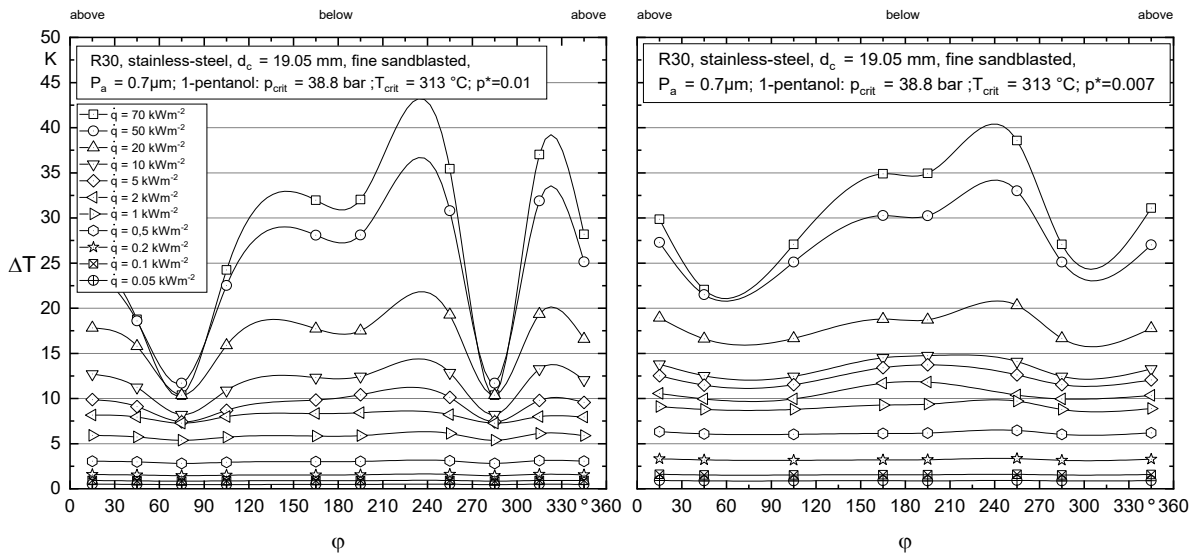


Figure 8.5: Tube wall superheating for the substance 1-pentanol,  $p^* = 0.007$ , for stainless-steel smooth tube (R30).

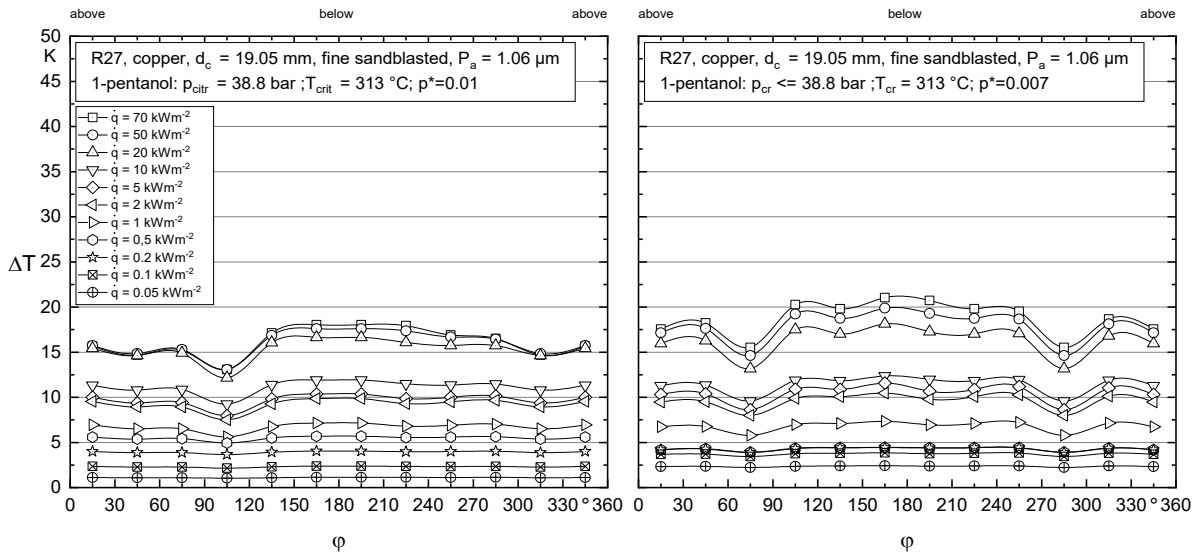


Figure 8.6: Tube wall superheating for the substance 1-pentanol,  $p^* = 0.01$  (left side)  $p^* = 0.007$  (right side), for copper smooth tube (R27).

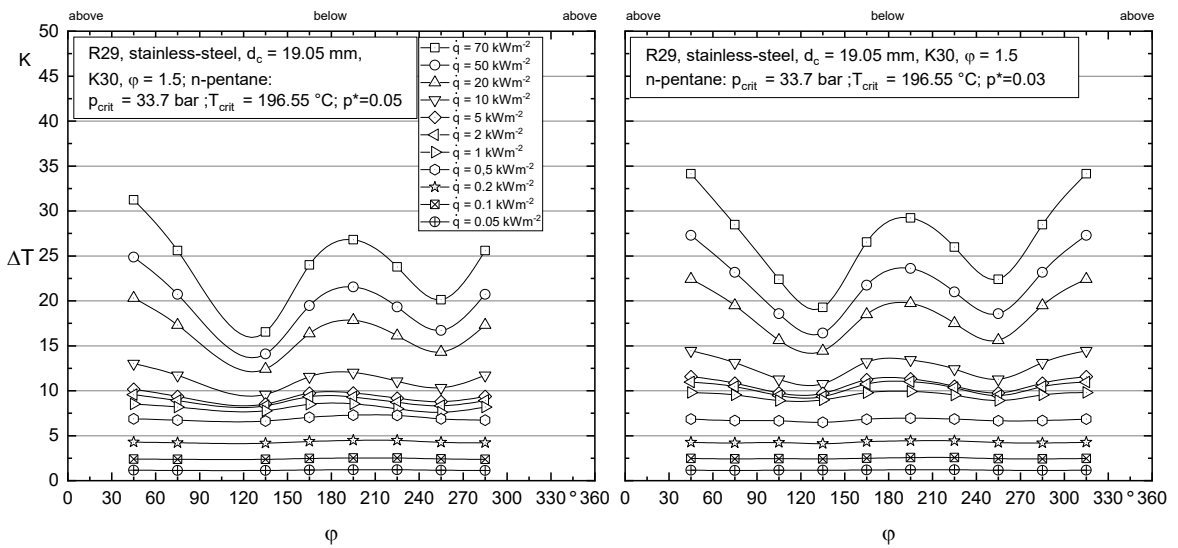


Figure 8.7: Tube wall superheating for the substance *n*-pentane, pressures  $p^* = 0.05$  (left side) and  $p^* = 0.03$  (right side), for stainless-steel finned tube (R29).

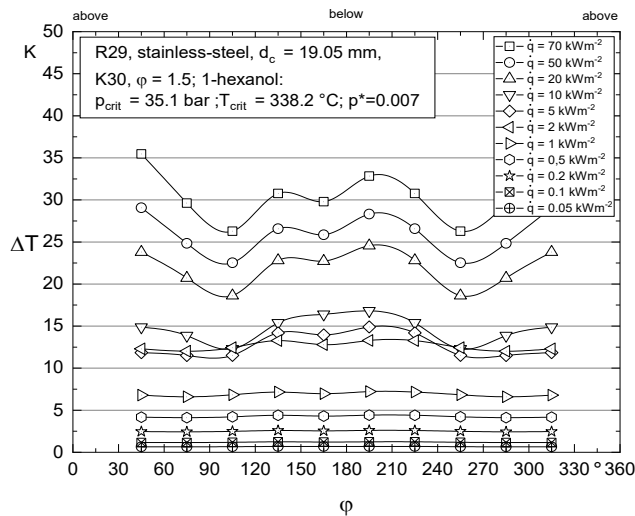


Figure 8.8: Tube wall superheating for the substance *1*-hexanol,  $p^* = 0.007$ , stainless-steel finned tube (R29).

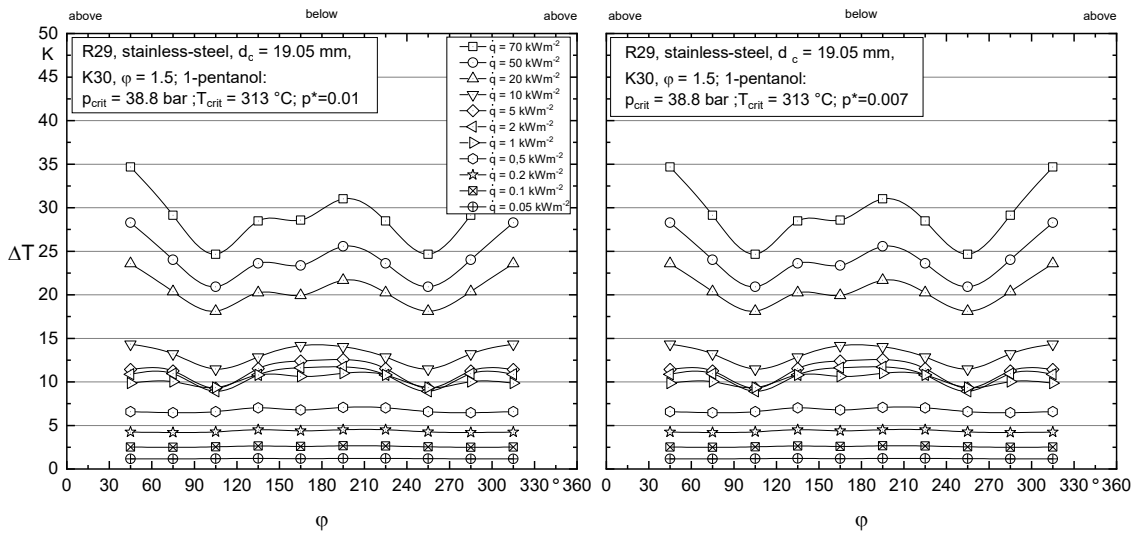


Figure 8.9: Tube wall superheating for the substance 1-pentanol,  $p^* = 0.01$  (left side) and  $p^* = 0.007$  (right side), stainless-steel finned tube (R29).

Table 8.12: Bubble formation when boiling n-pentane on the smooth stainless-steel tube (R30).

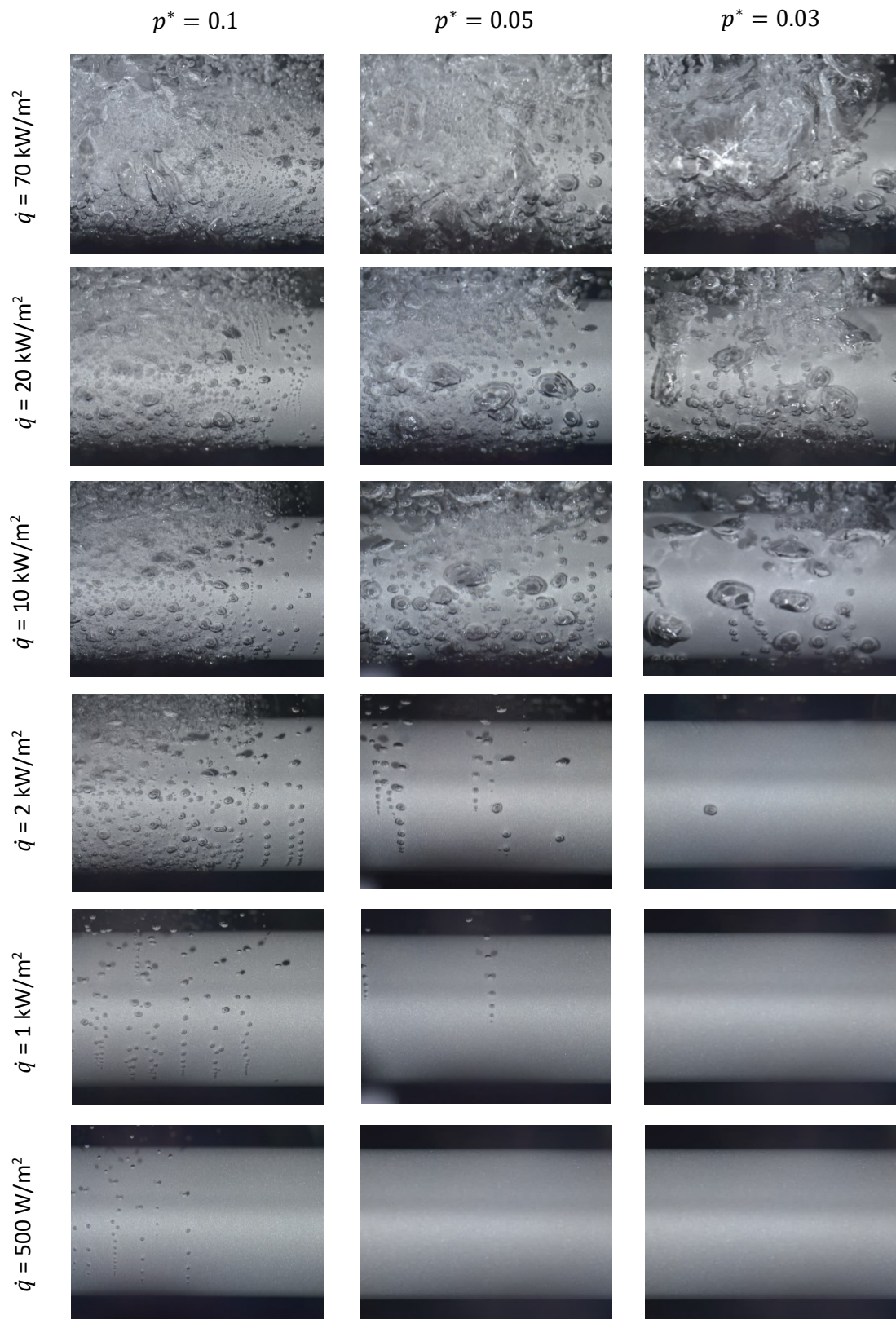




Table 8.13: Bubble formation when boiling 1-hexanol on the smooth stainless-steel tube (R30).

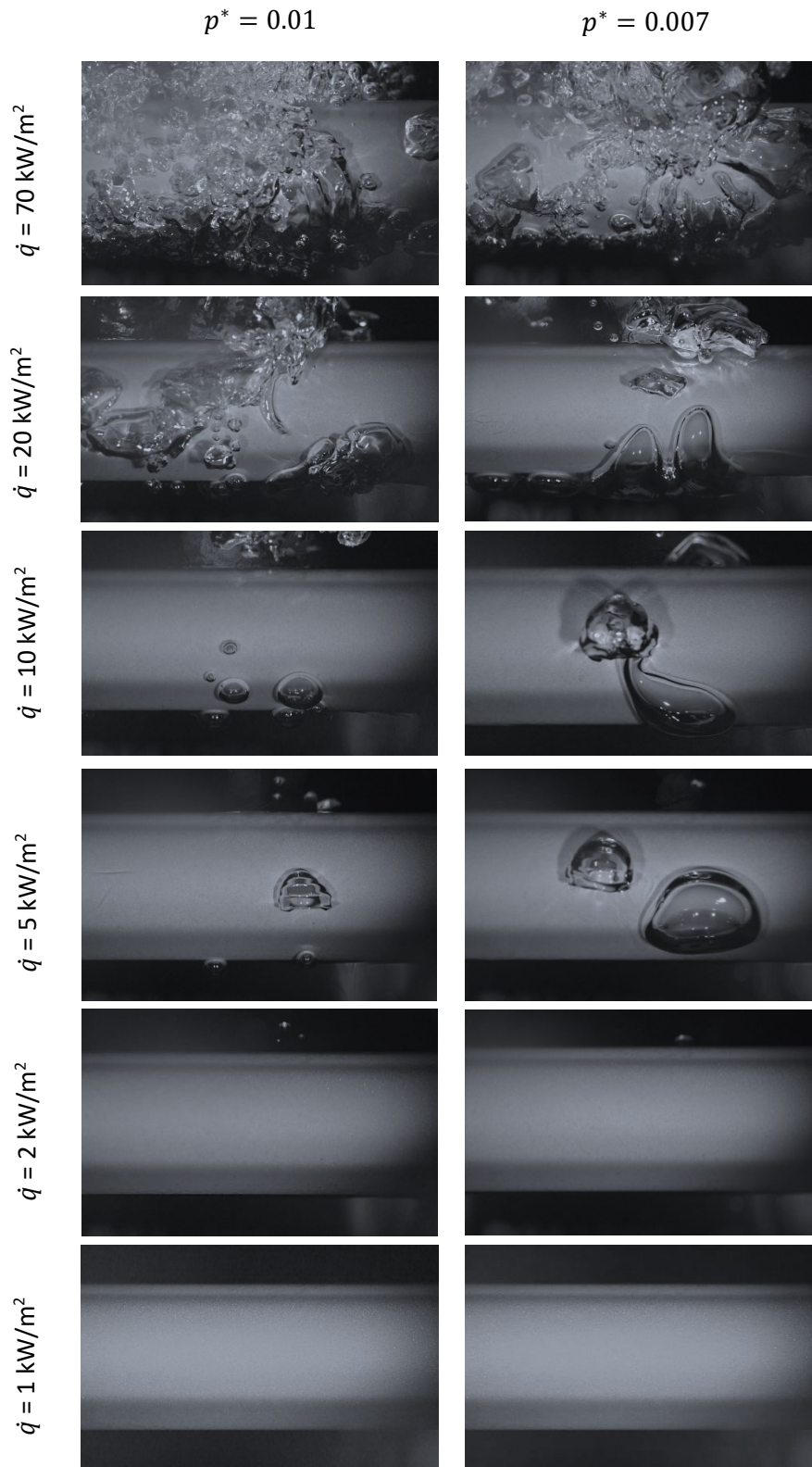


Table 8.14: Bubble formation when boiling 1-pentanol on the smooth stainless-steel tube (R30).

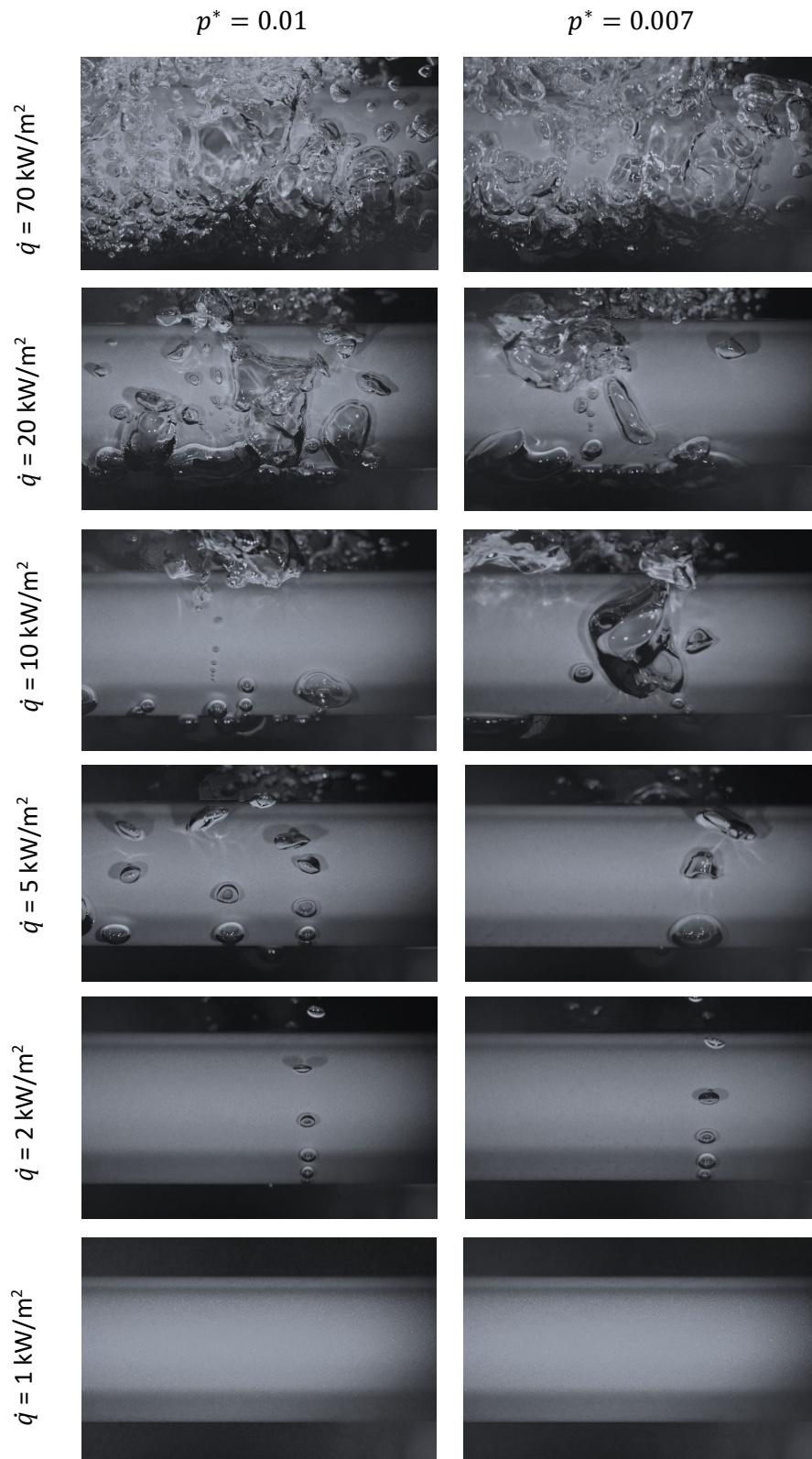


Table 8.15: Bubble formation when boiling n-pentane on the smooth copper tube (R27).











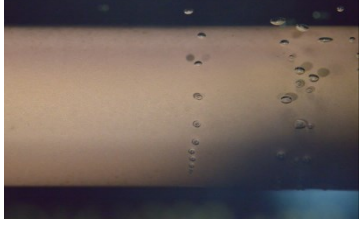

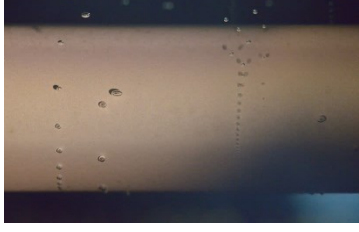
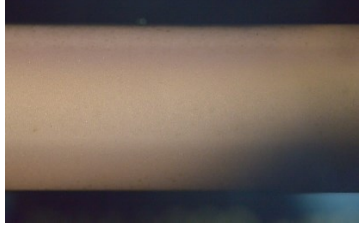
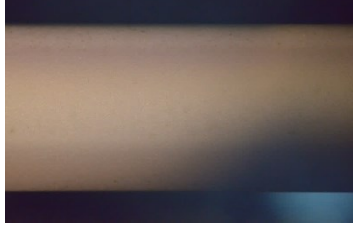
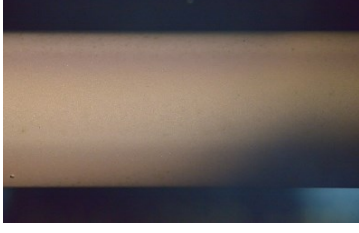
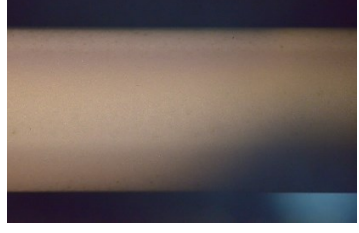
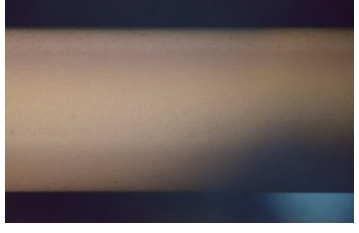
	$p^* = 0.1$	$p^* = 0.05$	$p^* = 0.03$
$\dot{q} = 70 \text{ kW/m}^2$			
$\dot{q} = 20 \text{ kW/m}^2$			
$\dot{q} = 10 \text{ kW/m}^2$			
$\dot{q} = 2 \text{ kW/m}^2$			
$\dot{q} = 1 \text{ kW/m}^2$			
$\dot{q} = 500 \text{ W/m}^2$			

Table 8.16: Bubble formation when boiling 1-hexanol on the smooth copper tube (R27).

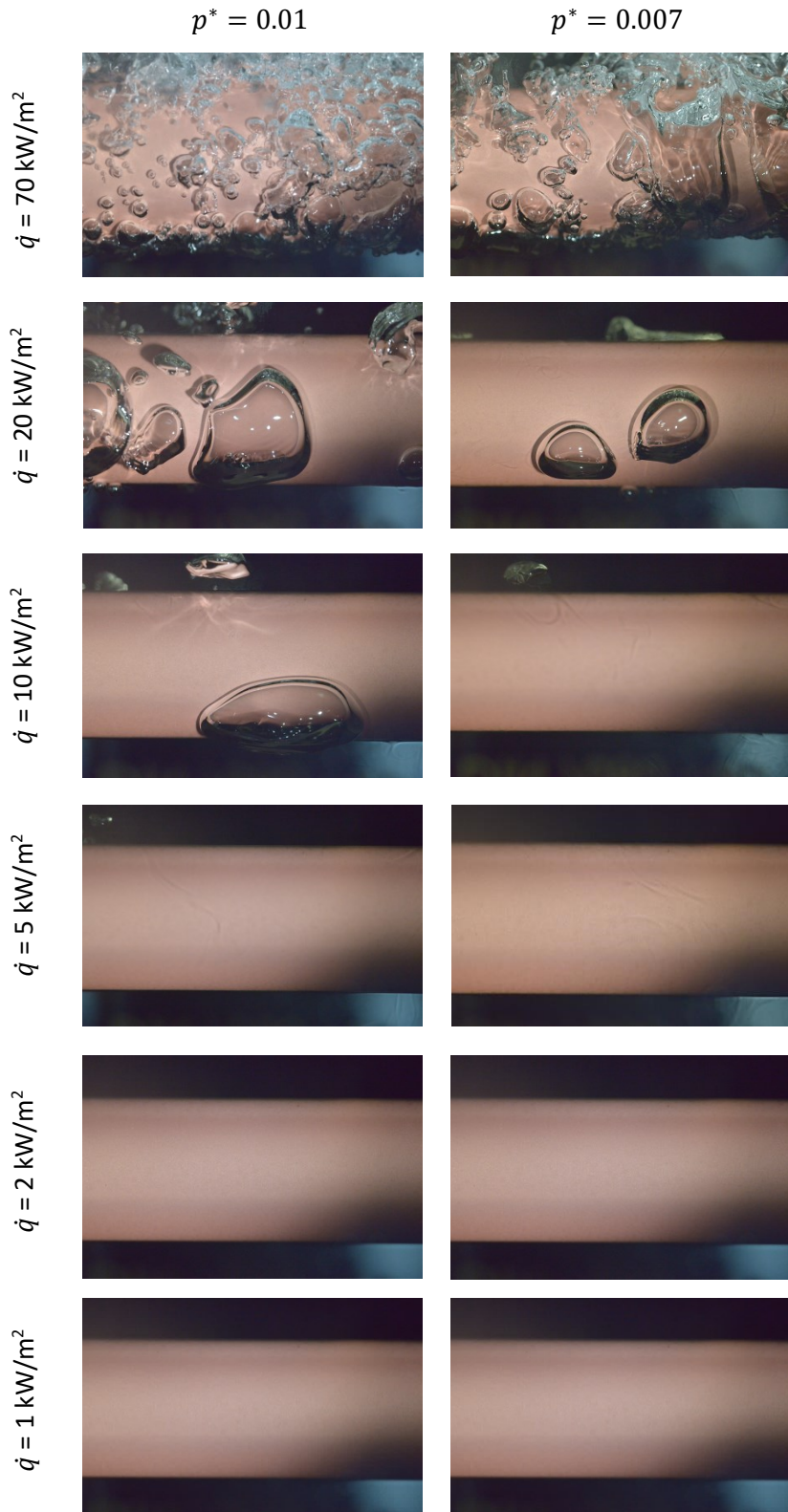


Table 8.17: Bubble formation when boiling 1-pentanol on the smooth copper tube (R27).

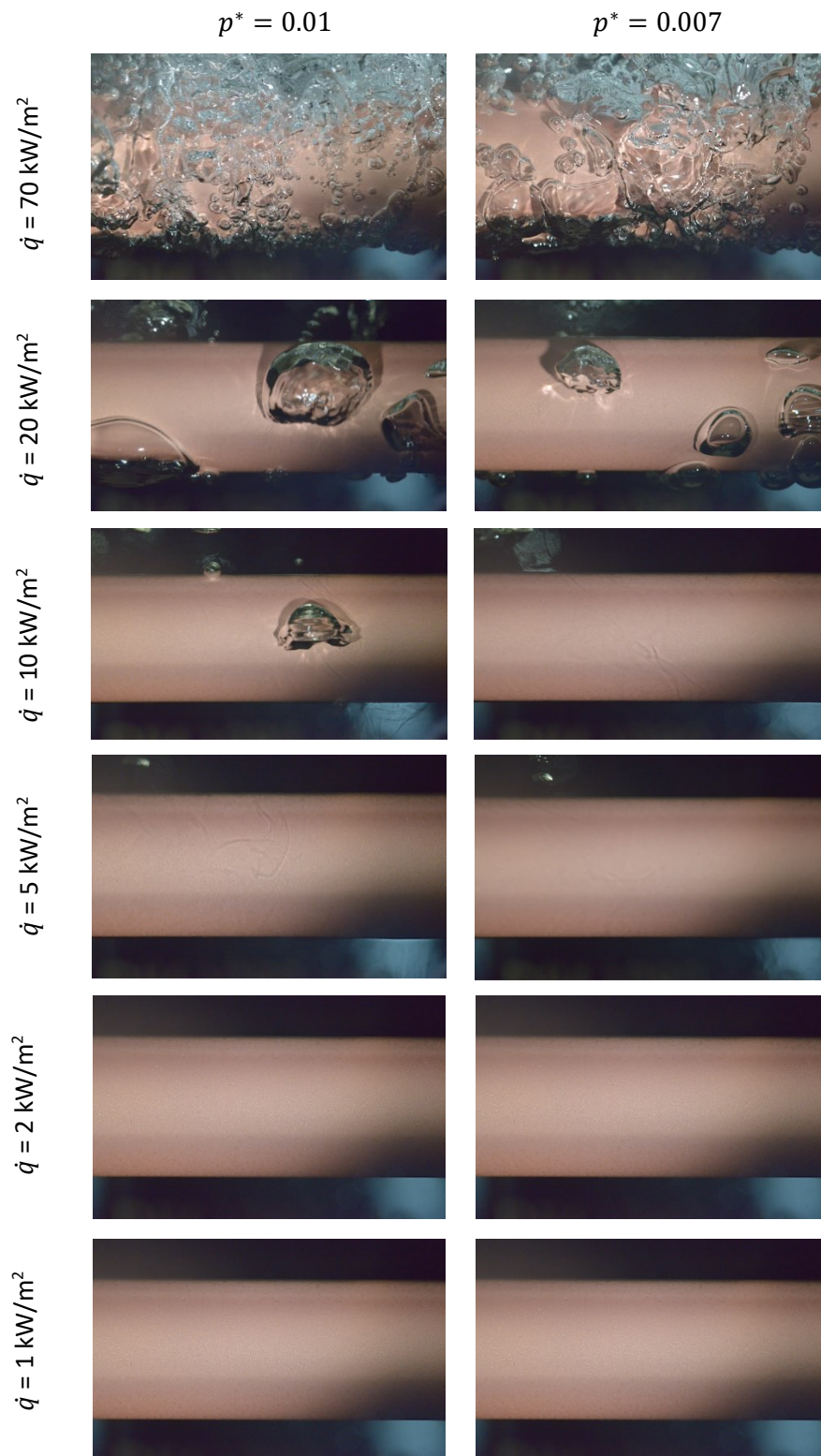


Table 8.18: Bubble formation when boiling n-pentane on the finned stainless-steel tube (R29).

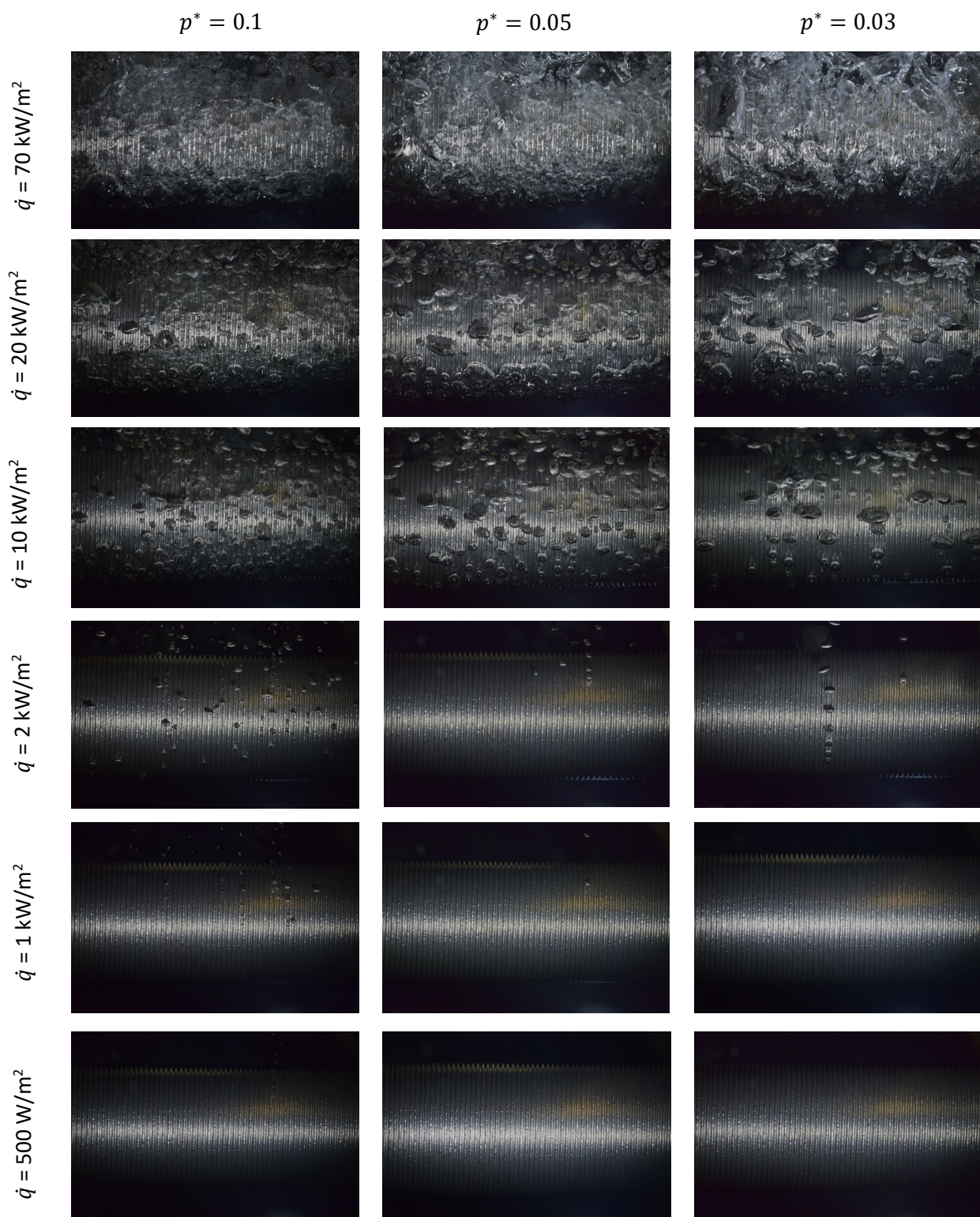


Table 8.19: Bubble formation when boiling 1-hexanol on the finned stainless-steel tube (R29).

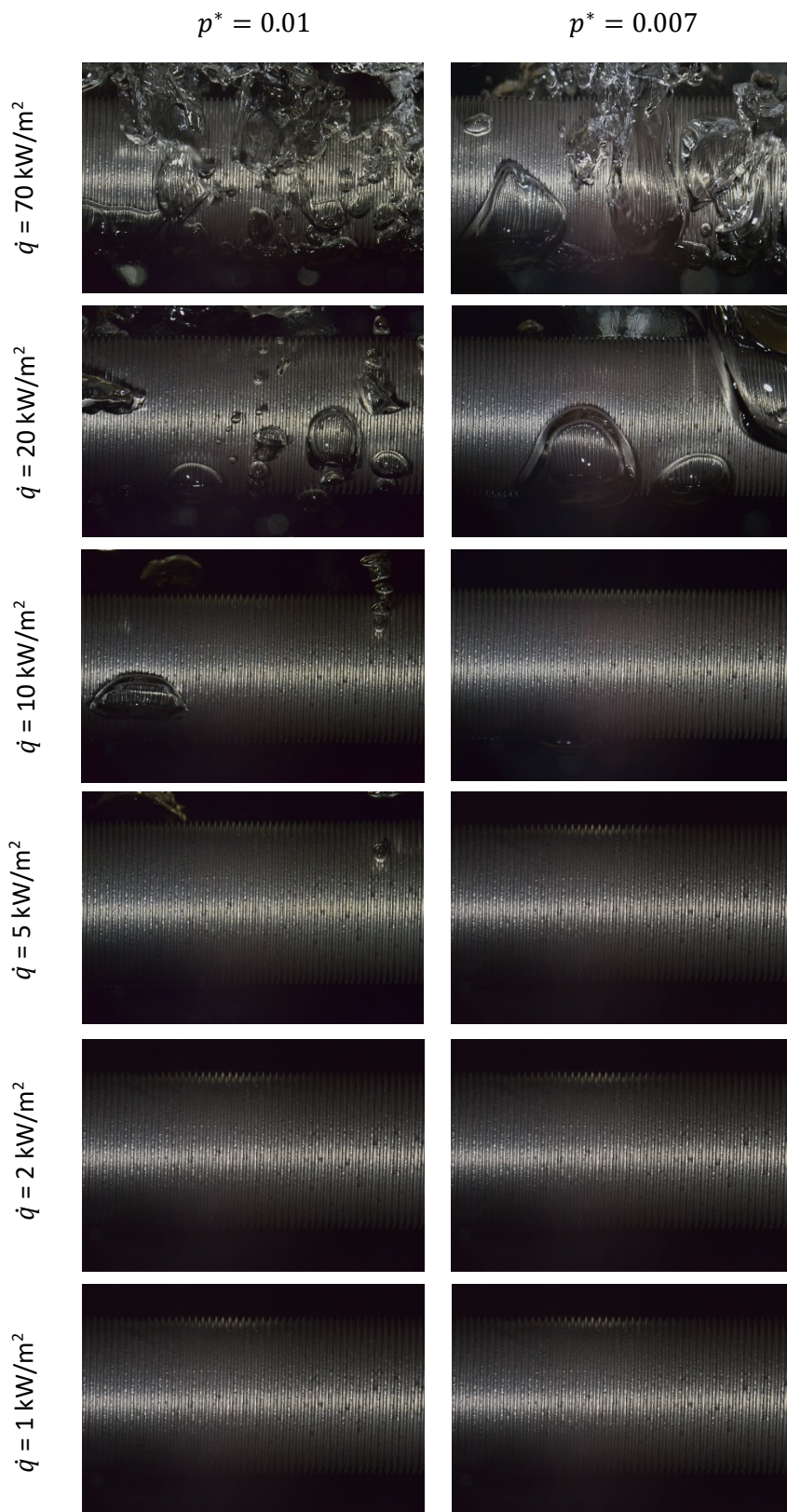
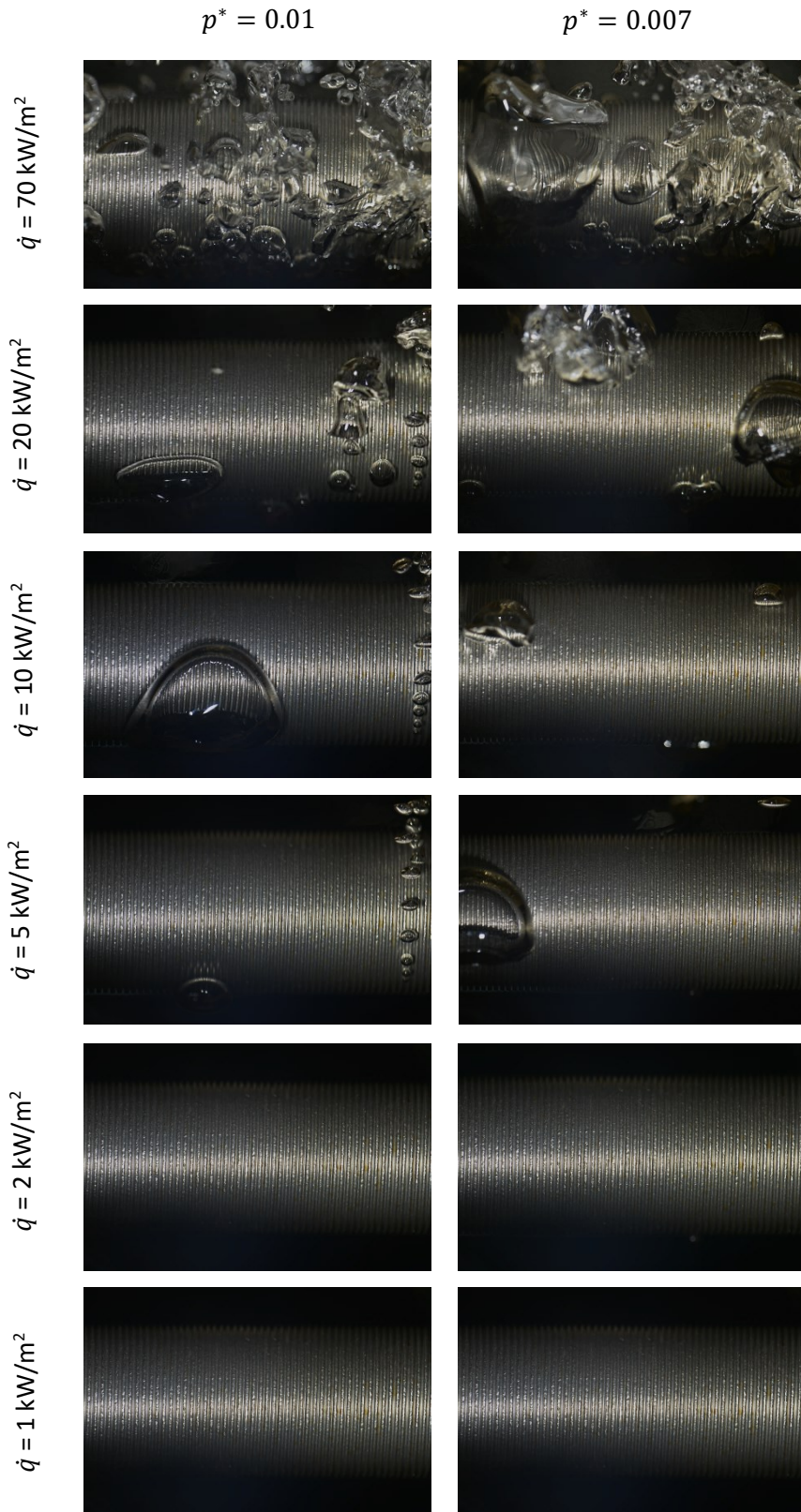


Table 8.20: Bubble formation when boiling 1-pentanol on the finned stainless-steel tube (R29).









## RINGRAZIAMENTI

Vorrei riservare questo spazio finale della mia tesi di laurea ai ringraziamenti verso tutti coloro che hanno contribuito, con il loro instancabile supporto, al mio percorso di crescita universitaria e professionale. Non posso non ringraziare la mia famiglia per avermi aiutata a superare i momenti più difficili. Ringrazio poi i miei amici, per aver alleggerito i momenti più pesanti e per avermi spronato a dare sempre di più. Infine, vorrei dedicare questa tesi a mia nonna, la quale con semplici gesti ha saputo darmi un grande supporto in questo mio cammino.

